On the theory and modelling of Fourth Generation Light Source

A thesis submitted to The Department of Physics
of the University of Strathclyde
for the degree of Doctor of Philosophy.

Cynthia Kar Woon Nam

January 5, 2009

© Copyright 2009

Signed: Date:

Abstract

This thesis reports research carried out to develop a non-averaged 3D simulation code written using minimal approximation to model a Free Electron Laser (FEL) amplifier, the so-called fourth generation light source. Previous generations of light source use synchrotron which has poor temporal coherence. The current race to build the next generation of coherent light sources, FELs, has started and the work carried out in this thesis aims to provide a new simulation code to give insight on the behaviour of the electrons and radiation interaction below the radiation wavelength limit.

The numerical simulation was written in Fortran 90 for use on parallel architecture computers to model a Free Electron Laser in three spatial dimensions and including time dependent effects. The Maxwell wave equation and Lorentz equation were used to describe the radiation field evolution and the electrons' propagation. These equations were scaled to become dimensionless. A finite element method, linear solver and Runge–Kutta method were applied to solve these equations.

Previous results were reproduced in the 1D limit. Coherent Spontaneous Emission (CSE) was reproduced; this can not be done by other current 3D simulators. Other numerical studies include the FEL interaction, electron shot-noise and modelling of the energy spread and emittance of the electron beam.

A final simulation demonstrates radiation diffractive effects in a full nonlinear FEL interaction including all 3D effects. This code is the first of its type to be developed and will allow a completely new range of physics of the FEL to be investigated and exploited.

Contents

List of Figures

List of Tables

Acknowledgements

Firstly, I gratefully acknowledge EPSRC, Daresbury Laboratory and my supervisor, Dr Brian McNeil, for providing funding for my PhD. Brian has helped and advised me to achieve not just the work on my thesis, also in many other ways. I would like to take this opportunity to say thank you to him; he is the most respected teacher to me. Prof. Alan Phelps was my undergraduate advisor and postgraduate advisor. He is one of the people who gave me good advice and someone I greatly respect.

The people I have worked with in the Department of Physics at the University of Strathclyde are: Dr Gordon Robb, Dr Pamela Johnston and Lawrence Campbell. They have helped me in their own different ways and I am very grateful. Gordon, who shared an office with me for three years, deserves a special mention for putting up with me being cold all the time, even in the summer, so the extra heater in the room was switched on most of the time. Michal Hemmerling, the next victim, shared the office with me for the next one and a half years and also became one of my good friends. I would like to apologise for the fact that I have to keep the blinds and the window closed all the time when I know that he likes the sunshine and fresh air. Dr Ricky Martin has helped me a lot in using NAG libraries and with other computer problems. He also offered me the chance to teach an undergraduate computational physics class and earn some extra pocket money. Thank you so much Ricky.

I would like to thank Dr Allan Whiteford, Dr Paul Bryans and Dr Martin Torney for their computational knowledge, being my computer technicians and coming up with interesting topics over tea/coffee break. I promise I will not reset the index inside a loop in the future, Martin. Thank you Allan for the new graphics card in the last nine months of my PhD. On several occasions I managed to overwrite the boot sector of my hard disk and Allan came to the rescue. Even though Paul left Glasgow and went to New York, I would like to thank him for making me laugh during tea break.

During my PhD I had the opportunity to work at Daresbury Laboratory, Cheshire, in the ASTeC group. The people in this group were very helpful, made me feel like part of the team, and were very generous with their time, milk and tea. In my last visit (Nov 2008) to the Daresbury lab, the ASTeC group had moved to a new building with air-con. I was happy to see everyone and congratulations to Neil Thompson and Dr Hywel Owen who recently had new arrivals to their families.

I would like to thank Dr Aidan Arnold for being the middle man and organising my viva. Also I am grateful that Dr Paul McKenna, my internal examiner, and Prof Alan Gillespie, my external examiner, spent time reading my thesis and all the horrible equations in detail. Thank you for all your advice and comments on my thesis. Their interest in my thesis led to a thorough exam that was not as bad as I imagined. I was happy when they told me that the structure of my thesis and the work were good and ever happier when they told me I had passed.

The next thank you goes to my Mum (Rosa), Dad (Francis) and brother

(Leon). Thank you for cooking everyday, listening to me moaning every minute and giving me advice on everything. Thank you so much, especially to my parents who gave up their life in Hong Kong and moved to the UK so my brother and I could have a better education. They have encouraged me from a young age and I think I have made them proud. Thank you again for all your support.

Finally, thank you to my fiancé, Dr Iain Paton, for all his support. The wedding plan was postponed year after year since 2005 and he had to tell others to shut up when they asked when the wedding was taking place. He has been a great teacher, since he allegedly knows everything, and is the only one apart from my parents who has and will put up with my temper. I am lost for words on how much I appreciate his help and love for me. Thank you once again Iain.

Cynthia Kar Woon Nam
— December 2008

Chapter 1

Introduction

The main source of the fourth generation light source is the coherent radiation emitted from a Free Electron Laser (FEL). The history of synchrotron radiation is introduced first in this chapter and the history of the past generation light sources are discussed. The development of each generation light source and how the laboratories made necessary changes to their facilities in order to upgrade to the next step are discussed next. Introduction to and the fundamental theory of FEL are briefly discussed. Towards the end of this chapter, the fourth generation light sources that were proposed or are being built, and the applications of those sources, are explained.

1.1 Synchrotron radiation

Synchrotron radiation is the main light source generated in the development of first to fourth generation light sources. This radiation is naturally occurring; an example of this is charged particles of matter spiralling through the cosmos and the radiation emitted can be detected by instruments on earth. In the past more than 50 years, there has been a growing interest in research which is reliant on synchrotron radiation. This form of electromagnetic radiation is emitted by charged particles when they are accelerated at relativistic speeds in a magnetic field. The spectral range of synchrotron radiation covers from infra-red to hard x-ray; therefore a wide range of energies can be produced with brightness many orders of magnitude greater than the radiation produced from conventional x-ray tubes. In addition, high collimation is achieved and the radiation is emitted in a narrow cone in the forward direction.

1.1.1 History of light source and the first generation light source

The first theoretical appearance of synchrotron radiation was during research on radial acceleration of charged particles in 1944 published by Ivanenko and Pomeranchuk (Soviet Union). Their calculation showed energy losses due to radiating electrons and this radiation was a by-product of their research [1]. In 1947, synchrotron radiation was first observed by Herb Pollock, Robert Langmuir, Frank Elder, and Anatole Gurewitsch at the General Electric Research Laboratory in Schenectady, New York [1, 2]. The bluish-white light was detected emerging from the transparent toroidal electron tube of their new 70MeV electron synchrotron accelerator. Initially, this was considered a nuisance to particle physics experiments because it constituted a major source of energy-loss in the particle accelerator; it was regarded as an unwanted by-product. Due to this phenomenon the performance in radial particle acceleration of the time was restricted. An experiment was performed by Tomboulian and Hartman in 1956 using a 320MeV electron synchrotron at Cornell and synchrotron radiation was exploited for scientific experiment for the first time [3]. Synchrotron Ultraviolet Radiation Facility (SURF) was the first generation light source built specifically to produce photons at the National Bureau of Standards (now National Institute of Standards and Technology) in 1961 and was used in 'parasitic mode' because the accelerators were built, and usually operated mainly for high-energy or nuclear physics. A few years after the world's first synchrotron light source arrived, Asia and Europe followed the same activity. The Institute for Nuclear Studies–Synchrotron Orbital Radiation (INS-SOR) group was formed in Tokyo in 1962 and measurement of soft x-ray absorption spectra of solids using light from a 750MeV source was made in 1965 [3]. In 1964, the 6GeV Deutsches Elektronen-Synchrotron (DESY) was used in Hamburg and they began operating both high-energy physics and synchrotron radiation experimental campaigns. Initially most of the first generation light sources were parasitic facilities and were soon replaced by the next development of electron storage rings in 1965, the basis of all modern synchrotron sources.

Previously, a proposal for a high-current accelerator for particle physics was developed in the 1950s when MURA (Midwest Universities Research Association) was formed. They had designed a 240MeV storage ring as a test bed for advanced accelerator concepts and it was built in Illinois; this facility became the Fermi National Accelerator Laboratory. Interest grew in synchrotron radiation in the 1960s and MURA agreed to provide access to synchrotron radiation without

affecting the accelerator studies by applied changes in the storage ring vacuum chamber. A storage ring called Tantalus I was operating for synchrotron-radiation research at the University of Wisconsin and the first spectrum was measured in 1968.

At the Orsay laboratory in France, synchrotron radiation work began in 1971 using the 540MeV ACO (Anneaux Collisions Orsay) storage ring. In 1974 SUR-FII, a 250MeV storage ring, opened to the market of synchrotron radiation research and the INS-SOR group from Tokyo started constructing a 300MeV storage ring. This device was built from the start specifically for the production of synchrotron radiation. The first multi-user storage ring facility was the 2.5GeV SPEAR (Stanford Positron Electron Asymmetric Ring) ring at the Stanford Linear Accelerator Center(SLAC), completed in 1972. Additional storage rings included Double Ring Storage (DORIS) at the DESY laboratory. This was set up as an electron-positron collider for high energy physics. There are many more worldwide, for example the Cornell Electron Storage Ring (CESR) at Cornell University, Ithaca, New York State.

1.1.2 Second Generation Light Source

Research moved from the parasitic light source of the first generation with limited output of synchrotron radiation to the second generation light source facilities. These were designed specifically to produce synchrotron radiation, and it allowed for a greater energy output without interfering with other experiments. This increase of energy made it possible to increase the number of work stations and beamlines at each facility. In 1980, the SRS (Synchrotron Radiation Source) located at the Daresbury Laboratory began to operate as a world-class machine dedicated to the exploitation of synchrotron radiation. The SRS closed this year(2008). The SRS was a 2GeV electron storage ring and the electrons were accelerated to ultra-relativistic energies in a circular path. The light beam emitted could be finely focussed and operated at high circulating currents(150-250mA) [4]. The emitted radiation from the SRS had a broad range of wavelengths from infrared through visible, ultraviolet and down to the x-ray region. The SRS consisted of two x-ray wigglers, a VUV-SXR (Vacuum Ultra Violet-Soft X-Ray) undulator and three multipole wigglers. Each experimental station was optimised to a particular spectral range segment. This facility began experiments in 1981 and around the ring it had approximately 12 beamlines with 40 stations. The Photon Factory (PF) in Tsukuba Science City (Japan) is another facility which is classed as a second GLS. The first and original ring of 2.5GeV

began to operate in 1982 and it was the first to provide synchrotron x-rays for research. A second 6.5GeV ring was used as a synchrotron source in parasitic mode in 1986 and then it was converted as a single-bunch electron storage ring in 1997. Both rings have had upgrades in order to improve their output by reducing the emittance (a measure of the quality of the electron beam, lower emittance is higher quality) of the 2.5GeV ring from 400nm.rad to 36nm.rad and increasing the number of straight section of insertion devices from 7 to 13 by replacing and rearranging quadrupole magnets. For the 6.5GeV ring, the life time of the electron beam was increased by replacing the vacuum system components completely. Around the same period, the construction of the National Synchrotron Light Source(NSLS), in Brookhaven National Laboratory(BNL), was completed, which included 700MeV and 2.5GeV storage rings. In addition, a new 1GeV storage ring called Aladdin was built at the University of Wisconsin Synchrotron Radiation Center and the Berliner Elektronenspeicherring-Gesellschaft für Synchrotronstrahlung (BESSY) in Berlin began to serve users in 1982 with a 800MeV storage ring. The Stanford Synchrotron Radiation Laboratory at SLAC and HASYLAB (Hamburger Synchrotronstrahlungslabor) at DESY were the ones who upgraded their first generation light source facilities to the second generation. All the above second generation light source facilities are only representative of many which are dedicated to the research and use of synchrotron radiation. The number of synchrotron radiation facilities continues to grow.

1.1.3 Third Generation Light Source

The next development of research facilities for synchrotron radiation, the third generation light source, brought high brilliance with lower emittance and long straight sections of insertion devices. These insertion devices are undulators and wigglers which can be placed along an empty straight section that connects the curved arcs of large storage rings. A planar undulator, which is commonly used, is a magnetic structure with an array of closely-spaced dipole magnets of alternating polarity. When the electron beam propagates longitudinally along the undulator its trajectory oscillates in the horizontal plane. Wigglers generally have a higher field and fewer dipoles than undulators. They produce a continuous spectrum with a higher flux and can be extended to shorter wavelengths than a single bending magnet. Only a small section of the angular range of the radiation cone from a bending magnet can be used for experiment since the angle of the radiation cone is fairly large. Therefore most of the radiation from the bending magnets was not used in the storage ring; for this reason the output power would

(a) ESRF, image courtesy of `www.esrf.eu`.

(b) APS, image courtesy of `www.aps.anl.gov`.

Figure 1.1: European Synchrotron Radiation Facility located in France, 1.1(a), and Advanced Photo Source located in USA, 1.1(b)

be limited.

Since these insertion devices wiggle/undulate the electron beam back and forth through multiple bending magnet fields, these magnets generate a higher-brightness photon beam than bending magnets alone. Undulator magnets have the additional feature that they generate narrow spectral lines and this enhances the overall photon brilliance of the machine. Today, there are 43 operational second and third-generation synchrotron light sources with more than 15 third-generation facilities presently under construction[5].

With the advancement of the third generation light source, users were able to access the information which was not possible previously; x-ray microscopy and spectromicroscopy require to resolve information spatially, dynamical information can be extracted and users such as spectroscopists and crystallographers were able to extract information on the sub-picosecond time scale.

Chasman and Green designed the double-bend achromat, and it is known as the Chasman-Green lattice today [3]. This periodic arrangement of magnets can bend, focus and correct the electron beam and therefore it has low emittance and yields a high brightness light source. This form of lattice is the basis for most of today's synchrotron sources and it enables NSLS to deliver world-class beams of light.

The first of the third generation machines was the European Synchrotron Radiation Facility (ESRF) in Grenoble, see figure 1.1(a). Construction was begun in 1988 by twelve European countries and six additional countries later on. ESRF specialise in hard x-rays produced with high brilliance. The electrons were successfully injected for the first time in the 6GeV storage ring at the beginning

of 1992 and by the end of the year all the target values such as beam lifetime, brilliance, stability of the storage ring were achieved or exceeded[6]. In 1994 the storage ring with fifteen operational beamlines opened its door to users and forty beamlines were available to researchers from all over the world from 1998. In the autumn of 1995, the Advanced Photon Source (APS) at Argonne National Laboratory began to operate with a 7GeV electron storage ring. The SPring8 is another third-generation source which began operation in late 1997 (Harima Science Garden City Hyogo, Japan) with an operational energy of 8GeV and 62 beamlines. These are the three largest third-generation synchrotron radiation facilities in the world in the short wavelength range.

The largest third generation light source in the UK is the Diamond Light Source. Currently, Diamond is the best medium-energy x-ray source and it can produce x-rays with photon energies ranging between 100eV to 20keV. This vast machine began to operate at the beginning of 2007 and there are seven beamlines in operation. An additional fifteen beamlines will be installed in the future. The structure of this machine is a vast toroidal building as can be seen in figure 1.2, the diameter of the booster is approximately 51 meters and of the storage ring is 179 meters. The electrons are accelerated by the LINAC and the booster synchrotron to ultra-relativistic speeds and then injected into the storage ring. The electron acceleration is constant in the storage ring, the direction of travel is different all the time, and synchrotron radiation is emitted by the electrons as they lose their energy. As described previously, Diamond produces light in the x-ray, the ultra-violet and infrared range with exceptional brightness. This intense light is diverted to each research station around the storage ring where scientists and engineers carry out experiments to gain a deeper understanding of their field of study, such as biotechnology, medicine, environmental studies and material science. Studies such as understanding the structure of complex biological samples, including proteins, use three of the beamlines. Other experiments using one beamline include the study of material under extreme conditions such as intense temperature and pressure and examine the electronic and magnetic properties of materials at the atomic level.

1.2 Free Electron Laser (FEL)

Three generations of light source facilities around the world were outlined in the previous sections. The fourth generation light source uses the FEL technology instead of bending magnets or insertion devices in a storage ring. The origin

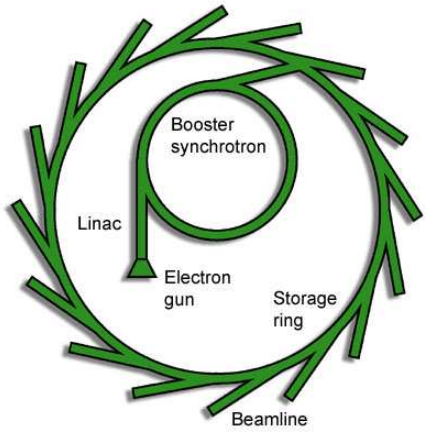

(a)

(b)

Figure 1.2: Schematic diagram of the main section of Diamond, 1.2(a) and aerial view of Diamond, 1.2(b). Image courtesy of `www.diamond.ac.uk`.

and history of the FEL are discussed in the next section followed by the current development and application of the fourth generation light source in subsequent sections.

A high vacuum electron tube that operates in the microwave frequency range is known as a microwave tube [7]. The concept of the FEL developed from the microwave tube invented in the mid twentieth century. The wavelengths produced from the microwave tube ranges from several meters to approximately one millimeter. The limitation of the size of the cavities inside the tubes resulted in wavelengths of less than 1mm being diffcult to produce.

In 1958, the invention of an open resonator became the most important step in developing the conventional laser as known today [8]. The essence of the laser is an optical resonator in the cavity of which it is possible to store vast amounts of optical power at short wavelengths. As a result of the invention of the laser, a wavelength of about four orders of magnitude smaller than the microwave tube would then be reached [8].

John Madey invented the Free Electron Laser(FEL) in 1971. This FEL was a combination of the methods used in microwave tubes and conventional laser cavities. Madey and his co-workers constructed a low-gain FEL amplifier in 1976 and measured the gain. The FEL oscillator was built in 1977 and began a great interest in this research field. The free electron laser is a powerful device for producing intense coherent radiation and it is based on the electromagnetic interaction of relativistic electrons with a static wiggler field and may be described classically. The interaction does not occur via quantum transitions of bound electrons, but it

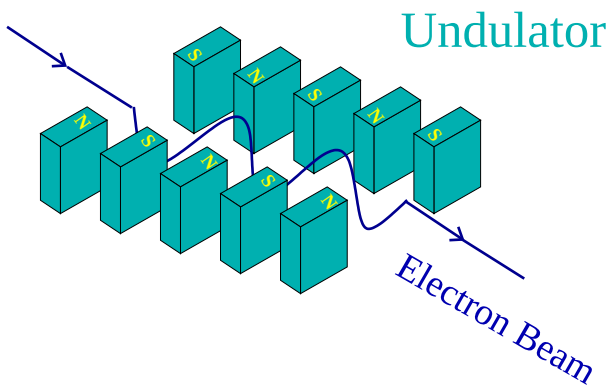

Figure 1.3: A sketch of a planar undulator and electron beam trajectory.

occurs from a beam of free electrons, like the microwave tubes, travelling through a magnetic field. The greatest advantages of the FEL are undoubtedly its tunability and very high peak power; unfortunately these advantages come at a price, with the main disadvantages being the size and cost of the FEL.

1.2.1 Outline of FEL

A Free Electron Laser consists of two major components; a linear accelerator and an insertion device such as an undulator. The electrons are accelerated in the linear accelerator and then enter into the undulator. The undulator consists of arrays of magnets with alternating poles. A schematic of the magnetic structure of a planar undulator can be seen in figure 1.3.

In the planar undulator the electrons are forced to oscillate in a plane, figure 1.3, which is perpendicular to both the undulator field

$$\boldsymbol{B_w} = \widehat{\boldsymbol{x}} B_w \sin\{k_w z\} \tag{1.1}$$

and its propagation direction z. The light emitted from this system is linearly polarized. A helical undulator is another type of undulator, with a field given by the helical wiggler is used in all the simulations discussed in this thesis. The electron trajectory in a helical undulator, figure 1.4, is a spiralling motion in the transverse plane and generates circularly polarised radiation.

$$\boldsymbol{B_w} = B_w(\widehat{\boldsymbol{x}} \sin\{k_w z\} + \widehat{\boldsymbol{y}} \cos\{k_w z\}) \tag{1.2}$$

When the relativistic electrons enter the helical undulator with magnetic field B_w and propagate in the forward direction their trajectory path is shown in

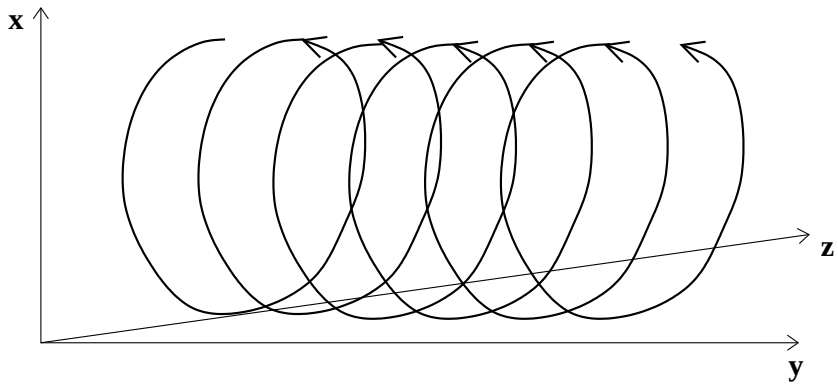

Figure 1.4: A sketch of the electron propagation path in a helical undulator.

figure 1.4. The electrons' paths are constantly changing direction therefore they are always accelerated and synchrotron radiation is emitted as a result. This radiation is intense and confined around the instantaneous velocity vector [9].

Due to the transverse electron motion an energy-exchange may occur between the electromagnetic field and the beam electrons. This is maximised when the FEL resonance condition is satisfied:

$$\lambda_r = \frac{\lambda_w}{2\gamma_0^2}(1 + a_w^2) \tag{1.3}$$

The wavelength λ_r of the radiation is determined by

1. The energy of the electron beam E_0,

$$E_0 = \gamma_0 m_e c^2 \tag{1.4}$$

   where the mass of an electron,m_e, the speed of light, c and the relativistic factor

$$\gamma_0 = (1 - \beta_\perp^2 - \beta_z^2)^{-1/2} \tag{1.5}$$

   with

$$\beta \equiv \frac{v}{c} \tag{1.6}$$

2. The wavelength of the undulator λ_w.

3. The magnetic field of the undulator, B_w; this is related to the wiggler parameter a_w in the following relation

$$a_w = \frac{eB_w}{m_e c k_w} \tag{1.7}$$

   where e is the charge of an electron and k_w is the undulator wave number,

defined as

$$k_w = \frac{2\pi}{\lambda_w} \tag{1.8}$$

By adjusting any of the three parameters above, the radiation wavelength can be varied over a wide range; this is in contrast to a conventional laser. Coherent synchrotron radiation is emitted by the electrons as a result of the energy exchange between the electrons with the combined wiggler and radiation fields. The process of the energy exchange will be discussed in more detail later in the next chapter.

1.3 Developments and Applications of the Fourth Generation Light Source

The next, Fourth, generation light source uses FEL rather than storage rings to produce coherent synchrotron radiation. The radiation produced in the 4th generation sources is greater by orders of magnitude in peak power and the electron beam emittance will be much lower to achieve higher order brightness than the previous generation sources.

1.3.1 Worldwide Fourth Generation Light Sources

Talk of developing the fourth generation light source began in the early 1990s and many countries had ideas to expand or modify their existing facilities to get ready for the next light source. In America, the Linac Coherent Light Source (LCLS) at SLAC will use SLAC's two mile long linac to accelerate the electrons to energies of 16GeV. This facility will be in operation in 2009 and it will be the world's first hard x-ray free electron laser with wavelengths approaching 1Å. The LCLS uses a planar hybrid undulator with permanent magnet quadrupoles to focus the electron beam. X-ray pulses produced from the LCLS will be approximately eight orders of magnitude brighter than the most powerful sources currently available. Their uses will be discussed in the last section of this chapter.

The European XFEL laboratory is another large facility which will produce x-rays and is located at the DESY site in Hamburg. An interesting fact is that most of this facility will be built underneath a residential area. The full length of XFEL is 3.4km [10] and it will be the world's longest artificial light source. A new superconducting linac will be used to accelerate the electrons to 10-20GeV before entering the undulator.

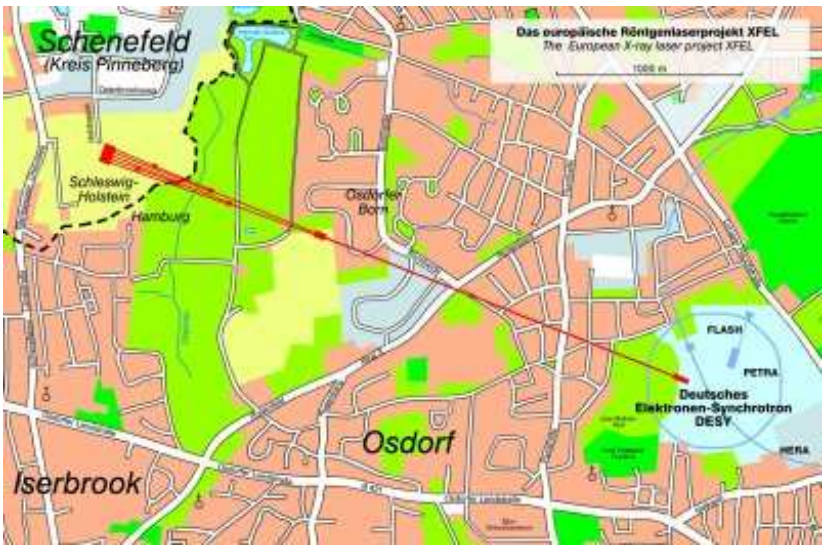

Figure 1.5: Location and schematic (red) of the XFEL facility. `Image courtesy of www.xfel.desy.de`.

There will be three sites on the above-ground level and they are located at DESY-Bahrenfeld site, the Osdorfer Born site and a research site in Schenefeld, see figure 1.5. The electrons are injected at the DESY Bahrenfeld site and accelerated. The main linac will end at the Osdorfer Born site and the electron bunches will be separated then diverted to various tunnels. The light emitted by the electrons will reach the research site in Schenefeld with experimental stations where people can operate their experiments with the intense x-ray light.

Japan has also dedicated resources to intense x-ray sources, which will culminate in a prototype of an x-ray FEL called the SPring-8 Compact SASE Source (SCSS), see figure 1.6 [11]. This is being built and is scheduled to start operations towards the end of 2010. Their aim is to produce a high peak-brilliance soft x-ray FEL on the order of 1Å. The facility in Japan was being built from scratch and it was reported to lase at wavelengths between 51-61nm [12]. Although XFEL is the world leader, lasing and carrying out experiments at the shortest wavelength at 6.5nm, the size of SCSS x-ray FEL facility fits into an 800m long site, whereas the XFEL site is 3.4km long. They have reduced the size of each component and the advantage of cost benefits the Japanese design.

The conventional way of generating electrons used a laser and photoelectric emission, but the electron gun used in the SCSS prototype uses a single crystal of CeB_6 as a hot cathode. The quality of the beam can be maintained during acceleration and their target is to achieve saturated lasing with x-rays at a wavelength of 2Å.

A proposed UK Fourth Generation Light Source Project (4GLS) was going to

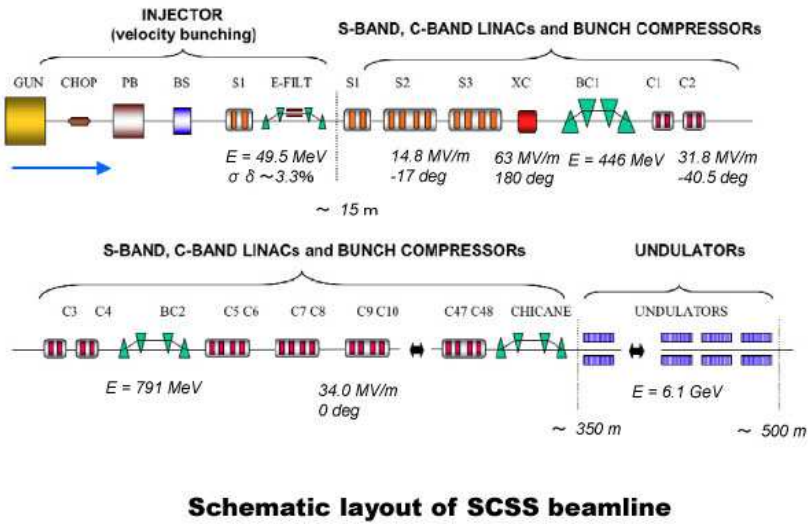

Figure 1.6: Schematic diagram of SCSS: Electron Gun, 1-GeVLinac, 8-GeV Booster synchrotron and 8-GeV Storage Ring. Image courtesy of `www-xfel.spring8.or.jp`.

be built on the existing site of STFC Daresbury laboratory in Cheshire. It was to be the world's first proposal as a multi-source and multi-user facility which uses both energy recovery linac (ERL) and FEL technology. The layout of 4GLS is shown in figure 1.7. The FEL radiation emitted from this system could cover from hundreds of microns to the soft x-ray (SXR) region. Using three FELs, XUV-FEL (extreme ultra violet), VUV-FEL (vacuum ultra-violet) and IR-FEL (infra-red). This multi-source facility could provide users with a wide range of wavelengths in a pump-probe configuration. Two of the FELs, VUV-FEL and IR-FEL, were an oscillator type using mirrors. The XUV-FEL operates in a single-pass high gain mode without any mirrors since the electrons propagate through a long undulator once and a short pulse will be emitted. The short electron bunches produced in this system would emit femtosecond pulses of radiation at high repetition rate.

The main linac located at the top of the figure 1.7, is a 600MeV superconducting linac to accelerate and produce high quality electron beams. The design of the facility is particularly efficient after the electrons are accelerated in the linac. The electrons will be split up into two routes in the beam separator. Some of them will continue to the middle section where they will be further accelerated to the desired energy and propagate into the XUV-FEL. An additional initial seed field can be injected along with the electrons. Quadrupoles are placed to focus the electron beam before entering into the XUV-FEL and periodically throughout. After the electrons emit radiation in the XUV-FEL, they will be discarded in the electron beam dump. On the other route, the electrons propagate through

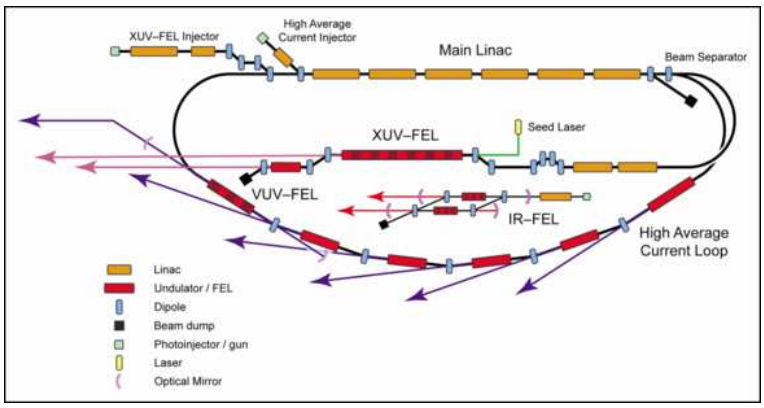

Figure 1.7: The proposed layout of the cancelled UK 4GLS facility. `Image courtesy of www.4gls.ac.uk`.

more undulators and a dipole is placed after each undulator. This is to divert any radiation emitted from the electrons to the user station and also to progressively bunch the electrons to higher currents. The VUV-FEL is the final section for the electrons to travel through and the electrons return to the beginning of the main linac. The electrons will be recycled for the next run by decelerating them to give energy to the RF field of the linac. This energy is used to accelerate the new set of incoming electrons. The old electrons will end their journey at the electron beam dump at the end of the main linac. The IR-FEL was to operate independently from the other FELs. While the 4GLS project has been cancelled the UK is now looking to develop the New Light Source [13].

1.3.2 Application of the next generation light source

Discussions on how each generation light source was developed and the quality of the electron beam as well as the synchrotron radiation emitted by the electrons has been improved from one generation to the next. The high power output and broad range of wavelength of the radiation pulses that could be achieved could lead to experiments thought impossible to undertake in the past. The coherence of FELs operating at x-ray enables experiments that can study finer spatial structure. Currently one of the most challenging areas of functional biological research is how proteins fold. The existing standard techniques of x-ray crystallography are not suitable to study several hundred thousand proteins. The fourth generation light source will be able to study the three dimensional structure of the protein, which is unique, and displays a highly organised structure. Proteins are some of the most important of all the molecules found in any living organism. During the process of protein folding serious problems arise, which can

lead to misfolds, leading to Alzheimer's, Parkinson's disease, and many cancers and cancer-related syndromes [14]. The duration of the protein folding can occur within milliseconds down to nanoseconds and an increase in temporal resolution would be required to study the details of all these dynamic processes. Good time resolution is therefore important, and the next generation light source can provide a flexible timing structure down to femtosecond scales over a wide range of wavelengths.

The importance of investigating matters in small scale has been mentioned in the latter application, and nanoscience development does not only have an impact on our everyday lives, it is also important in many scientific studies. The fastest growing area of science and technology is probably the development of nanoscience and nanotechnology. The high brightness, intense and coherent radiation from the new source could examine single or clusters of nanoscale objects and their interactions. Studies of transition effects could be carried out when doping a molecule in a cluster and observing its properties as a function of cluster size. When the molecule absorbs infrared photons from an IR-FEL it dissociates since the molecule is weakly bound to the cluster and the cluster fragments will subsequently be lost from the beam. By measuring the infrared absorption spectrum during the absorption processes, detailed information can be obtained.

These examples illustrate the more general application of this technology in different branches of science to investigate physical, biological and chemical processes as they occur and the very real potential this area of research has in the future.

The theory and the mathematics of an FEL are derived in the next chapter. The approximations used in current three dimensional models will be discussed and extended to the 3D model developed in this thesis.

Chapter 2

Theory and modelling of the 4GLS

The next, fourth, generation of synchrotron radiation consists mainly of the FEL. The lasing action takes place when the electrons travel freely along the undulator and interact with the combined wiggler and radiation field from the undulator. There are existing FEL simulations which can model this phenomena e.g. [15, 16, 17]. The new simulation of this thesis was written not only to model in one dimensional space, but to extend the study to three dimensional space with time-dependence. Fundamental theories are applied and the assumptions made in the new 3D model are less restricted than previous models leading to potentially new areas of FEL physics being simulated and investigated.

A brief summary of the methods used to solve the 3D Maxwell wave equation and Lorentz equation is discussed next. Current 3D simulation models and the approximations that were applied to their models is discussed. The rest of the chapter is divided into the following topics: the physics of the FEL; the steady state (time independent) 1D model, a linear stability analysis was carried out; a 1D (time dependent) FEL model that uses electron pulses to produced coherent radiation and superradiance effects are discussed; the derivation of the equations and analytical theory of a 3D model using minimal approximation is presented.

2.1 An overview of the calculation of new FEL code

The calculation of the wave equation, Lorentz force equation and particles' trajectory equations are all scaled with respect to the radiation rest frame $(z - ct)$.

The radiation is in its stationary frame while the electrons propagate backwards with respect to the radiation. This is the opposite case from one of the 1D simulation [18] where the electrons are stationary and radiation propagates in the forward direction.

The electric field envelope term (ξ_0) from the wave equation describes the diffraction effects explicitly along with the fast oscillating exponential term. There is no diffraction term written out implicitly, so there is no restriction on how the radiation evolves due to diffraction. In the Lorentz force equation the energy spread of the beam and the effects of betatron motion are included in this 3D system. The electrons' transverse position is scaled with respect to the gain length and co-operation length. There are six equations being solved simultaneously:

- A wave equation
- Two Lorentz force equations
- Three particle trajectory equations.

The main method used to solve the equations is called the Split-Step Fourier method. Within this SSFM, three subsequent methods are used collectively:

- Finite element Galerkin method
- Linear Solver
- 4th order Runge-Kutta method (rk4).

More details of these methods will be explained along with the derivation of all the equations in section 2.6. Before the main derivation of the equations, the current 3D models are examined and the approximations that applied are discussed.

2.2 Previous FEL simulations

The use of FELs has became more popular and there has been an increase in FEL simulation codes that can simulate the behaviour of the radiation field and the particles' motion. The main discussion here is about three-dimensional simulation codes such as GINGER, GENESIS, FAST and others [15, 16, 17].

GINGER is a multi-dimensional and time-dependent FEL simulation and has been developed over the past 18 years. Users can choose either a linear or a helical undulator for the FEL. A radial coordinate system, r, z and t are the spatial and

time independent parameters in the radiation field and a slowly-varying envelope approximation (SVEA) is applied to the radiation equations. The particles are described in terms of macroparticles with x, y, z and t being the independent variables of the particle equations. Originally, a Gear predictor-corrector scheme was used to solve the radiation field equation; a new direct implicit method has been used to replace the former method [15].

GENESIS is another three-dimensional and time-dependent simulation code. It supports both steady-state and time-dependent simulations. A memory saving method is used when running a time-dependent simulation [16]. The radiation field equation is discretised in a cartesian mesh and uses the Alternating Direction Implicit integration algorithm [19] to solve the field equation. There are six dimensions which describe the electron beam's motion and macroparticles are also used to represent the beam. The energy and phase equations which describe the longitudinal direction are integrated using rk4 while the electrons' equation in the transverse direction is calculated analytically.

FAST was developed to reduce the computational time required for a fast three dimensional, time-dependent simulation which takes slippage effects into account. The radiation fields are calculated with the presence of the resonance and paraxial approximations using an integral solution of Maxwell's equation, which can be found in [17]. The equations of the electrons' motions are described in the polar coordinate system, then the independent parameters are further reduced. This code provides an option to model a high-gain, high-efficiency FEL amplifier with a tapered undulator. The concept of tapered undulator was suggested by Kroll, Morton and Rosenbluth and other authors [9] and the FEL efficiency can be improved, by decreasing the wiggler field B_w to compensate for the decrease of averaged relativistic energy, $<\gamma>$, so keeping the FEL process in resonance. An external seed field as well as the initial shot-noise in the electron beam can also be simulated.

2.2.1 Approximations

In the last section, three current 3D simulation models were briefly discussed detailing the different methods used to solve the FEL system of equations. The approximations used in the models will be explained in this section. A different approximation, as applied to the 3D model derived in this thesis is also discussed.

The paraxial approximation as used in previous models assumes the radiation propagates very close to the main undulator axis (the z-axis) of the system, i.e. the angle, θ is small about the z axis, see figure 2.1. The variation of radiation

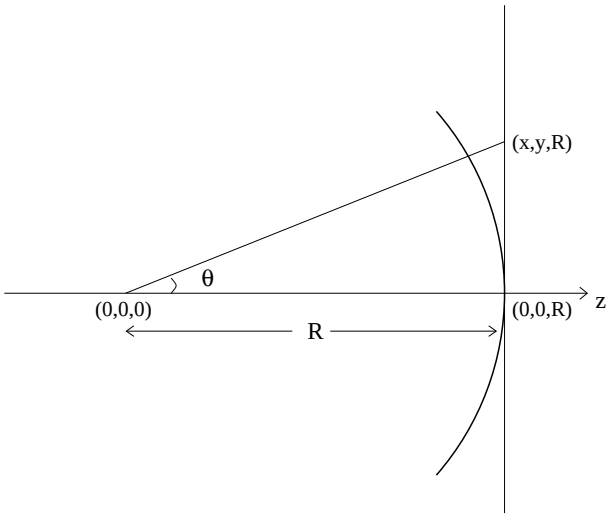

Figure 2.1: The propagation direction of the light is assumed to deviate only slightly from the z-axis; this is the paraxial approximation.

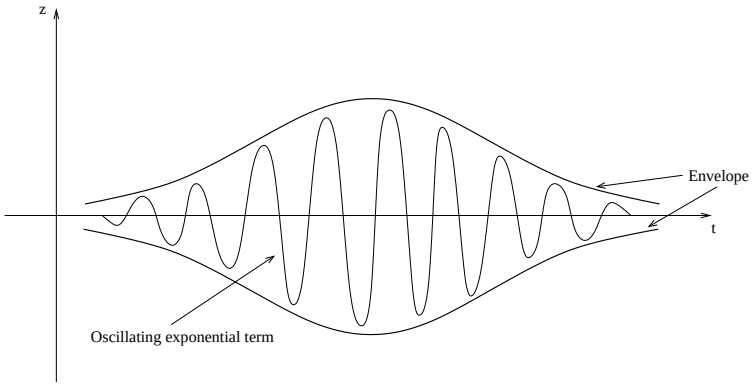

Figure 2.2: The radiation electric field consists of a slowly varying complex envelope and a complex exponential term describing the fast field oscillations.

in the transverse plane is assumed to be a spherical wavefront [20].

The second approximation is the Slowly Varying Envelope Approximation, SVEA [9]. This is a standard approximation made in many simulations to approximate the radiation field. The radiation field is composed of the product of the radiation envelope term and a fast varying exponential term, see figure 2.2,

$$\boldsymbol{E}(x, y, z, t) \equiv \xi_0(x, y, z, t) \times \exp i(kz - \omega t). \tag{2.1}$$

The SVEA reads as,

$$\begin{aligned} &\left|\frac{\partial^2 \xi_0}{\partial z^2}\right| \ll \left|k\frac{\partial \xi_0}{\partial z}\right|, \quad \left|\frac{\partial^2 \xi_0}{\partial t^2}\right| \ll \left|\omega\frac{\partial \xi_0}{\partial t}\right| \\ &\Rightarrow \left|\frac{\partial \xi_0}{\partial z}\right| \ll |k\xi_0|, \qquad \left|\frac{\partial \xi_0}{\partial t}\right| \ll |\omega\xi_0| \end{aligned} \tag{2.2}$$

where ξ_0 is the radiation field envelope, k and ω are the radiation wave number and frequency respectively. The radiation envelope varies slowly in time and space with respect to a period and wavelength of the radiation.

The two approximations explained above are generic approximations often applied to the wave equation; however, they were not applied in the 3D model presented in this thesis. The only approximation made is the variation of ξ_0 and $\dfrac{\partial \xi_0}{\partial z}$ are negligible in one undulator period in the z direction [20]. This approximation is named "complex envelope approximation" in this thesis so it can be referred to easily.

$$\left|\frac{\partial^2 \xi_0}{\partial z^2}\right| \ll \left|k\frac{\partial \xi_0}{\partial z}\right|, \quad \left|\frac{\partial \xi_0}{\partial z}\right| \ll |k\xi_0|. \tag{2.3}$$

This approximation does not define how the radiation varies in the transverse direction therefore the diffraction effects of the radiation will not be restricted. Also the radiation envelope need not vary slowing over a radiation period. In this next section the physics of FEL is discussed, including the concept of resonance condition, energy exchange and electron bunching.

2.3 FEL physics

The demand to develop a short wavelength (e.g., $\lambda_r \leq 1$nm) and high power FEL source has increased worldwide. This cannot be achieved using an optical cavity because there are no high reflectivity mirrors and coherent seed sources available to achieve the required performance at such short wavelengths. A process called self-amplified spontaneous emission (SASE) has been widely used in FEL development [9]. This process is achieved by injecting a high quality electron beam along a long undulator. As the electrons co-propagate along the undulator axis and interact with the spontaneous radiation the electrons tend to be bunched at the radiation wavelength. The intensity grows exponentially as the interaction between the electrons and the radiation continues until saturation occurs. The key to SASE is the initial shot-noise of the electron beam which radiates incoherent spontaneous radiation and will be described in section 2.3.3. Firstly, one must

understand how the electron propagates under the influence of the magnetic field of an undulator alone and then when the presence of the electric field is added. This leads to the next section describing the process of energy exchange between the radiation and the electrons and electron bunching.

2.3.1 Electron motion in an undulator

The trajectory of the electrons spiral in the transverse plane and travel in the longitudinal direction due to the magnetic field of the undulator, $\boldsymbol{B}_w$ defined as

$$\boldsymbol{B}_w = B_w(\sin k_w z\ \underline{\widehat{x}}, \cos k_w z\ \underline{\widehat{y}}, 0\ \underline{\widehat{z}}). \tag{2.4}$$

The electrons are periodically deflected by the Lorentz force and emit circularly polarized radiation in the forward direction, z. The motion of the electrons is described by the Lorentz force equation[1].

$$\boldsymbol{F} = -e(\boldsymbol{E} + \boldsymbol{v} \times \boldsymbol{B}) \tag{2.5}$$

The presence of an electric field is not included in a process of spontaneous emission as $|\boldsymbol{E}| \ll c|\boldsymbol{B}_w|$ therefore only the undulator magnetic field $\boldsymbol{B}_w$, is considered and the Lorentz force equation becomes

$$\boldsymbol{F} = -e(\boldsymbol{v} \times \boldsymbol{B}_w) \tag{2.6}$$

where e is the electron charge, $\boldsymbol{v}$ is the velocity of the electrons. λ_w is the undulator wavelength and $k_w = 2\pi/\lambda_w$. The force, $\boldsymbol{F}$, is also defined as the rate of change of momentum, $\boldsymbol{p}$, with respect to time, t and the momentum of a relativistic electron is,

$$\boldsymbol{p} = \gamma m \boldsymbol{v} \tag{2.7}$$

where m is the electron rest mass. Combine the definitions for the Lorentz force and momentum equation 2.7, equation 2.6 yields:

$$\frac{\mathrm{d}(\gamma m \boldsymbol{v})}{\mathrm{d}t} = -e(\boldsymbol{v} \times \boldsymbol{B}_w) \tag{2.8}$$

$$m\gamma \frac{\mathrm{d}\boldsymbol{v}}{\mathrm{d}t} + m\boldsymbol{v}\frac{\mathrm{d}\gamma}{\mathrm{d}t} = -e(\boldsymbol{v} \times \boldsymbol{B}_w). \tag{2.9}$$

[1]The Coulomb repulsion between the electrons has been neglected since the electron beam currents are small enough. This is called the Compton limit.

The second term on the l.h.s. in equation 2.9 is zero in the absence of any electric field. Hence:

$$m\gamma\frac{\mathrm{d}\boldsymbol{v}}{\mathrm{d}t} = -e(\boldsymbol{v}\times\boldsymbol{B}_w). \tag{2.10}$$

A proof of the relation between $\dot{\gamma}$ and $\boldsymbol{E}$ are shown in the next section and the derivation from equation 2.20 to equation 2.31. The solution for the electrons' velocity is derived by integration of equation 2.10 after the substitution of the definition of β, equation 1.6, and the undulator magnetic field

$$\begin{aligned}\beta_x &= -\frac{a_w}{\gamma}\cos k_w z\\ \beta_y &= -\frac{a_w}{\gamma}\sin k_w z\\ \beta_z &= \beta_{z0}\end{aligned} \tag{2.11}$$

where β_{z0} is a constant. The solution is shown in equation 2.11 and it can seen that the electrons have periodic oscillations in the x and y directions. In the z direction, β_z has a constant motion as can be shown using equations (1.5), (1.6) and (2.11).

$$\gamma = \frac{1}{\sqrt{1-(\beta_x^2+\beta_y^2+\beta_z^2)}} \tag{2.12}$$

$$\frac{1}{\gamma^2} = 1-(\beta_x^2+\beta_y^2+\beta_z^2) \tag{2.13}$$

$$\beta_z^2 = 1-\beta_x^2-\beta_y^2-\frac{1}{\gamma^2} \tag{2.14}$$

$$\beta_z = \sqrt{1-\beta_x^2-\beta_y^2-\frac{1}{\gamma^2}} \tag{2.15}$$

$$= \sqrt{1-\left(\frac{a_w}{\gamma}\right)^2(\cos^2 k_w z+\sin^2 k_w z)-\frac{1}{\gamma^2}} \tag{2.16}$$

$$= \sqrt{1-\left(\frac{a_w}{\gamma}\right)^2-\frac{1}{\gamma^2}} \tag{2.17}$$

$$= \sqrt{1-\frac{1}{\gamma^2}(a_w^2+1)} \tag{2.18}$$

For a given value of γ and a_w, the above calculations have shown that a constant value of β_z may be obtained.

Expressions of an electron's trajectories in all three spatial direction propagating in an undulator without any electric field was derived. Now consider the case where the electrons are propagating in the presence of both the magnetic field and electric field; the calculations are shown in the next section and the

resonance condition is derived.

2.3.2 Stimulated Emission

A useful expression must be derived via the Lorentz force equation with the presence of the electric field only. A similar method has been carried out and this time the magnetic field is neglected and the electric field acts alone, $\boldsymbol{E}$,

$$\boldsymbol{F} = -e\ \boldsymbol{E} \tag{2.19}$$

$$\frac{\mathrm{d}(\gamma m \boldsymbol{v})}{\mathrm{d}t} = -e\ \boldsymbol{E}. \tag{2.20}$$

To derive an expression of the time derivative of γ, one can, firstly, multiply equation 2.20 on both sides by $\boldsymbol{v}$, which yields

$$m\frac{d}{dt}(\gamma \boldsymbol{v}) \cdot \boldsymbol{v} = -e\boldsymbol{v} \cdot \boldsymbol{E} \tag{2.21}$$

$$m(\gamma \dot{\boldsymbol{v}} \cdot \boldsymbol{v} + \dot{\gamma}\boldsymbol{v}^2) = -e\boldsymbol{v} \cdot \boldsymbol{E} \tag{2.22}$$

$$m\left(\frac{\gamma}{2}\frac{d\boldsymbol{v}^2}{dt} + \dot{\gamma}\boldsymbol{v}^2\right) = -e\boldsymbol{v} \cdot \boldsymbol{E}. \tag{2.23}$$

By taking equation 1.5 and differentiating it with respect to t, the bracketed term in equation 2.23 can be written in a simpler form, as shown in the following;

$$\dot{\gamma} = \frac{d}{dt}\left(\frac{1}{\sqrt{1-\frac{\boldsymbol{v}^2}{c^2}}}\right) \tag{2.24}$$

$$= \frac{d}{dt}\left(\sqrt{1+\frac{\gamma^2\boldsymbol{v}^2}{c^2}}\right) \tag{2.25}$$

$$= \frac{1}{2c^2}\left(1+\frac{\gamma^2\boldsymbol{v}^2}{c^2}\right)^{-1/2}\ \frac{d(\gamma^2\boldsymbol{v}^2)}{dt} \tag{2.26}$$

$$= \frac{1}{2c^2}\frac{1}{\gamma}(2\boldsymbol{v}^2\gamma\dot{\gamma} + \gamma^2\frac{d\boldsymbol{v}^2}{dt}) \tag{2.27}$$

$$= \frac{1}{c^2}(\boldsymbol{v}^2\dot{\gamma} + \frac{\gamma}{2}\frac{d\boldsymbol{v}^2}{dt}) \tag{2.28}$$

$$\Rightarrow \boldsymbol{v}^2\dot{\gamma} + \frac{\gamma}{2}\frac{d\boldsymbol{v}^2}{dt} = \dot{\gamma}c^2 \tag{2.29}$$

One can now substitute derived equation 2.29 into equation 2.23 to give

$$m\dot{\gamma}c^2 = -e\boldsymbol{v}\cdot\boldsymbol{E} \tag{2.30}$$

$$\dot{\gamma} = -\frac{e}{mc}\boldsymbol{\beta}\cdot\boldsymbol{E}. \tag{2.31}$$

Equation 2.31 is an important expression which explains the process of energy exchange between the electrons and the radiation field. This is also related to the micro-bunching and it will be discussed further in section 2.3.3.

Now considering there is a radiation field co-propagating with the electron beam from the start and they travel through a constant undulator field, this initial radiation field can be produced by an external laser beam. The form of an expression for a radiation field has be mentioned in section 2.2.1 and the following equation 2.32 is a 1-D radiation field,

$$\boldsymbol{E}(z,t) = \frac{1}{\sqrt{2}}\left(\hat{\boldsymbol{e}}\xi_0(z,t)\exp i(kz-\omega t) + c.c.\right). \tag{2.32}$$

where $\hat{\boldsymbol{e}}$ is the vector basis used in a helical system and its complex conjugate $(c.c.)$,

$$\hat{\boldsymbol{e}} \equiv \frac{\hat{\boldsymbol{x}} + i\hat{\boldsymbol{y}}}{\sqrt{2}}\ , \quad \hat{\boldsymbol{e}}^* \equiv \frac{\hat{\boldsymbol{x}} - i\hat{\boldsymbol{y}}}{\sqrt{2}}. \tag{2.33}$$

The two mathematical properties related to $\hat{\boldsymbol{e}}$ are shown below;

$$\hat{\boldsymbol{e}}\cdot\hat{\boldsymbol{e}}^* = 1 \tag{2.34}$$

$$\hat{\boldsymbol{e}}\cdot\hat{\boldsymbol{e}} = 0. \tag{2.35}$$

The complex radiation field envelope is

$$\xi_0(z,t) = |\xi_0(z,t)|\exp\{i\phi(z,t)\} \tag{2.36}$$

where ϕ is the radiation phase.

The wave of the radiation field in equation 2.32 is transverse and there is no $\hat{\boldsymbol{z}}$ component. From figure 2.2, $\xi_0(z,t)$ is the complex envelope and the complex exponential term describes the radiation frequency which is a type of carrier wave. One can substitute $\hat{\boldsymbol{e}}$ into equation 2.32 and expand the radiation field in cartesian form.

$$\boldsymbol{E}(z,t) = \frac{1}{\sqrt{2}}\left(\frac{\hat{\boldsymbol{x}} + i\hat{\boldsymbol{y}}}{\sqrt{2}}\xi_0(\exp i(kz-\omega t) + \frac{\hat{\boldsymbol{x}} - i\hat{\boldsymbol{y}}}{\sqrt{2}}\xi_0(\exp -i(kz-\omega t))\right) \tag{2.37}$$

$$= \xi_0(z,t)\ [\cos(kz-\omega t)\hat{\boldsymbol{x}} - \sin(kz-\omega t)\hat{\boldsymbol{y}}]. \tag{2.38}$$

For the simplification here, the complex conjugate envelope term, ξ_0^*, is equal to ξ_0 but it is not correct in general.

Recall the solutions of the electrons' velocity (in equation 2.11) is:

$$\begin{aligned}\boldsymbol{\beta} &= \beta_x\ \hat{\boldsymbol{x}} + \beta_y\ \hat{\boldsymbol{y}} + \beta_z\ \hat{\boldsymbol{z}} \\ &= -\frac{a_w}{\gamma}\cos(k_w z)\ \hat{\boldsymbol{x}} - \frac{a_w}{\gamma}\sin(k_w z)\ \hat{\boldsymbol{y}} + \beta_{z0}\ \hat{\boldsymbol{z}}. \end{aligned} \tag{2.39}$$

Since the solution of the electrons' velocity is a function of γ, which is a constant, and the radiation field is zero, both of which are in the z-direction, therefore the product of β_z and E_z equals to zero. As a result, when one substitutes both equation 2.38 and 2.39 into equation 2.31, only x and y directions are of interest,

$$\begin{aligned}\dot{\gamma} &= -\frac{e}{mc}\boldsymbol{\beta}\cdot\boldsymbol{E} \\ &= -\frac{e}{mc}\left(-\frac{a_w}{\gamma}\cos(k_w z)\hat{\boldsymbol{x}} - \frac{a_w}{\gamma}\sin(k_w z)\hat{\boldsymbol{y}}\right)\cdot\xi_0(z,t)[\cos(kz-\omega t)\hat{\boldsymbol{x}} - \sin(kz-\omega t)\hat{\boldsymbol{y}}] \\ &= \frac{ea_w}{mc\gamma}\xi_0(z,t)(\cos(k_w z)\cos(kz-\omega t) - \sin(k_w z)\sin(kz-\omega t)) \\ &= \frac{ea_w}{mc\gamma}\xi_0(z,t)\cos[(k_w+k)z-\omega t]. \end{aligned} \tag{2.40}$$

In equation 2.40, the argument of the cosine term must be varying slowly with respect to the radiation period in order for the electrons to have a slow energy exchange with the radiation. The argument term, θ, is define as:

$$\theta = k_w z + kz - \omega t. \tag{2.41}$$

For a slow energy exchange, θ must be approximately constant, therefore differentiating θ with respect to time must equal zero,

$$\frac{\mathrm{d}\theta}{\mathrm{d}t} = 0 \tag{2.42}$$

$$\begin{aligned}\frac{\mathrm{d}}{\mathrm{d}t}(k_w z + kz - \omega t) &= 0 \\ (k_w+k)\frac{\mathrm{d}z}{\mathrm{d}t} - \omega &= 0 \\ (k_w+k)v_z - ck &= 0 \\ (k_w+k)\beta_z - k &= 0. \end{aligned} \tag{2.43}$$

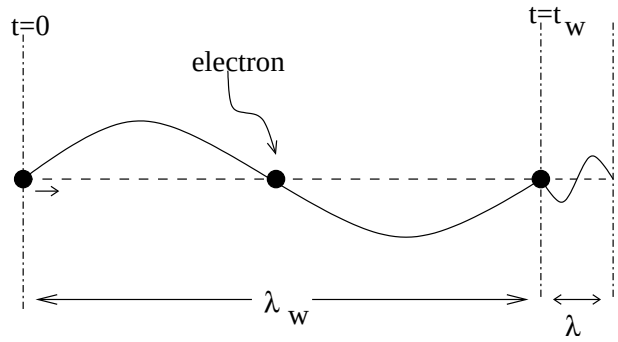

Figure 2.3: A simple sketch illustrating the FEL resonance condition. The resonance condition occurs when one radiation wavelength passes over ('slips') a resonant electron in one wiggler period.

Rearranging equation 2.43 yields a new expression,

$$\frac{\lambda_w}{\lambda} = \frac{\beta_z}{(1-\beta_z)}. \tag{2.44}$$

This is the resonance condition[2] and is the most basic and important concept in FEL Physics. Figure 2.3 schematically describes the concept of the resonance condition. When an electron satisfies this condition, the energy exchange between the radiation and the wiggler field is optimised. Furthermore, this condition demonstrates the tunability of an FEL by changing the electron-beam kinetic energy, therefore the FEL mechanism can be designed to operate over a large range of wavelengths. In reality, there are more factors to be considered in order to adjust to a specified wavelength, such as the quality of the electron beam and the gain of an FEL. The intensity of the radiation is different when the electrons are randomly positioned compared to a pre-bunched electron beam. The process of energy exchange occurs when the resonance condition is satisfied and this leads to electron bunching. These topics are discussed in detail in the next section.

2.3.3 Energy exchange and bunching

Upon entering the undulator, the electrons are randomly spread across the length of the electron beam, see figure 2.4. This random distribution is the source of

[2]There is another way to write the resonance condition. This is calculated by substituting equation 2.18 into equation 2.44 and use the binomial expansion assuming $\gamma \gg 1$. Then only the first order term remains which gives the new form of the resonance condition,

$$\lambda = \frac{\lambda_w(1+a_w^2)}{2\gamma^2}$$

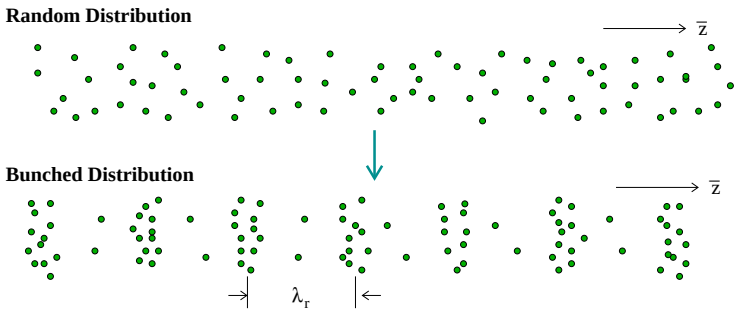

Figure 2.4: Initially electrons are randomly distributed; this is shown at the top. After the FEL interaction the electrons are bunched at a radiation period, at shown in bottom sketch.

shot-noise in the electron beam and it is also the source of the spontaneous radiation in the SASE process. Electron bunching is important in both the gain of an FEL device and for coherent emission which results in high power radiation. The electron beam used in a SASE process contains millions of individual electrons, so the radiated intensity, I, in this randomly distributed environment is proportional to the number of electrons, N where $N \gg 1$. This can be understood by considering the radiation electric field emitted by each electron, E_i, where $i = 1 \ldots N$. In general,

$$I \propto \left(\sum_{i=1}^{N} E_i \right)^2 \tag{2.45}$$

$$\propto \sum_{i=1}^{N} E_i^2 + 2 \sum_{\substack{i,j=1 \\ i \neq j}}^{N} E_{ij}. \tag{2.46}$$

For the case where the phases of the electrons are random, the cross terms will cancel out and there is no correlation between an electron, say E_1, and the fields from other electrons, say $E_2, E_3, \ldots$.

$$\sum_{\substack{i,j=1 \\ i \neq j}}^{N} E_{ij} \simeq 0. \tag{2.47}$$

Due to this incoherent sum of the electric fields the intensity varies directly as N when the electrons are random distributed. When the electrons begin to bunch (in phase) and start to emit coherent radiation over a radiation period, the intensity is now directly proportional to N^2. This is because the cross terms (second term on equation 2.46) are now correlated and become non-zero.

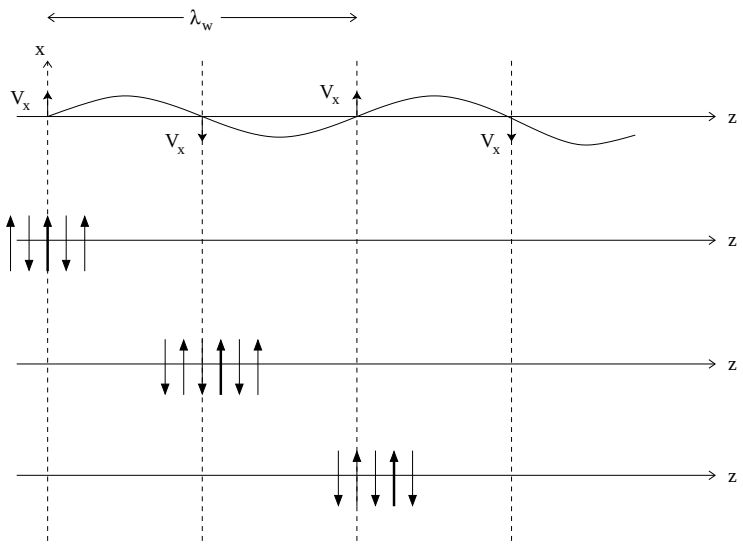

Figure 2.5: A diagram showing the electron trajectory (top z-axis) and the radiation field vector (bottom three z axes) over one wiggler period. After one undulator period, the radiation has propagated one radiation period ahead of the electron while maintaining a slow interaction ($\boldsymbol{E} \cdot \boldsymbol{v} \approx$ constant).

At the beginning of section 2.3, the interaction between the electrons and the radiation during the process of SASE was briefly mentioned. A detailed explanation of the energy exchange between the electrons and the radiation and how the electron bunching occurs is discussed next.

Now consider the radiation, travelling at c, co-propagating with an electron, which travels with axial velocity component $\boldsymbol{v}_{\parallel}$, from the beginning at $t = 0$, see figure 2.5. After one undulator period, λ_w, at $t = \frac{\lambda_w}{v_{\parallel}}$ the radiation has travelled a distance of $\lambda_w + \lambda_r$. Without an undulator there should be no energy exchange between the electromagnetic(EM) field and electron beam which propagates in the same direction because $\boldsymbol{E} \cdot \boldsymbol{v} = 0$. However the electrons' velocity has a transverse component in the presence of an undulator field so there is an interaction between the EM field and the electron beam, $\boldsymbol{E} \cdot \boldsymbol{v} \neq 0$.

During the process of energy exchange, some of the electrons will gain more energy, $\boldsymbol{v} \cdot \boldsymbol{E} < 0$, from the radiation field and they will travel faster than the average electrons. On the other hand, other electrons will lose their energy, $\boldsymbol{v} \cdot \boldsymbol{E} > 0$, to the radiation field and result in falling behind the average electrons. Another way to explain how the energy exchange took place is to use a potential well, Φ. The electrons are sitting inside the potential well initially before the process of energy exchange and figure 2.6 shows the electrons moving inside the well. When the ponderomotive well is driven by the rate of change of the radiation phase, the electrons begin to bunch at the bottom of the well. As Φ is changing,

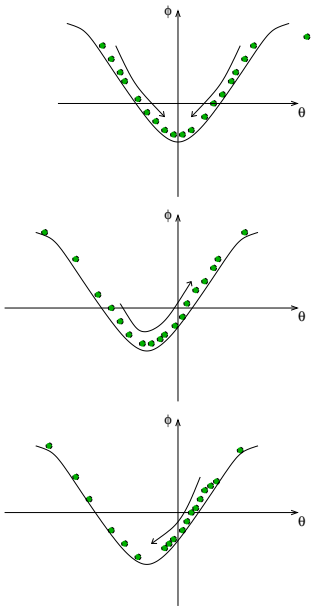

Figure 2.6: A diagram showing how the electrons move inside the potential well as the phase of the potential well changes.

the potential well has shifted away from the centre and the electrons are now sitting on a slope of the well. Subsequently, the electrons are driven by the field intensity and they roll back to the middle of the well and start to 'climb up' to the opposite slope of well, this is when they begin to coherently absorb the energy from the radiation. Most of the electrons continue to oscillate inside the well both absorbing and transmitting energy to the field and some electrons reach the top of the well and fall down to the neighboring potential well. When more and more electrons begin to radiate in phase, this results in an increasingly coherent superposition of the radiation emitted from the micro-bunched electrons. In the FEL interaction region, the intensity of the radiation starts to be exponentially amplified, see figure 2.7, until the electrons are strongly bunched, after which it is over modulated resulting in saturation.

There exists 1D models which study the evolution of the radiation with an infinitely long electron beam and pulses of electrons injected at the beginning of the undulator. The analysis, analytical and numerical results of these two systems are explained in the next two sections.

2.4 Steady State

In a one dimensional FEL case the electron pulse is infinitely long and uniform, and the the slippage effects can be neglected. Under these conditions, the system

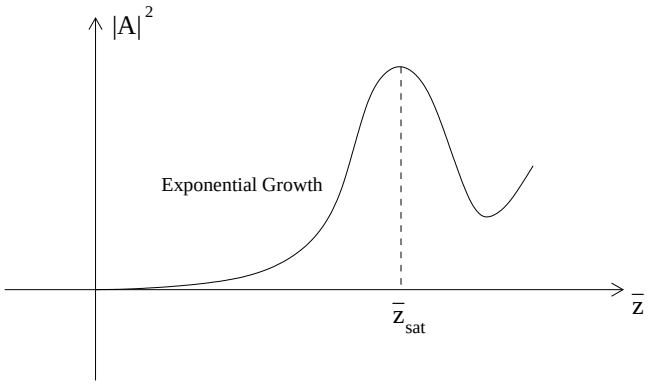

Figure 2.7: The intensity exponentially increases in $\bar{z}$ until it reaches its saturation point, $\bar{z}_{sat}$. At the peak of the intensity the electrons are fully bunched and emit coherent radiation.

is said to be in a "steady state" regime. In that limit, the time derivative in Maxwell's 1D wave equation may be safely ignored and the steady state evolution depends only on the spatial dimension, z.

The parameters and the FEL equations for the steady state regime are set in a dimensionless form. The first and most important parameter in FEL physics is [9]

$$\rho = \frac{1}{\gamma_r}\left(\frac{a_w \omega_p}{4ck_w}\right)^{2/3}. \tag{2.48}$$

This parameter, known as the Pierce parameter, describes the strength of the coupling between field and electrons. Here, ω_p is the plasma frequency for the peak electron number density of the electron pulse, n_p.

$$\omega_p = \sqrt{\frac{e^2 n_p}{\epsilon_0 m}}. \tag{2.49}$$

The forward propagation direction, z, is scaled as:

$$\bar{z} = 2k_w \rho z. \tag{2.50}$$

This is an independent variable and it is also used in the 3D equations which are derived and discussed in section 2.6. From the definition of $\bar{z}$, this is a dimensional length in the range $0 \leq \bar{z} \leq 4\pi\rho N_w$ where N_w is the number of undulator periods. One period in unscaled cartesian co-ordinates is λ_w and $4\pi\rho$ is one period in the scaled system. In the FEL equation the complex radiation envelope is scaled as follows;

$$A = \frac{\omega \xi_0}{\omega_p \sqrt{\rho \gamma_r}} \tag{2.51}$$

where ω is the radiation angular frequency. It should be noted that the fundamental FEL parameter, ρ, appears in all the scalings.

The main study of an FEL is focused in a high-gain Compton regime. This contrasts the low-gain or Raman regime and the main differences between the Compton and Raman are listed below [9],

1. $\rho \ll 1$ for Compton, $\rho \sim 1$ for Raman.

2. Space-charge effect is negligible in Compton but it has a significant effect in Raman.

The structure of the next section is as follows: In a steady-state regime, a linear stability analysis is carried out when a small perturbation is initially added into the FEL system. A dispersion relation is derived and an analytical solution for the radiation field calculated.

2.4.1 Linear Stability Analysis

The SVEA limit was discussed previously in section 2.2.1 and this assumption is, again, applied to the one dimensional wave equation for the steady state regime. The derivative with respect to time in the wave equation is neglected to give the steady-state regime. The resultant FEL equations describing the evolution of the radiation field and the electrons are given by [9],

$$\frac{d\theta_j}{d\bar{z}} = p_j \tag{2.52}$$

$$\frac{dp_j}{d\bar{z}} = -(A\exp\{i\theta_j\} + A^*\exp\{-i\theta_j\}) \tag{2.53}$$

$$\frac{dA}{d\bar{z}} = \langle \exp(-i\theta)\rangle \equiv b. \tag{2.54}$$

The subscript j denotes the j^{th} electron. In equation 2.52, θ describes the electrons' positions within the ponderomotive well and the derivative of θ describes the velocity of the electrons in the well. On the r.h.s. of equation 2.52, p_j is defined as:

$$p_j = \frac{1}{\rho}\frac{\gamma_j - \langle\gamma_0\rangle}{\langle\gamma_0\rangle}. \tag{2.55}$$

The initial condition for p_j, when $\bar{z} = 0$, is $\langle p_0\rangle = \delta$ where δ is known as the detuning parameter. Next, the electron energy equation is written in equation 2.53 and the source term in this equation is a ponderomotive force which drives the electron to either accelerate or decelerate and to bunch. The final equation 2.54

is the field as driven by the electrons and b is defined as the bunching parameter. $\langle\ \rangle$ is defined as the average over a sample of N electrons

$$\langle \ldots \rangle = \frac{1}{N} \sum_{j=1}^{N} (\ldots)_j. \tag{2.56}$$

When the electrons are unbunched $|b| = 0$ and for perfectly bunched $|b| = 1$, therefore the bunching parameter must lie in the range, $0 \leq |b| \leq 1$.

The stability of the state may be investigated by performing a linear stability analysis around the initial value. In equilibrium, the initial conditions are no field excitation and unbunched, the electron beam is monoenergetic,i.e.,

$$A(\bar{z}) = 0, \quad p_j(\bar{z}) = p_{j0} = \delta \quad \theta_j(\bar{z}) = \theta_{j0} + \delta\bar{z} \tag{2.57}$$

where θ_{j0} is uniformly distributed in the interval $0 < \theta < 2\pi$. The linear stability analysis is performed by adding a small perturbation to the three collective variables from the initial state: in general form e.g. f is a function of x,

$$f(x) = f_0 + f_1(x) \tag{2.58}$$

where $f_1(x) \ll 1$ is the small perturbation term and f_0 is the initial value. The following three parts present a method of how the 1D FEL equations is linearised:

$\underline{\theta \ \text{ equation}}$: phase of an electron in the combined ponderomotive field,

$$\frac{d\theta_j}{d\bar{z}} = p_j$$

$$\frac{d\ (\theta_{0j} + \theta_{1j} + \delta\bar{z})}{d\bar{z}} = p_{0j} + p_{1j} \tag{2.59}$$

$$\frac{d\theta_{0j}}{d\bar{z}} + \frac{d\theta_{1j}}{d\bar{z}} = p_{1j} + \delta \tag{2.60}$$

Using the initial conditions for p_{0j} in equation 2.57

$$\delta + \frac{d\theta_{1j}}{d\bar{z}} = p_{1j} + \delta \tag{2.61}$$

$$\frac{d\theta_{1j}}{d\bar{z}} = p_{1j} \tag{2.62}$$

p equation : momentum of an electron,

$$\begin{aligned}\frac{dp_j}{d\bar{z}} &= -(A\exp(i\theta_j) + A^*\exp(-i\theta_j)) \\ \frac{d\ (p_{0j}+p_{1j})}{d\bar{z}} &= -(A\exp\{i(\theta_{0j}+\delta\bar{z}+\theta_{1j})\} + A^*\exp\{-i(\theta_{0j}+\delta\bar{z}+\theta_{1j})\})\end{aligned} \tag{2.63}$$

$$\begin{aligned}\text{Since } \exp\{x\} \simeq 1+x \text{ when } x \ll 1 \\ = -(A(1+i\theta_{1j})\exp\{i(\theta_{0j}+\delta\bar{z})\} + A^*(1-i\theta_{1j})\exp\{-i(\theta_{0j}+\delta\bar{z})\})\end{aligned} \tag{2.64}$$

$$\text{As } A \text{ and } \theta_{1j} \ll 0, \text{ so } A\ \theta_{1j} \ll 0, \text{ this term may be neglected.}$$

$$\frac{dp_{1j}}{d\bar{z}} = -(A\exp\{i(\theta_{0j}+\delta\bar{z})\} + A^*\exp\{-i(\theta_{0j}+\delta\bar{z})\}) \tag{2.65}$$

A equation : complex field envelope,

$$\begin{aligned}\frac{dA}{d\bar{z}} &= \langle\exp(-i\theta)\rangle \\ \frac{d\ (A_0+A_1)}{d\bar{z}} &= \langle\exp\{-i(\theta_0+\delta\bar{z})\}(1-i\theta_1)\rangle \qquad (2.66) \\ \frac{dA_1}{d\bar{z}} &= -i\theta_1\langle\exp\{-i(\theta_0+\delta\bar{z})\}\rangle. \qquad (2.67)\end{aligned}$$

As the electrons are assumed to be randomly distributed in phase, $\langle\exp\{-i(\theta_0+\delta z)\}\rangle = \exp\{-i\delta\bar{z}\}\langle\exp\{-i\theta_0\}\rangle = 0$. The next step is to average equation 2.62 and 2.65:

$$\begin{aligned}\frac{d\langle\theta_1\rangle}{d\bar{z}} &= \langle p_1\rangle \qquad (2.68) \\ \frac{d\langle p_1\rangle}{d\bar{z}} &= -(A\langle\exp\{i(\theta_0+\delta\bar{z})\}\rangle + A^*\langle\exp\{-i(\theta_0+\delta\bar{z})\}\rangle) \qquad (2.69)\end{aligned}$$

A simple cubic equation can be derived by successively differentiating equation 2.67, then equations 2.68 and 2.69 are substituted. Differentiate equation 2.67 once to yield the second order derivatives of A;

$$\frac{d^2A_1}{d\bar{z}^2} = -i\langle p_{1j}\exp\{-i(\theta_{0j}+\delta\bar{z})\} - i\delta\theta_1\exp\{-i(\theta_{0j}+\delta\bar{z})\}\rangle \tag{2.70}$$

and the third order derivatives is;

$$\begin{aligned}\frac{d^3A_1}{d\bar{z}^3} = -i\langle -A^*\exp\{-2i(\theta_{0j}+\delta\bar{z})\} - 2\delta p_1\exp\{-i(\theta_{0j}+\delta\bar{z})\} \\ - \delta^2\theta_1\exp\{-i(\theta_{0j}+\delta\bar{z})\}\rangle\end{aligned} \tag{2.71}$$

Using equations 2.67, 2.70 and 2.71, the cubic differential equation of A is,

$$\frac{d^3A_1}{d\bar{z}^3} + 2i\delta\frac{d^2A_1}{d\bar{z}^2} - \delta^2\frac{dA_1}{d\bar{z}} = iA_1 \tag{2.72}$$

The solution of equation 2.72 is assumed to be in this form: $A_1(\bar{z}) = A_1(0)\exp(i\lambda\bar{z})$ and this is substituted into equation 2.72. An equation for the linear dynamics of the field was derived as a result,

$$\lambda^3 + 2\delta\lambda^2 + \delta^2\lambda + 1 = 0 \tag{2.73}$$

This third-order polynomial of λ is obtained and is known as the dispersion relation. The solutions of λ are determined by solving equation 2.73 and substituting them back into a general form of A:

$$A(\bar{z}) = A(0)\sum_{k=1}^{3} C_k \exp(i\lambda_k\bar{z}) \tag{2.74}$$

The dispersion relation clearly has three solutions and the system is stable when all three roots are real. If one of the roots is real ($\lambda = \lambda_1$) and the other two roots are complex-conjugate ($\lambda_{2,3} = x \pm iy$) the system is unstable and the field amplitude would grow exponentially along the undulator. The analytical solution for A is

$$A(\bar{z}) = \frac{A(0)}{3}\left[\exp\left(\frac{i\bar{z}}{2}\right)\left(\exp\left(\frac{\sqrt{3}}{2}\bar{z}\right) + \exp\left(-\frac{\sqrt{3}}{2}\bar{z}\right)\right) + \exp(-i\bar{z})\right] \tag{2.75}$$

Figure 2.8 shows a sketch of all three solutions and when $\overline{z} \ll 1$, solution (II) does not have much impact on the solution and the other two will dominate the solution equally. As $\overline{z} \geq 1$, where it is sufficiently large enough, (II) is now the dominant one and the other two have much less impact.

2.5 Coherent Spontaneous Emission

While the steady-state interaction FEL of the previous section is useful to demonstrate the FEL instability, it is impractical to have a uniform electron beam that is infinitely long. Pulses of electrons are normally used and the field amplitude is then dependent on time, t, where this variable was neglected in the steady-state regime, and the propagation direction, z. The output intensity at any position along the undulator now varies with time and, generally, the SVEA does not ap-

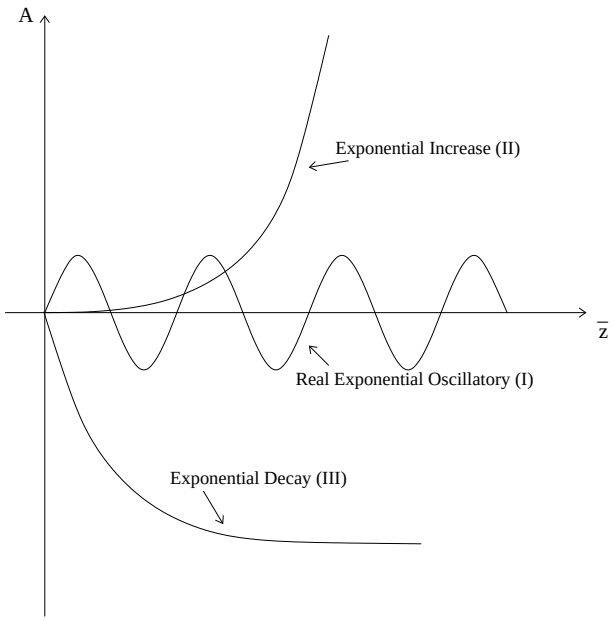

Figure 2.8: Sketch of the linear solutions of the radiation envelope: real exponential oscillatory (I), exponential increase (II) and exponential decrease (III).

ply in this case. A new set of FEL equations must be derived for the FEL pulse interaction and the equations are discussed in the next section.

2.5.1 Equations in the 1-D limit

When electron pulses travel through an undulator, it is important to include the independent parameter t in Maxwell's wave equation. A numerical approach has been chosen to derive the solution using a Finite Element Method (FEM).

The FEL pulse interaction equations began with Maxwell's wave equation and the Lorentz force equation and then followed by universal scaling. The independent variables, $(z,\, t)$, are re-scaled from the stationary rest frame to the electrons' rest frame, $(\overline{z},\, \overline{z}_1)$. The scaled propagation direction is shown in equation 2.50 and the time variable is scaled as

$$\bar{z}_1 = \frac{2k_w\rho}{1-\bar{\beta}_z}\left(z - c\bar{\beta}_z t\right) \tag{2.76}$$

When an observer is in the stationary frame they would 'see' the field and electrons' motion changing with time. With the new $\bar{z}_1$ independent variable, an observer in the electron frame, travelling along with the electrons, observes the radiation moving and the electrons stationary. There is also a counter-propagating pseudo-radiation generated by the undulator field that the electrons would 'see'. The final form of the FEL pulse equations after all the mathematical manipula-

tion gives:

$$\left(\frac{\partial}{\partial\bar{z}}+\frac{\partial}{\partial\bar{z}_1}\right)A=\frac{\alpha}{2\rho}\frac{1}{\bar{n}_{p\|}}\sum_{j=1}^{N}\exp\left\{-i\frac{(\bar{z}_{1j}-\bar{z})}{2\rho}\right\}\frac{\bar{p}_{\perp j}}{(1+|\bar{p}_{\perp j}|^2)^{1/2}}$$
$$(\varepsilon Q_j(\epsilon Q_j+2))^{\frac{1}{2}}\,\delta(\bar{z}_1-\bar{z}_{1j}(\bar{z})) \tag{2.77}$$

$$\frac{d\bar{p}_{\perp j}}{d\bar{z}}=\frac{a_w}{2\rho}\left[i\exp\left\{-i\frac{\bar{z}}{2\rho}\right\}-\alpha^2\varepsilon Q_j\left(A\exp\left\{\frac{i(\bar{z}_{1j}-\bar{z})}{2\rho}\right\}+c.c\right)\right] \tag{2.78}$$

$$\frac{dQ_j}{d\bar{z}}=\frac{a_w}{4\rho}\frac{Q_j(\varepsilon Q_j+2)}{1+|\bar{p}_{\perp j}|^2}\Bigg[i(\varepsilon Q_j+1)\left(\bar{p}^*_{\perp j}\exp\left\{-ik_wz\right\}-c.c\right)+$$
$$\alpha^2\varepsilon Q_j(\bar{p}^*_{\perp j}A\exp\left\{i\frac{\bar{z}_{1j}-\bar{z}}{2\rho}\right\}+c.c)\Bigg] \tag{2.79}$$

$$\frac{d\bar{z}_{1j}}{d\bar{z}}=1-Q_j \tag{2.80}$$

where

$$\alpha=\frac{2\rho\gamma_r}{a_w} \tag{2.81}$$

$$\varepsilon=\frac{1-\bar{\beta}_z}{\bar{\beta}_z} \tag{2.82}$$

$$\bar{n}_{p\|}=\frac{n_p\sigma\varepsilon}{2\rho k_w} \tag{2.83}$$

$\bar{n}_{p\|}$ is the peak number of electrons per unit $\bar{z}_1$, σ is the cross-sectional area of the electron beam.

It is useful at this point to give a brief explanation of how the equations are stored, the numerical methods used to solve the 1D FEL equations, post-processing and plotting of the results is given.

In the simulation code, the FEL pulse equations are stored into a column vector to save computational time when carrying out the integration. The equation for the scaled field, A, is a partial differential equation hence there is not a single analytical method to solve this equation. A numerical method called the FEM was used to solve this field equation which estimates the best possible solution. There are many types of FEM, and the Streamline Diffusion method was applied in equation 2.77. One of the NAG (Numerical Algorithms Group [21]) library routines was implement on the field equation, converted the l.h.s. into a sparse matrix and then integrated along with other equations using rk4. The output results were post-analysed using a Tcl script program which uses the

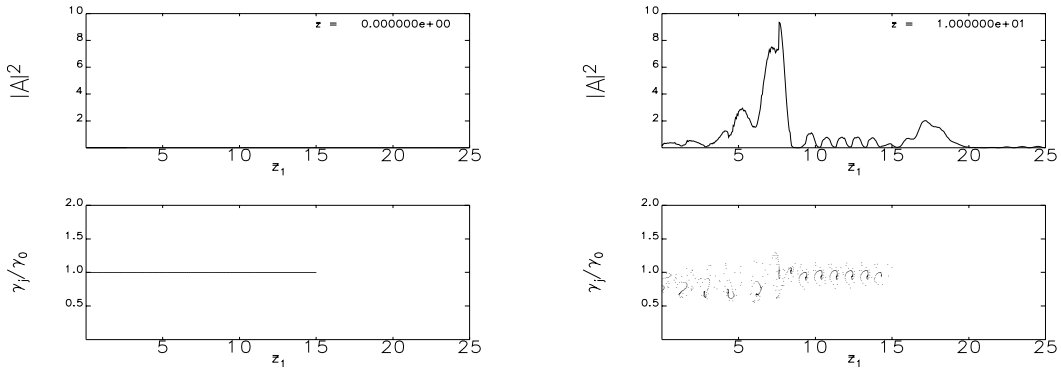

(a) $\bar{z}$=0 (b) $\bar{z}$=10

Figure 2.9: The electron pulse length is $\ell_e = 15$ in the electron rest frame. At $\bar{z} = 0$, in 2.9(a), the intensity is zero (top) and the electrons' phase (bottom) are uniform with $\gamma = \gamma_0$. At $\bar{z} = 10$, in 2.9(b), the intensity (top) has grown exponentially to saturation. The electrons have bunched at the radiation period as shown in the phase-space (bottom).

SDDS toolkit [22] to produce a movie of the intensity varying in the electron rest frame, the electrons' trajectory in phase-space and a plot of the intensity along the undulator.

The analysis of the results is discussed below. Figures 2.9(a) and 2.9(b) are the first and last frame for an interaction length $\bar{z} = 10$. The intensity and the phase-space of a simulation which has length of electron beam pulse $\ell_e = 15$ in units of $\bar{z}_1$. Figure 2.9(a) shows the system's initial condition before any interaction and at $\bar{z} = 10$ the intensity has grown then saturated and the electrons have bunched which can be seen in figure 2.9(b). Furthermore, there are two regions where the field evolves in different ways and an understanding of these regions is also very important in the three-dimensional FEL study. The first region is called the slippage region, which lies in $(0 < \bar{z}_1 < \bar{z} = 10)$ where the radiation emitted from the tail electrons at the entrance of the undulator has propagated to $\bar{z}_1 = 10$. In this region the radiation is not steady-state since there is no radiation entering the electron pulse from behind $\bar{z}_1 < 0$. The radiation emitted from this region exhibits pulse like effects and can lead to superradiance [23]. From $\bar{z} = 10 < \bar{z}_1 < \ell_e$ the radiation is more uniform over the pulse and the electrons evolves identically; this is the steady-state region which was discussed previously. There are no slippage effects and the electrons interact with the radiation continuously where the radiation is coming from the slippage region. Any radiation beyond $15 = \ell_e < \bar{z}_1$ is freely propagated in the vacuum since the electrons only exist between $0 < z_1 < \ell_e$ and no FEL interaction occurs in this

region.

2.5.2 Superradiance

Results in the previous section, when pulses of electrons are injected in the FEL system, show that the radiation evolved in three different regions: steady-state, discussed in section 2.4, vacuum region and slippage region. The radiation in the slippage region evolved differently from the steady-state regime to give another region that an FEL may operate in called the superradiant regime.

In this regime the radiated power is proportional to N^2 compared to $N^{4/3}$ in the steady-state case. It was initially thought that in order to achieve the superradiant effect a short electron pulse was required. However numerical and analytical results have shown [24, 25, 26] that the effect can also occur in the tail of a long electron pulse. An electron pulse is defined as long or short with respect to the cooperation length, l_c. l_c is the slippage length in one gain length, l_g. l_g is the distance through the undulator such that $\Delta\bar{z} = 1$. In the three dimensional equations of section 2.6, all three spatial and temporal variables are scaled using l_g and l_c. The intensity of the emitted radiation in a system where the electrons are randomly distributed with no input signal is proportional to N, whereas in a pre-bunched system the intensity scales as N^2. Superradiance is spontaneous emission from a coherently prepared system as defined by Dicke [27]. When the electrons enter the undulator there is shot-noise in the electron beam and $I \propto N$ then the electrons begin to interact with the spontaneous radiation/undulator field and bunch together. In the steady-state the radiation power scales as $N^{4/3}$ whereas in the slippage, as superradiant region, the power scales as N^2.

At the slippage region in the tail of a long electron pulse, the electrons evolve as a short electron pulse as there is no radiation entering from behind, since the emitted radiation propagates forward. A spiking behavior was displayed in this trailing region and the intensities are much greater than the steady-state saturation point as shown results in section 2.5.1. This phenomenon is called the strong superradiance and the other effect, which is emitted by a short electron pulse, is weak superradiance. In the short-pulse limit, as the electron pulse travels at a velocity less than the speed of light, the radiation escapes from the head of the electron pulse and experiences an exponential growth up to a peak. Continuous energy extraction of the electrons takes place in weak superradiance as there is little reabsorption of the radiation.

In the next section, derivations of the FEL equations for a 3D model are shown, first, that includes the wave equation, electron momentum equations,

electron axial equations and the new scalings parameters are used in the transverse direction. Subsequently the initial conditions of the electrons, an equation for the conservation of energy are derived in this order. The theory of matched beam electron and diffraction are discussed and finally, a summary of the input file used in the simulator and the outline of how the simulation code works is explained.

2.6 Analytical theory on the new 3D model

One of the main objectives of this thesis is to derive a new set of equations to describe a three dimensional system which includes the effects of betatron motion, matched beam, diffraction and FEL interaction. These effects will be described later in this section. The mathematics of the equations in this section covers all these areas starting from Maxwell's wave equation and the Lorentz equation.

2.6.1 Maxwell's wave equation and Lorentz force equation

The first equation is the three dimensional Maxwell wave equation and it may be written as

$$\nabla^2 \boldsymbol{E} - \frac{1}{c^2}\frac{\partial^2 \boldsymbol{E}}{\partial t^2} = -\frac{\mu_0 e}{m}\frac{\partial}{\partial t}\sum_{j=1}^{N}\frac{\boldsymbol{p}_j}{\gamma_j}\delta^3(x,y,z) \tag{2.84}$$

where $\nabla^2 \equiv \dfrac{\partial^2}{\partial x^2} + \dfrac{\partial^2}{\partial y^2} + \dfrac{\partial^2}{\partial z^2}$, $\delta^3(x,y,z) = \delta(x-x_j)\delta(y-y_j)\delta(z-z_j)$ and the complex radiation field, $\boldsymbol{E}$, is defined as

$$\boldsymbol{E} = \frac{1}{\sqrt{2}}(\widehat{\boldsymbol{e}}\ \xi_0 \exp\{i(kz-\omega t)\} + c.c.). \tag{2.85}$$

ξ_0 is a complex envelope of the radiation field and the exponential term describes the fast carrier frequency. $\widehat{\boldsymbol{e}}$ was defined in equation 2.33 in section 2.3.2. Equation 2.84 is written in the absence of space-charge terms which are neglected. This radiation depends on three spatial dimensions, x, y, z and time, t. On the r.h.s. of the equation, $\mu_0 = 4\pi \times 10^{-7}$ Vs/Am is the permeability of free space. e is the electron charge with the value of $\simeq 1.6021773 \times 10^{-19}$ C and its mass $m \simeq 9.10939 \times 10^{-31}$ kg. The summation adds up the source term for all the particles, from particle $j = 1$ to $j = N$. Each particle's momentum represented as $\boldsymbol{p}_j$ and γ_j is the relativistic factor defined in equation 2.12. The existence of a particle is described by the Dirac δ function: that is, a particle is located at a single point.

The Maxwell wave equation was introduced and the equation that describes how an electromagnetic force acts upon a particle is the Lorentz force equation:

$$\boldsymbol{F} = -e(\boldsymbol{E} + \boldsymbol{v} \times \boldsymbol{B}) \tag{2.86}$$

where $\boldsymbol{F}$ is the Lorentz force acting upon a particle of instantaneous velocity $\boldsymbol{v}$.

The magnetic $\boldsymbol{B}$ field is

$$\boldsymbol{B} = \frac{B_w}{\sqrt{2}}(\widehat{\boldsymbol{e}}\ \exp\{-ik_w z\} + c.c.) - \frac{i}{\sqrt{2}}\left(\widehat{\boldsymbol{e}}\ \frac{\xi_0}{c}\exp\{i(k_w z - \omega t)\} - c.c.\right) \quad (2.87)$$

and consists of the undulator magnetic field and the magnetic field of the radiation found from the Maxwell equation [20];

$$\nabla \times \boldsymbol{E} = -\frac{\partial \boldsymbol{B}}{\partial t}. \quad (2.88)$$

A discussion on how the new scaling parameters are used in the 3D FEL equations is presented in the next section. They are then applied to the equations in section 2.6.3.

2.6.2 Scaled parameters

In section 2.4 the forward propagation direction, z, scaling was defined in equation 2.50. The range of $\bar{z}$ in one undulator period is $4\pi\rho$. The other independent parameter in the one dimensional example was $\bar{z}_1$ in equation 2.76, which is set in the electron rest frame. Interestingly, there is a relationship between $\bar{z}$ and $\bar{z}_1$ which is linked by another dimensionless variable, $\bar{z}_2$, which is set in the radiation rest frame:

$$\bar{z} = \bar{z}_1 + \bar{z}_2. \quad (2.89)$$

$$\text{where } \bar{z}_2 = 2k_w\rho\frac{\bar{\beta}_z}{1-\bar{\beta}_z}(ct - z) \quad (2.90)$$

where $\bar{z}$ and $\bar{z}_1$ are already defined in equation 2.50 and 2.76 respectively. $c\bar{\beta}_z = \bar{v}_z$ is the mean axial relativistic velocity and $k_w = \dfrac{2\pi}{\lambda_w}$ is the wave number of the undulator. The independent parameter $\bar{z}_2$ is used in the three dimensional simulation code.

The Pierce parameter was defined in equation 2.48, which is specifically for a helical undulator whereas for a planar wiggler,

$$\rho \equiv \frac{1}{\gamma_r}\left(\frac{a_w\omega_p f_B}{4ck_w}\right)^{2/3} \quad (2.91)$$

where the factor f_B for a planar wiggler is terms of the Bessel function[3]. When ρ is small, say $\rho \ll 1$, the interaction time of the energy exchange between the

[3]For a planar wiggler $f_B = J_0(\zeta) - J_1(\zeta)$ where $\zeta = a_w^2/2(1+a_w^2)$[28]

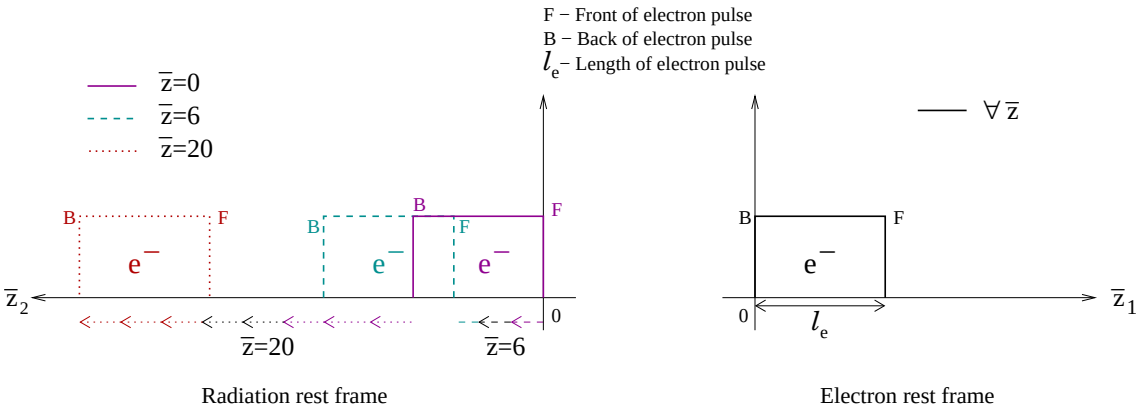

Figure 2.10: On the right, the electron pulse (ℓ_e) is in the electron rest frame ($\bar{z}_1$) and it remains at the same position for all $\bar{z}$. On the left is the radiation frame ($\bar{z}_2$). The electron pulse (ℓ_e) moves "backwards" from $\bar{z} = 0$ to $\bar{z} = 20$.

field and the electrons is short since the electrons are travelling near the speed of light. An explanation below discusses the difference between $\bar{z}_1$ and $\bar{z}_2$ frames.

$\bar{z}_2$ is set in the radiation reference frame where an observer is 'sitting' in a frame travelling at c, the speed of light. The electrons would then appear to travel backwards with respect to the observer. Figure 2.10 is a schematic diagram showing the difference between the electron and the radiation reference frame. The electron pulse would always be at the same position in $\bar{z}_1$ frame whereas the electron pulse travels backwards in $\bar{z}_2$ frame.

The next step is to define a scaling for the transverse plane and they are related to the concepts of gain length (l_g) and cooperation length (l_c), which were briefly mentioned in section 2.5.2. These two variables are a convenient way to understand the scaling. The scaled variables are often referred to in terms of l_g and l_c and they are related to the wavelength of an undulator and radiation respectively,

$$l_g = \frac{\lambda_w}{4\pi\rho} \tag{2.92}$$

$$l_c = \frac{\lambda_r}{4\pi\rho}. \tag{2.93}$$

A second way to explain the scaled propagation direction $\bar{z}$ is that z is scaled with respect to the l_g.

$$\bar{z} = \frac{z}{l_g}. \tag{2.94}$$

In the transverse plane, x and y are also scaled such that they also become

dimensionless lengths. The scaled transverse variables are given by,

$$\bar{x} = \frac{x}{\sqrt{l_g l_c}} \tag{2.95}$$

$$\bar{y} = \frac{y}{\sqrt{l_g l_c}}. \tag{2.96}$$

All the independent parameters have been defined and the next variable is the complex radiation field envelope, ξ_0. This is scaled to A, which is a slightly different scaling from equation 2.51. The new scaled envelope is given by:

$$A = \frac{e\xi_0}{mc\omega_p\sqrt{\gamma_r\rho}}. \tag{2.97}$$

In addition some definitions related to momentum are listed in the following;

$$p_\perp \equiv p_x - ip_y \tag{2.98}$$

$$\text{where } p_x = \frac{1}{2}(p_\perp + p_\perp^*) \tag{2.99}$$

$$p_y = \frac{i}{2}(p_\perp - p_\perp^*) \tag{2.100}$$

$$\boldsymbol{p}_j \cdot \widehat{\boldsymbol{e}} = \frac{p_{\perp j}^*}{\sqrt{2}}, \quad \boldsymbol{p}_j^* \cdot \widehat{\boldsymbol{e}}^* = \frac{p_{\perp j}}{\sqrt{2}} \tag{2.101}$$

$$p_x = \Re(p_{\perp j}), \quad p_y = -\Im(p_{\perp j}) \tag{2.102}$$

All the scaled parameters have been defined and these are now applied to the FEL equations in section 2.6.3.

2.6.3 Maxwell's wave equation

The first step of the scaling processes is to multiply the wave equation 2.84 by a vector basis $\boldsymbol{e}^*$, which is defined in equation 2.33:

$$\left[\nabla^2\boldsymbol{E} - \frac{1}{c^2}\frac{\partial^2\boldsymbol{E}}{\partial t^2}\right] \frac{(\hat{\boldsymbol{x}} - i\hat{\boldsymbol{y}})}{\sqrt{2}} = -\frac{\mu_0 e}{m}\frac{\partial}{\partial t}\sum_{j=1}^{N}\frac{\boldsymbol{p}_j}{\gamma_j}\delta^3(x,y,z)\,\frac{(\hat{\boldsymbol{x}} - i\hat{\boldsymbol{y}})}{\sqrt{2}} \tag{2.103}$$

$$\frac{1}{\sqrt{2}}\left[\nabla^2 - \frac{1}{c^2}\frac{\partial^2}{\partial t^2}\right]\xi_0\exp\{i(kz-\omega t)\} = -\frac{\mu_0 e}{\sqrt{2}m}\frac{\partial}{\partial t}\sum_{j=1}^{N}\frac{p_{\perp j}}{\gamma_j}\delta^3(x,y,z) \tag{2.104}$$

The mathematics for the change of variables $(z,t) \rightarrow (\bar{z},\bar{z}_2)$ have most of the changes and x and y scaling are neglected temporarily. Taking the partial deriva-

tives on the l.h.s. of equation 2.104 and transforming z and t to $\bar{z}, \bar{z}_2$ to obtain

$$\begin{aligned}
&\text{l.h.s. of eqn. 2.104} \\
&= \frac{1}{\sqrt{2}}\left(\frac{\partial^2}{\partial z^2} - \frac{1}{c^2}\frac{\partial^2}{\partial t^2}\right)\xi_0 \exp\{i(kz-\omega t)\} && (2.105)\\
&= \frac{1}{\sqrt{2}}\left(\frac{\partial}{\partial z} + \frac{1}{c}\frac{\partial}{\partial t}\right)\left(\frac{\partial}{\partial z} - \frac{1}{c}\frac{\partial}{\partial t}\right)\xi_0 \exp\{i(kz-\omega t)\} && (2.106)\\
&= \frac{4k_w^2\rho^2}{\sqrt{2}}\frac{\partial}{\partial \bar{z}}\left(\frac{\partial}{\partial \bar{z}} - \frac{2\bar{\beta}_z}{1-\bar{\beta}_z}\frac{\partial}{\partial \bar{z}_2}\right)\xi_0 \exp\left\{-i\frac{\bar{z}_2}{2\rho}\right\} && (2.107)
\end{aligned}$$

where one used: $\begin{cases} \frac{\partial}{\partial z} = 2k_w\rho\left(\frac{\partial}{\partial \bar{z}} - \frac{\bar{\beta}_z}{1-\bar{\beta}_z}\frac{\partial}{\partial \bar{z}_2}\right) \\ \frac{\partial}{c\partial t} = 2k_w\rho\frac{\bar{\beta}_z}{1-\bar{\beta}_z}\frac{\partial}{\partial \bar{z}_2} \\ kz-\omega t = -\frac{\bar{z}_2}{2\rho} \end{cases}$

The second bracketed term in equation 2.107 is expanded and so the l.h.s. may be written as:

$$\begin{aligned}
&= \frac{4k_w^2\rho^2}{\sqrt{2}}\frac{\partial}{\partial \bar{z}}\left(\frac{\partial \xi_0}{\partial \bar{z}} - \frac{2\bar{\beta}_z}{1-\bar{\beta}_z}\left(-\frac{i}{2\rho}\xi_0 + \frac{\partial \xi_0}{\partial \bar{z}_2}\right)\right)\exp\left\{-i\frac{\bar{z}_2}{2\rho}\right\} && (2.108)\\
&= \frac{4k_w^2\rho^2}{\sqrt{2}}\exp\left\{-i\frac{\bar{z}_2}{2\rho}\right\}\left(\frac{\partial^2 \xi_0}{\partial \bar{z}^2} + \frac{i}{\rho}\frac{\bar{\beta}_z}{1-\bar{\beta}_z}\frac{\partial \xi_0}{\partial \bar{z}} - \frac{2\bar{\beta}_z}{1-\bar{\beta}_z}\frac{\partial^2 \xi_0}{\partial \bar{z}\partial \bar{z}_2}\right). && (2.109)
\end{aligned}$$

The next step in the calculation is to apply the "complex envelope approximation" to the wave equation. The wavefront of the complex envelope propagating along $\bar{z}_2$ is approximated as a constant for small angles from the z axis therefore the following assumptions can be made.

$$\begin{aligned}
\frac{\partial \xi_0}{\partial z} &= 2k_w\rho\frac{\partial}{\partial \bar{z}}\xi_0(\bar{z}, \bar{z}_2 \approx \text{ constant }) && (2.110)\\
\frac{\partial^2 \xi_0}{\partial z^2} &= (2k_w\rho)^2\frac{\partial^2 \xi_0}{\partial \bar{z}^2}. && (2.111)
\end{aligned}$$

The second bracketed term in equation 2.109 can be re-written as,

$$\begin{aligned}
\frac{i}{\rho}\frac{\bar{\beta}_z}{(1-\bar{\beta}_z)}\frac{\partial \xi_0}{\partial \bar{z}} &= \frac{i}{\rho}\frac{k}{k_w}\frac{\partial \xi_0}{\partial \bar{z}} && (2.112)\\
&= \frac{2ik}{2k_w\rho}\frac{\partial \xi_0}{\partial \bar{z}} && (2.113)\\
&= \frac{2ik}{(2k_w\rho)^2}\frac{\partial \xi_0}{\partial z}. && (2.114)
\end{aligned}$$

Compare the first bracketed term in equation 2.109 with equation 2.114 and then

use equation 2.111 to form an approximation;

$$\left|\frac{\partial^2\xi_0}{\partial\bar{z}^2}\right| \ll \left|\frac{i}{\rho}\frac{\bar{\beta}_z}{1-\bar{\beta}_z}\frac{\partial\xi_0}{\partial\bar{z}}\right| \tag{2.115}$$

$$\left|\frac{1}{(2k_w\rho)^2}\frac{\partial^2\xi_0}{\partial z^2}\right| \ll \left|\frac{2ik}{(2k_w\rho)^2}\frac{\partial\xi_0}{\partial z}\right| \tag{2.116}$$

$$\left|\frac{\partial^2\xi_0}{\partial z^2}\right| \ll 2k\left|\frac{\partial\xi_0}{\partial z}\right| \tag{2.117}$$

An approximation the "complex envelope approximation", which was mentioned in section 2.2.1, has been applied in equation 2.117. The second order partial derivatives of $\bar{z}$ in equation 2.109 can be neglected as a result of this approximation. The transverse component of the field envelope is unchanged hence the l.h.s. of the wave equation has reduced to:

$$\frac{1}{\sqrt{2}}\left[\frac{\partial^2\xi_0}{\partial x^2}+\frac{\partial^2\xi_0}{\partial y^2}+4k_w^2\rho^2\frac{\bar{\beta}_z}{1-\bar{\beta}_z}\left(\frac{i}{\rho}\frac{\partial\xi_0}{\partial\bar{z}}-2\frac{\partial^2\xi_0}{\partial\bar{z}\partial\bar{z}_2}\right)\right]\exp\left\{-i\frac{\bar{z}_2}{2\rho}\right\}. \tag{2.118}$$

Next, the source term on the r.h.s. of the wave equation 2.104 is scaled in terms of $\bar{z}$ and $\bar{z}_2$:

$$\begin{aligned}
\text{r.h.s.} &= -\frac{\mu_0 e}{\sqrt{2}m}\frac{\partial}{\partial t}\sum_{j=1}^{N}\frac{p_{\perp j}}{\gamma_j}\ \delta^3(x,y,z) \\
&= -\frac{e}{\sqrt{2}\epsilon_0 mc^2}\frac{\partial}{\partial t}\sum_{j=1}^{N}\frac{p_{\perp j}}{\gamma_j}\ \delta^3(x,y,z) \quad \text{where } \mu_0=\frac{1}{\epsilon_0 c^2} \\
&= -\frac{e}{\sqrt{2}\epsilon_0 mc}2k_w\rho\frac{\bar{\beta}_z}{1-\bar{\beta}_z}\frac{\partial}{\partial\bar{z}_2}\sum_{j=1}^{N}\frac{p_{\perp j}}{\gamma_j}\frac{2k_w\rho}{\beta_{zj}}\frac{\bar{\beta}_z}{1-\bar{\beta}_z}\delta(x-x_j)\delta(y-y_j)\delta(\bar{z}_2-\bar{z}_{2j}) \\
&= -\frac{e}{\sqrt{2}\epsilon_0 mc}\left(\frac{\bar{\beta}_z}{1-\bar{\beta}_z}\right)^2 4k_w^2\rho^2\frac{\partial}{\partial\bar{z}_2}\sum_{j=1}^{N}\frac{p_{\perp j}}{\beta_{zj}\gamma_j}\delta^3(\bar{x},\bar{y},\bar{z}_2).
\end{aligned} \tag{2.119}$$

Appendix A has the detailed calculations on the δ transformation manipulation.

Now, gather equation 2.118 and 2.119 to form the wave equation, both sides of which have a common factor of

$$\frac{1}{\sqrt{2}}4k_w^2\rho^2\frac{\bar{\beta}_z}{1-\bar{\beta}_z}.$$

This is factored out across the full wave equation to give:

$$\frac{1-\bar{\beta}_z}{\bar{\beta}_z}\frac{1}{4k_w^2\rho^2}\left(\frac{\partial^2\xi_0}{\partial x^2}+\frac{\partial^2\xi_0}{\partial y^2}\right)+\frac{i}{\rho}\frac{\partial\xi_0}{\partial\bar{z}}-2\frac{\partial^2\xi_0}{\partial\bar{z}\partial\bar{z}_2}$$
$$=-\frac{e}{\epsilon_0 mc}\frac{\bar{\beta}_z}{1-\bar{\beta}_z}\exp\left\{i\frac{\bar{z}_2}{2\rho}\right\}\frac{\partial}{\partial\bar{z}_2}\sum_{j=1}^{N}\frac{p_{\perp j}}{\beta_{zj}\gamma_j}\delta^3(x,y,\bar{z}_2). \tag{2.120}$$

Further factoring $\frac{i}{\rho}$ across equation 2.120 and apply the resonance condition $\frac{1-\bar{\beta}_z}{\bar{\beta}_z}=\frac{\lambda_r}{\lambda_w}$ gives:

$$-\frac{i}{4kk_w\rho}\left(\frac{\partial^2\xi_0}{\partial x^2}+\frac{\partial^2\xi_0}{\partial y^2}\right)+\frac{\partial\xi_0}{\partial\bar{z}}+2i\rho\frac{\partial^2\xi_0}{\partial\bar{z}\partial\bar{z}_2}$$
$$=\frac{e}{\epsilon_0 mc}\,i\rho\,\frac{\bar{\beta}_z}{1-\bar{\beta}_z}\exp\left\{i\frac{\bar{z}_2}{2\rho}\right\}\frac{\partial}{\partial\bar{z}_2}\sum_{j=1}^{N}\frac{p_{\perp j}}{\beta_{zj}\gamma_j}\delta^3(x,y,\bar{z}_2). \tag{2.121}$$

The definitions of x and y are given in equation 2.95–2.96: the reason they are scaled with respect to l_g and l_c is because the coefficient in front of the partial derivatives of x and y would become only ρ dependent.

So the second order partial derivative of x,

$$\frac{\partial^2}{\partial x^2}=\frac{1}{l_g l_c}\frac{\partial^2}{\partial\bar{x}^2} \tag{2.122}$$

and it is the same for y. The terms of the x and y derivatives become;

$$\begin{aligned}
&-\frac{i}{4kk_w\rho}\,\frac{1}{l_g\,l_c}\left(\frac{\partial^2\xi_0}{\partial\bar{x}^2}+\frac{\partial^2\xi_0}{\partial\bar{y}^2}\right)\\
=\;&-\frac{i}{4kk_w\rho}\,2\rho k_w\,2\rho k\left(\frac{\partial^2\xi_0}{\partial\bar{x}^2}+\frac{\partial^2\xi_0}{\partial\bar{y}^2}\right)\\
=\;&-i\rho\left(\frac{\partial^2\xi_0}{\partial\bar{x}^2}+\frac{\partial^2\xi_0}{\partial\bar{y}^2}\right).
\end{aligned} \tag{2.123}$$

Now, the l.h.s. of the wave equation is written as:

$$-i\rho\left(\frac{\partial^2\xi_0}{\partial\bar{x}^2}+\frac{\partial^2\xi_0}{\partial\bar{y}^2}\right)+\frac{\partial\xi_0}{\partial\bar{z}}+2i\rho\frac{\partial^2\xi_0}{\partial\bar{z}\partial\bar{z}_2}. \tag{2.124}$$

To complete the new scaling apply the same x, y scaling to the δ functions on

r.h.s. of the wave equation 2.121

$$\delta(x) = \frac{1}{\sqrt{l_g l_c}}\,\delta(\bar{x}) \quad \delta(y) = \frac{1}{\sqrt{l_g l_c}}\,\delta(\bar{y}) \tag{2.125}$$

By combining equation 2.124, l.h.s., and applying the transverse delta definition in equation 2.125 onto equation 2.121, r.h.s., the final form of the wave equation becomes:

$$\begin{gathered} -i\rho\left(\frac{\partial^2\xi_0}{\partial\bar{x}^2} + \frac{\partial^2\xi_0}{\partial\bar{y}^2}\right) + \frac{\partial\xi_0}{\partial\bar{z}} + 2i\rho\frac{\partial^2\xi_0}{\partial\bar{z}\partial\bar{z}_2} = \frac{e}{\epsilon_0 mc} i\rho\frac{\bar{\beta}_z}{1-\bar{\beta}_z} \\ \frac{1}{l_g l_c}\exp\left\{i\frac{\bar{z}_2}{2\rho}\right\}\frac{\partial}{\partial\bar{z}_2}\sum_{j=1}^{N}\frac{p_{\perp j}}{\beta_{zj}\gamma_j}\delta(\bar{x}-\bar{x}_j)\delta(\bar{y}-\bar{y}_j)\delta(\bar{z}_2-\bar{z}_{2j}) \end{gathered} \tag{2.126}$$

The wave equation is displayed in equation 2.126 before using any analytical or numerical methods to solve this equation. The next section introduces a general numerical Split-Step Fourier method and discusses how this method may be applied to the wave equation.

Split-Step Fourier Method

Equation 2.126 is a mixed partial differential equation so there is no easy analytical method which can solve this equation. A method that could help to solve this equation is to split the problem into two parts and solve them separately. The numerical technique that does this, and is used to solve the equation, is called the Split Step Fourier Method(SSFM).

Consider a generic system,

$$i\nabla_\perp^2 A + \frac{dA}{dz} = J \tag{2.127}$$

A is the unknown and dependent on $\boldsymbol{r}$, z_2 and z. Note that $A(\underline{r}, z_2, z)$ is in normal space and $\widetilde{A}(k_{\underline{r}}, z_2, z)$ in Fourier space.

① First solve the equation

$$i\nabla_\perp^2 A + \frac{dA}{dz} = 0 \tag{2.128}$$

Take Fourier transform of equation 2.128

$$i\nabla_\perp^2 \widetilde{A} + \frac{d\widetilde{A}}{dz} = 0 \tag{2.129}$$

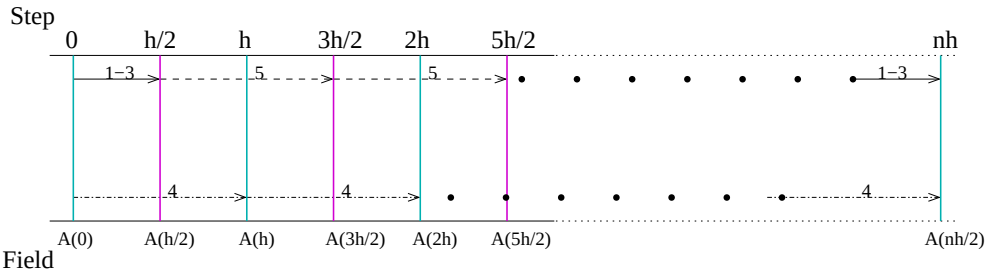

Figure 2.11: The first three steps of the Split-Step Fourier method are solved by firstly transforming the problem in Fourier space, secondly solving the wave equation analytically and thirdly taking the inverse Fourier transform. The solution has advanced $\Delta z = \frac{h}{2}$. The fourth step is to drive the radiation as a full step. The first three steps are repeated for $\Delta z = h$. This is repeated until the end when steps 1-3 are performed.

② Solve the ordinary differential equation (ODE) 2.129 and the solution is

$$\widetilde{A}_{1/2} = \exp\left(-ik_{\perp}^2 h/2\right)\widetilde{A}(k_{\perp}). \tag{2.130}$$

③ Inverse Fourier transform the solution at half step

$$\mathcal{F}^{-1}[\widetilde{A}_{1/2}] \rightarrow A_{1/2}(\underline{r}, z_2, z + h/2)$$

④ Use the solution at half step to solve the second part of the problem

$$\frac{\partial A}{\partial z} = J \tag{2.131}$$

the solution is,

$$A(z + h) = J(z) \cdot h + A_{1/2}(\underline{r}, z_2, z + h/2) \tag{2.132}$$

$$z_{2j}(z + h) = p(z) \cdot h + z_{2j}(z) \tag{2.133}$$

This step is solved simultaneously with the electrons' equation 2.133 and/or other equations.

⑤ Repeat ①–③ steps with a step size of h.

This process repeats step ④–⑤ until the end, see figure 2.11. Towards the end, there is only half a step remaining, therefore one must use step ①–③ to finish the calculation. The example just described is a general format of the SSFM and a modified version of SSFM was applied to the partial differentiate equation (PDE) 2.126.

Split Step as applied

To be consistent with the second part of the SSFM the field envelope will be in redefined as,

$$A = \frac{e\xi_0}{mc\omega_p\sqrt{\gamma_r\rho}}. \tag{2.134}$$

Replacing the new variable A for ξ_0, the final form of the wave equation looks like;

$$-i\rho\left(\frac{\partial^2 A}{\partial\bar{x}^2}+\frac{\partial^2 A}{\partial\bar{y}^2}\right)+\frac{\partial A}{\partial\bar{z}}+2i\rho\frac{\partial^2 A}{\partial\bar{z}\partial\bar{z}_2}=0. \tag{2.135}$$

The coefficient switching from ξ_0 to A will not affect the calculation in the Fourier transform, the same procedures may still be applied.

The following is a step-by-step guide to the first half of the SSFM as applied to equation 2.135.

I. Initially the diffraction acts alone, which means that the radiation field will diffract on the transverse plane. The radiation will propagate freely in the $\bar{z}$ direction without the influence of the source term. Setting the r.h.s. of the wave equation equal to zero, it becomes homogeneous:

$$-i\rho\left(\frac{\partial^2 A}{\partial\bar{x}^2}+\frac{\partial^2 A}{\partial\bar{y}^2}\right)+\frac{\partial A}{\partial\bar{z}}+2i\rho\frac{\partial^2 A}{\partial\bar{z}\partial\bar{z}_2}=0 \tag{2.136}$$

II. To solve this hyperbolic equation, as the name of this method suggests, take a 2-D Fourier transform in the transverse plane;

$$\widetilde{A}(k_{\bar{x}},k_{\bar{y}},\bar{z},\bar{z}_2)=\mathcal{F}[A(\bar{x},\bar{y},\bar{z},\bar{z}_2)] \tag{2.137}$$

$$=\int_{-\infty}^{\infty}\int_{-\infty}^{\infty}A\exp\{-ik_{\bar{x}}\bar{x}-ik_{\bar{y}}\bar{y}\}\mathrm{d}k_{\bar{x}}\mathrm{d}k_{\bar{y}} \tag{2.138}$$

The Fourier transforms of the derivatives are given by:

$$\mathcal{F}\left\{\frac{d^n y}{dx^n}\right\}=(is)^n\bar{y}(s) \tag{2.139}$$

The Fourier variable of $\bar{x}$ and $\bar{y}$ in Fourier space is $-k_\perp^2=-(k_{\bar{x}}^2+k_{\bar{y}}^2)$. With

the second order Fourier derivatives $\bar{x}$ and $\bar{y}$ equation 2.136 yields,

$$i\rho k_{\perp}^{2}\widetilde{A}+\frac{\partial\widetilde{A}}{\partial\bar{z}}+2i\rho\frac{\partial^{2}\widetilde{A}}{\partial\bar{z}\partial\bar{z}_{2}}=0 \tag{2.140}$$

$$\frac{\partial\widetilde{A}}{\partial\bar{z}}+2i\rho\frac{\partial^{2}\widetilde{A}}{\partial\bar{z}\partial\bar{z}_{2}}=-i\rho k_{\perp}^{2}\widetilde{A} \tag{2.141}$$

$$\frac{\partial}{\partial\bar{z}}\left(\widetilde{A}+2i\rho\frac{\partial\widetilde{A}}{\partial\bar{z}_{2}}\right)=-i\rho k_{\perp}^{2}\widetilde{A} \tag{2.142}$$

III. Usually in the SSFM, the Fourier transform is only performed once, but one more Fourier transform is required in this case so the SSFM can be used, so here the method is slightly modified. After taking the first Fourier transform there are still two variables left, $(\bar{z},\bar{z}_2)$, so take the Fourier transform in $\bar{z}_2$ next;

$$\widetilde{A}^{'}=\mathcal{F}[\widetilde{A}]=\int_{-\infty}^{\infty}\widetilde{A}\exp\{-ik_{z_2}z_2\}\mathrm{d}k_{z_2} \tag{2.143}$$

When the Fourier transform is applied on $\bar{z}_2$, equation 2.142 becomes;

$$\frac{\partial}{\partial\bar{z}}(\widetilde{A}^{'}-2\rho k_{z_2}\widetilde{A}^{'}) = -i\rho k_{\perp}^{2}\widetilde{A}^{'} \tag{2.144}$$

$$(1-2\rho k_{z_2})\frac{\partial\widetilde{A}^{'}}{\partial\bar{z}} = -i\rho k_{\perp}^{2}\widetilde{A}^{'} \tag{2.145}$$

Now the equation is an ordinary differential equation (ODE) and it can be solved analytically. The best approach is to integrate with respect to $\bar{z}$ and then take the exponential on both sides of the equation. The solution for this ODE problem becomes:

$$\widetilde{A}^{'}=A_0\exp\left\{-\frac{i\rho k_{\perp}^{2}}{(1-2\rho k_{z_2})}\bar{z}\right\} \tag{2.146}$$

Note that A_0 is an initial field in three dimensional Fourier space.

IV. The final step of the first SSFM is take the inverse Fourier transform of equation 2.146:

$$A\left(\frac{h}{2}\right)=\mathcal{F}_{k_{\perp}^{2}}^{-1}\left(\mathcal{F}_{k_{z_2}}^{-1}\left(\widetilde{A}^{'}\right)\right) \tag{2.147}$$

In the second part of the SSFM, the source term acts alone and the diffraction

terms are neglected. The equation to solve this step is then:

$$\left(\frac{\partial \xi_0}{\partial \bar{z}} + 2i\rho \frac{\partial^2 \xi_0}{\partial \bar{z} \partial \bar{z}_2}\right) \exp\left\{-i\frac{\bar{z}_2}{2\rho}\right\} = \frac{e}{\epsilon_0 mc} i\rho \frac{\bar{\beta}_z}{1-\bar{\beta}_z} \frac{1}{l_g l_c} \frac{\partial}{\partial \bar{z}_2} \sum_{j=1}^{N} \frac{p_{\perp j}}{\beta_{zj}\gamma_j} \delta(\bar{x}-\bar{x}_j)\delta(\bar{y}-\bar{y}_j)\delta(\bar{z}_2-\bar{z}_{2j}) \tag{2.148}$$

Equation 2.148 can now be simplified to an Ordinary Differentiate Equation (ODE), as shown below. One can then apply a 4th order Runge-Kutta (rk4) method to the ODE and solve it along with other electrons' equations, which are also derived from section 2.6.5 onwards.

During the simplification of the equation 2.148, the $\bar{z}_2$ variable is eliminated and resultant ODE is obtained in terms of $\bar{z}$ only.

Let us first define $E = \xi_0 \exp\left\{-i\frac{\bar{z}_2}{2\rho}\right\}$, then l.h.s. of 2.148 becomes,

$$\begin{aligned}
&\frac{\partial}{\partial \bar{z}}\left(\xi_o e^{-i\frac{\bar{z}_2}{2\rho}} + 2i\rho e^{-i\frac{\bar{z}_2}{2\rho}} \frac{\partial \xi_0}{\partial \bar{z}_2}\right) \\
&= \frac{\partial}{\partial \bar{z}}\left(\xi_o e^{-i\frac{\bar{z}_2}{2\rho}} + 2i\rho\left[\frac{\partial}{\partial \bar{z}_2}\xi_0 e^{-i\frac{\bar{z}_2}{2\rho}} + \frac{i}{2\rho}\xi_0 e^{-i\frac{\bar{z}_2}{2\rho}}\right]\right) \\
&= \frac{\partial}{\partial \bar{z}}\left(E + 2i\rho\left[\frac{\partial E}{\partial \bar{z}_2} + \frac{i}{2\rho}E\right]\right) \\
&= \frac{\partial}{\partial \bar{z}}\left(E + 2i\rho\frac{\partial E}{\partial \bar{z}_2} - E\right) \\
&= \frac{\partial}{\partial \bar{z}}\left(2i\rho\frac{\partial E}{\partial \bar{z}_2}\right) \\
&= 2i\rho\frac{\partial^2 E}{\partial \bar{z}\partial \bar{z}_2}.
\end{aligned} \tag{2.149}$$

Equation 2.148 becomes the following when 2.149 is substituted;

$$2i\rho\frac{\partial^2 E}{\partial \bar{z}\partial \bar{z}_2} = \frac{e}{\epsilon_0 mc} i\rho \frac{\bar{\beta}_z}{1-\bar{\beta}_z}\frac{1}{l_g l_c}\frac{\partial}{\partial \bar{z}_2}\sum_{j=1}^{N}\frac{p_{\perp j}}{\beta_{zj}\gamma_j}\delta(\bar{x}-\bar{x}_j)\delta(\bar{y}-\bar{y}_j)\delta(\bar{z}_2-\bar{z}_{2j}). \tag{2.150}$$

The common $\bar{z}_2$ derivative to both sides of the equation may be factored to give:

$$\frac{\partial}{\partial \bar{z}_2}\left[2i\rho\frac{\partial \xi_0}{\partial \bar{z}} - \frac{e}{\epsilon_0 mc} i\rho \frac{\bar{\beta}_z}{1-\bar{\beta}_z}\frac{1}{l_g l_c} \sum_{i=1}^{N}\frac{p_{\perp j}}{\beta_{zj}\gamma_j}\delta(\bar{x}-\bar{x}_j)\delta(\bar{y}-\bar{y}_j)\delta(\bar{z}_2-\bar{z}_{2j})\exp\left\{i\frac{\bar{z}_{2j}}{2\rho}\right\}\right] = 0. \tag{2.151}$$

The general solution of the bracketed term must be a function of $\bar{z}$ plus a constant.

If the source term is set to zero, then the function of $\bar{z}$ in the general function and the constant must be zero because of energy and momentum conservation. Thus the bracketed equation itself must equal zero i.e.:

$$2i\rho\frac{\partial\xi_0}{\partial\bar{z}} = \frac{e}{\epsilon_0 mc} i\rho \frac{\bar{\beta}_z}{1-\bar{\beta}_z}\frac{1}{l_g l_c} \sum_{j=1}^{N}\frac{p_{\perp j}}{\beta_{zj}\gamma_j}\delta(\bar{x}-\bar{x}_j)\delta(\bar{y}-\bar{y}_j)\delta(\bar{z}_2-\bar{z}_{2j})\exp\left\{i\frac{\bar{z}_{2j}}{2\rho}\right\} \tag{2.152}$$

$$\frac{\partial\xi_0}{\partial\bar{z}} = \frac{e}{2\epsilon_0}\frac{1}{l_g l_c}\sum_{j=1}^{N}\frac{\bar{p}_{\perp j}}{\varepsilon\beta_{zj}\gamma_j}\delta(\bar{x}-\bar{x}_j)\delta(\bar{y}-\bar{y}_j)\delta(\bar{z}_2-\bar{z}_{2j})\exp\left\{i\frac{\bar{z}_{2j}}{2\rho}\right\} \tag{2.153}$$

using the definitions

$$\frac{1}{\varepsilon} = \frac{\bar{\beta}_z}{1-\bar{\beta}_z} \tag{2.154}$$

$$\bar{p}_{\perp j} = \frac{p_{\perp j}}{mc}. \tag{2.155}$$

Furthermore, the following term can be re-written as

$$\frac{1}{\varepsilon\beta_{zj}\gamma_j} = \frac{1}{\varepsilon\beta_{zj}}\left(\frac{1-\beta_{zj}^2}{(1+|\bar{p}_\perp|^2)_j}\right)^{1/2} \tag{2.156}$$

$$= \frac{1}{\varepsilon}\left(\frac{1}{(1+|\bar{p}_\perp|^2)_j}\frac{1-\beta_{zj}}{\beta_{zj}}\left(\frac{1-\beta_{zj}}{\beta_{zj}}+2\right)\right)^{1/2} \tag{2.157}$$

$$= \frac{1}{\varepsilon}\left(\frac{\varepsilon Q_j(\varepsilon Q_j+2)}{(1+|\bar{p}_\perp|^2)_j}\right)^{1/2} \tag{2.158}$$

where

$$\frac{1-\beta_{zj}}{\beta_{zj}} = \varepsilon Q_j. \tag{2.159}$$

Substitute the expression 2.158 into the second part of the wave equation 2.153,

$$\frac{\partial\xi_0}{\partial\bar{z}} = \frac{e}{2\epsilon_0}\frac{1}{l_g l_c}\sum_{j=1}^{N}\frac{\bar{p}_{\perp j}}{\varepsilon}\left(\frac{\varepsilon Q_j(\varepsilon Q_j+2)}{(1+|\bar{p}_\perp|^2)_j}\right)^{1/2} \delta(\bar{x}-\bar{x}_j)\delta(\bar{y}-\bar{y}_j)\delta(\bar{z}_2-\bar{z}_{2j})\exp\left\{i\frac{\bar{z}_{2j}}{2\rho}\right\}. \tag{2.160}$$

It is necessary to transform ξ_0 to A just like in the first part of the SSFM and the definition of A in terms of ξ_0 is in equation 2.134.

The coefficient in front of the summation is simplified in the following manner;

$$\begin{aligned}
&\frac{e}{2\varepsilon\epsilon_0}\frac{1}{l_g l_c}\frac{e}{mc\omega_p\sqrt{\gamma_r\rho}} \\
&= \frac{e^2}{2\epsilon_0 mc\varepsilon}\frac{1}{l_g l_c}\frac{a_w}{\gamma_r^2\rho^2 4ck_w} \\
&= \frac{e^2}{2\epsilon_0 mc\varepsilon}\frac{1}{l_g l_c}\frac{a_w}{4ck_w}\gamma_r\rho\left(\frac{4ck_w}{a_w}\right)^2\frac{\epsilon_0 m}{e^2 n_p} \\
&= \frac{2\gamma_r\rho k_w}{\varepsilon a_w n_p}\frac{1}{l_g l_c} \\
&= \frac{2\gamma_r\rho k_w}{\varepsilon a_w}\frac{l_c}{\bar{n}_p} \text{ where } \frac{\bar{n}_p}{l_g l_c^2}=n_p \text{ is the electron density} \\
&= \frac{2\gamma_r\rho k_w}{a_w}\frac{\bar{\beta}_z}{1-\bar{\beta}_z}\frac{1}{2\rho k}\frac{1}{\bar{n}_p} \\
&= \frac{\gamma_r}{a_w}\frac{1}{\bar{n}_p}. \qquad (2.161)
\end{aligned}$$

The coefficient term has changed into 2.161 in such a way that it is only dependent on γ_r, a_w and $\bar{n}_p$ then equation 2.160 is

$$\begin{aligned}
\frac{\partial A}{\partial \bar{z}} = \frac{\gamma_r}{a_w}\frac{1}{\bar{n}_p}\sum_{j=1}^{N}\frac{\bar{p}_{\perp j}}{(1+|\bar{p}_\perp|^2)_j^{1/2}}(\varepsilon Q_j(\varepsilon Q_j+2))^{1/2} \\
\delta(\bar{x}-\bar{x}_j)\delta(\bar{y}-\bar{y}_j)\delta(\bar{z}_2-\bar{z}_{2j})\exp\left\{i\frac{\bar{z}_{2j}}{2\rho}\right\}. \qquad (2.162)
\end{aligned}$$

The transformation of the summation in the wave equation to reduce the sum over real electrons to a sum over macroparticles is now discussed.

In a three-dimensional system there are many electrons within one element. The volume of an element has the size $V_e = d\bar{x}d\bar{y}d\bar{z}_2$ and they could be represented by a few macroparticles. The j^{th} index in the summation is denoted as the index of each electron. For example if there are 8 macroparticles in the element, and assuming the volume of each of the macroparticles occupies the same smaller volume, see figure 2.12. The volume occupied by each macroparticle is,

$$V_k = \delta\bar{x}\delta\bar{y}\delta\bar{z}_2 \qquad (2.163)$$

It is not effective to model the system with the many real electrons because the computational time would be prohibitive. Therefore, macroparticles were used to replace the real electrons and the summation on the wave equation was carried out over the macroparticles. Thus the real electron summation has been divided

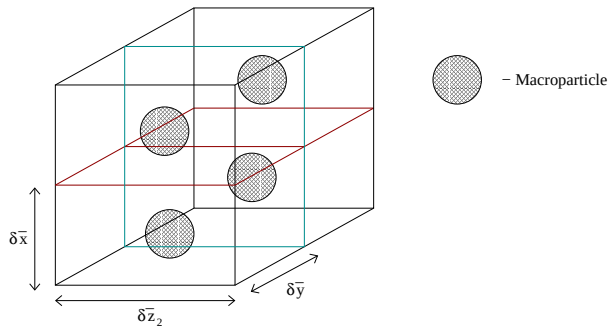

Figure 2.12: Inside the element in the diagram there are four macroparticles each occupying a volume of $V_k = \delta\bar{x}\delta\bar{y}\delta\bar{z}_2$.

into two separate summations;

$$\frac{1}{\bar{n}_p}\sum_{j=1}^{N}(\cdots)_j = \frac{1}{\bar{n}_p}\sum_{k=1}^{N_m}\sum_{i=1}^{N_k}(\cdots)_i \tag{2.164}$$

On the l.h.s. of equation 2.164, it is summed over the real electrons from $j = 1$ to N whereas the first summation on the r.h.s. is to sum over all macroparticles from $k = 1$ to N_m, and by the sum over all the electrons from $i = 1$ to N_k where N_k is the number of electrons the k^{th} macroparticles represents. In any macroparticles it is true that all the electrons in a macroparticle would have the same $\bar{p}_{\perp j}$'s and Q_j's values so

$$(\cdots)_i = (\cdots)_k \;\forall\; i. \tag{2.165}$$

The summation in equation 2.164 is then equal to

$$\frac{1}{\bar{n}_p}\sum_{j=1}^{N}(\cdots)_j = \frac{1}{\bar{n}_p}\sum_{k=1}^{N_m}N_k(\cdots)_k \tag{2.166}$$

where N_k is the charge weight of the k^{th} macroparticle in units of the electron charge and it is defined as $N_k = \chi_k \bar{n}_p V_k$ which can be substitute to give

$$\frac{1}{\bar{n}_p}\sum_{j=1}^{N}(\cdots)_j = \frac{1}{\cancel{\bar{n}_p}}\sum_{k=1}^{N_m}\chi_k\cancel{\bar{n}_p}V_k(\cdots)_k \tag{2.167}$$

$$= \sum_{k=1}^{N_p}\chi_k V_k(\cdots)_k \tag{2.168}$$

and where $0 < \chi_k \leq 1$ is a weighting function of the k^{th} macroparticle. After the change of summation, the final form of the wave equation in the second part

reads as,

$$\frac{\partial A}{\partial \bar{z}} = \frac{\gamma_r}{a_w} \sum_{k=1}^{N_m} \chi_k V_k \frac{\bar{p}_{\perp k}}{(1+|\bar{p}_\perp|^2)_k^{\frac{1}{2}}} (\varepsilon Q_k(\varepsilon Q_k + 2))^{\frac{1}{2}} \\ \delta(\bar{x} - \bar{x}_k)\delta(\bar{y} - \bar{y}_k)\delta(\bar{z}_2 - \bar{z}_{2k}) \exp\left\{ i \frac{\bar{z}_{2k}}{2\rho} \right\}. \tag{2.169}$$

The SSFM has been applied to the wave equation; the first part of SSFM was solved by using FFT and the final form of the equation for the second part has been derived in equation 2.169. In the next section the numerical method used to solve this equation is discussed - the reduced wave equation will be solved along with the electron equations by using rk4.

2.6.4 Finite Element Method on the wave equation

The Finite Element Method (FEM) used to solve the wave equation 2.169 is called the Galerkin method [29] and the first step is to discretise the unknown quantity, A. The field is discretised into a linear interpolation function and nodal value a_m, a new unknown,

$$A(\bar{x}, \bar{y}, \bar{z}, \bar{z}_2) = \sum_m a_m(\bar{z}) \Lambda_m(\bar{x}, \bar{y}, \bar{z}_2) \tag{2.170}$$

where m is the element index of the 3D system and Λ_m is a group of interpolation functions within an 8-node hexahedral element, defined as,

$$\Lambda_m(\bar{x}, \bar{y}, \bar{z}_2) = \left(\sum_{i=1}^{8} L_i \right)_m \tag{2.171}$$

where i is the local index within an element and L_i is the interpolation function at each node, which is listed in Table 2.1.

The eight local nodes are labelled as shown in figure 2.13 and Δx,Δy, Δz_2 are the sizes of an element and vary depending on the dimensions of the system.

Continuing with the calculation of the wave equation , the definition in equation 2.170 may be substituted and wave equation is now read as:

$$\frac{\partial A}{\partial \bar{z}} = \sum_m \left(\Lambda_m \frac{\partial a_m(\bar{z})}{\partial \bar{z}} = \frac{\gamma_r}{a_w} \sum_{k=1}^{N_m} \chi_k V_k \frac{\bar{p}_{\perp k}}{(1+|\bar{p}_\perp|^2)_k^{\frac{1}{2}}} \right. \\ \left. (\varepsilon Q_k(\varepsilon Q_k + 2))^{\frac{1}{2}} \delta^3(\bar{x}_k, \bar{y}_k, \bar{z}_{2k}) \exp\left\{ i \frac{\bar{z}_{2k}}{2\rho} \right\} \right). \tag{2.172}$$

Node	Interpolation functions
L_1	$\left(1-\frac{\bar{x}}{\Delta\bar{x}}\right)\left(1-\frac{\bar{y}}{\Delta\bar{y}}\right)\left(1-\frac{\bar{z}_2}{\Delta\bar{z}_2}\right)$
L_2	$\left(1-\frac{\bar{x}}{\Delta\bar{x}}\right)\left(\frac{\bar{y}}{\Delta\bar{y}}\right)\left(1-\frac{\bar{z}_2}{\Delta\bar{z}_2}\right)$
L_3	$\left(\frac{\bar{x}}{\Delta\bar{x}}\right)\left(1-\frac{\bar{y}}{\Delta\bar{y}}\right)\left(1-\frac{\bar{z}_2}{\Delta\bar{z}_2}\right)$
L_4	$\left(\frac{\bar{x}}{\Delta\bar{x}}\right)\left(\frac{\bar{y}}{\Delta\bar{y}}\right)\left(1-\frac{\bar{z}_2}{\Delta\bar{z}_2}\right)$
L_5	$\left(1-\frac{\bar{x}}{\Delta\bar{x}}\right)\left(1-\frac{\bar{y}}{\Delta\bar{y}}\right)\left(\frac{\bar{z}_2}{\Delta\bar{z}_2}\right)$
L_6	$\left(1-\frac{\bar{x}}{\Delta\bar{x}}\right)\left(\frac{\bar{y}}{\Delta\bar{y}}\right)\left(\frac{\bar{z}_2}{\Delta\bar{z}_2}\right)$
L_7	$\left(\frac{\bar{x}}{\Delta\bar{x}}\right)\left(1-\frac{\bar{y}}{\Delta\bar{y}}\right)\left(\frac{\bar{z}_2}{\Delta\bar{z}_2}\right)$
L_8	$\left(\frac{\bar{x}}{\Delta\bar{x}}\right)\left(\frac{\bar{y}}{\Delta\bar{y}}\right)\left(\frac{\bar{z}_2}{\Delta\bar{z}_2}\right)$

Table 2.1: Table of linear interpolation function on each of the eight nodes in a hexahedral element.

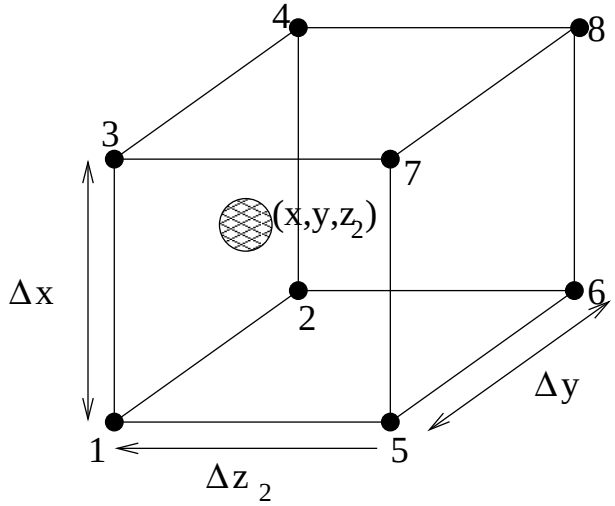

Figure 2.13: A macroparticle position, ($\bar{x}$,$\bar{y}$,$\bar{z}_2$), inside a hexahedral element ($\Delta\bar{x}$,$\Delta\bar{y}$,$\Delta\bar{z}_2$) with 8 nodes. Each node is labelled with a local node number.

The procedure of the Galerkin method applied to the wave equation 2.172 is as follows: first multiply the interpolation function on both sides of the equation 2.172 and then integrate it over all space. Equation 2.172 can be rewritten as a matrix equation, by defining $\{\ \} \equiv$ a column vector, $\lfloor\ \rfloor \equiv$ a row vector as in [30], and the system can be rewritten as:

$$\begin{aligned}\int \{\Lambda_m\}\lfloor\Lambda_m\rfloor \frac{\partial a_m(\bar{z})}{\partial \bar{z}} dV = \frac{\gamma_r}{a_w}\sum_{k=1}^{N_m}\int \{\Lambda_m\}\chi_k V_k \frac{\bar{p}_{\perp k}}{(1+|\bar{p}_{\perp k}|^2)^{1/2}} \\ (\varepsilon Q_k(\varepsilon Q_k+2))^{1/2}\delta^3(\bar{x}_k,\bar{y}_k,\bar{z}_{2k})\exp\left\{i\frac{\bar{z}_2}{2\rho}\right\}dV \quad \forall\ m.\end{aligned} \tag{2.173}$$

The integral of the two interpolation functions on the l.h.s. generates the "Stiffness Matrix", $K = \{\Lambda_m\}\lfloor\Lambda_m\rfloor$ [29], to give.

$$[K]\frac{\partial a_m(\bar{z})}{\partial \bar{z}} = \frac{\gamma_r}{a_w}\sum_{k=1}^{N_m}\bar{\chi}_k\frac{\bar{p}_{\perp k}}{(1+|\bar{p}_\perp|^2)^{1/2}}(\varepsilon Q_k(\varepsilon Q_k+2))^{1/2}\left(\Lambda_m\right)_k\exp\left\{i\frac{\bar{z}_{2k}}{2\rho}\right\} \quad \forall\ m \tag{2.174}$$

here $\bar{\chi}_k = \chi_k V_k$ where V_k is defined in equation 2.163 and $\left(\Lambda_m\right)_k$ is the interpolation function of the corresponding evaluated element for k^{th} macroparticle. Note that $\Lambda_m \equiv 0$ outwith the elements to which it belongs. The Stiffness Matrix can be calculated analytically since the interpolation functions are known and defined in table 2.1. For each element there are eight local nodes so the size of an elemental K is 8×8 and it was calculated as follows:

$$[K]_{element} = \int_V \begin{bmatrix} L_1L_1 & L_1L_2 & \cdots\cdots & L_1L_8 \\ L_2L_1 & L_2L_2 & \cdots\cdots & L_1L_8 \\ \vdots & \vdots & \vdots & \vdots \\ \vdots & \vdots & \vdots & \vdots \\ \vdots & \vdots & \vdots & \vdots \\ L_8L_1 & L_8L_2 & \cdots\cdots & L_8L_8 \end{bmatrix} dV. \tag{2.175}$$

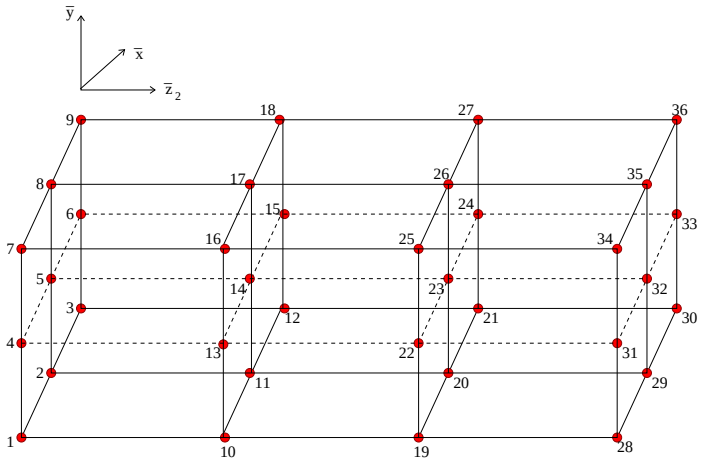

Figure 2.14: In a $2 \times 2 \times 3$ system, with 12 elements. The order of the global nodes is: along $\bar{x}$ first then $\bar{y}$ and then $\bar{z}_2$. The global nodes are labelled as shown.

After the integration for each entry, the resultant $[K]_{element}$ is:

$$[K]_{element} = \frac{\Delta x \Delta y \Delta z_2}{216} \begin{bmatrix} 8 & 4 & 4 & 2 & 4 & 2 & 2 & 1 \\ 4 & 8 & 2 & 4 & 2 & 4 & 1 & 2 \\ 4 & 2 & 8 & 4 & 2 & 1 & 4 & 2 \\ 2 & 4 & 4 & 8 & 1 & 2 & 2 & 4 \\ 4 & 2 & 2 & 1 & 8 & 4 & 4 & 2 \\ 2 & 4 & 1 & 2 & 4 & 8 & 2 & 4 \\ 2 & 1 & 4 & 2 & 4 & 2 & 8 & 4 \\ 1 & 2 & 2 & 4 & 2 & 4 & 4 & 8 \end{bmatrix}. \tag{2.176}$$

This is an elemental Stiffness Matrix, $[K]_{element}$. To construct a full Stiffness matrix, $[K]$, $[K]_{element}$ are added for each element in the complete structure.

Each node within an element has an associated global node number. Consider the size of a system is $2 \times 2 \times 3$, the figure in 2.14 shows how the global nodes are numbered. Element 1 has global node 1, 2, 4, 5, 10, 11, 13 and 14 which are the local nodes from 1-8 respectively. The local $[K]_{element}$ values for element 1 are entered into the corresponding global matrix K. When duplicate node entries exist in the global K, then they are summed together. Since the velocity of electrons never exceed the speed of light, then there should be no electrons that can propagate into region $\bar{z}_2 < 0$. Therefore, a boundary condition may be applied to the entries associated with the nodes at $\bar{z}_2 = 0$, i.e. global nodes 1-9. Also, K is a singular matrix because its determinant is equal to zero. To remove this singularity problem one must invoke the boundary conditions [30].

The element size, $V_e = \Delta x \Delta y \Delta z_2$, in the stiffness matrix in equation 2.176

is the same across the system. Since V_e is a constant value one can factor it on both sides of the equation,

$$\frac{1}{216}[\cdot\,\cdot\,\cdot]\frac{\partial a_m(\bar{z})}{\partial \bar{z}} = \frac{\gamma_r}{a_w}\sum_{k=1}^{N_m}\frac{\bar{\chi}_k}{V_e}\frac{\bar{p}_{\perp k}}{(1+|\bar{p}_\perp|^2)^{1/2}}(\varepsilon Q_k(\varepsilon Q_k+2))^{1/2}\left(\Lambda_m\right)_k \exp\left\{i\frac{\bar{z}_{2k}}{2\rho}\right\}. \tag{2.177}$$

The last step is to use a NAG linear solver to invert the stiffness matrix and reduce to the canonical form of $\underline{A}x = \underline{b}$, where $\underline{A}$ are the $\bar{z}$ derivatives and $\underline{b}$ is the source term. This is then solved by rk4 along with the remaining electron equations which are derived in the section 2.6.5–2.6.7. Note that at this stage it would be possible to introduce elements of unequal volume.

2.6.5 Electron equation on the transverse plane

The first derivation of the electron equations is in the transverse plane that start with the Lorentz Force equation 2.5. By definition, force can be defined as the time derivative of momentum, so the Lorentz equation may be described in terms of momentum while the time derivative may be transformed to the dimensionless $\bar{z}$ variable as follows:

$$\boldsymbol{F} = \frac{d\boldsymbol{p}_j}{dt} \tag{2.178}$$

$$= c\beta_{zj}\frac{d\boldsymbol{p}_j}{dz} \tag{2.179}$$

$$= c\beta_{zj}2k_w\rho\frac{d\boldsymbol{p}_j}{d\bar{z}} \tag{2.180}$$

$$\implies \frac{d\boldsymbol{p}_j}{d\bar{z}} = -\frac{e}{2k_w\rho c\beta_{zj}}(\boldsymbol{E}+\frac{\boldsymbol{p}_j}{\gamma_j m}\times\boldsymbol{B}). \tag{2.181}$$

Next, multiplying by $\hat{\boldsymbol{e}}^*$ across equation 2.181:

$$LHS \text{ of } 2.181 = \frac{d\boldsymbol{p}_j}{d\bar{z}}\cdot\hat{\boldsymbol{e}}^* = \frac{1}{\sqrt{2}}\frac{dp_{\perp j}}{d\bar{z}} \tag{2.182}$$

$$RHS \text{ of } 2.181 = -\frac{e}{2k_w\rho c\beta_{zj}}(\boldsymbol{E}+\frac{\boldsymbol{p}_j}{\gamma_j m}\times\boldsymbol{B})\cdot\hat{\boldsymbol{e}}^* \tag{2.183}$$

First, $\boldsymbol{p}_j \times \boldsymbol{B}$ is calculated where the magnetic field is the sum of the undulator magnetic field and the magnetic field of the radiation:

$$\boldsymbol{E} = \frac{1}{\sqrt{2}}(\hat{\boldsymbol{e}}\xi_0 \exp\{i(kz - \omega t)\} + c.c.) \tag{2.184}$$

$$\boldsymbol{B} = \frac{B_w}{\sqrt{2}}(\hat{\boldsymbol{e}} \exp\{-ik_w z\} + c.c.) - \frac{i}{\sqrt{2}}\left(\frac{\xi_0}{c}\hat{\boldsymbol{e}} \exp\{i(kz - \omega t)\} - c.c.\right). \tag{2.185}$$

The x-component of the cross product is

$$(\boldsymbol{p}_j \times \boldsymbol{B})_x = -p_{zj}B_y = -p_{zj}\Bigg(-\frac{iB_w}{2}(\exp\{ik_w z\} - c.c) + \frac{1}{2}(\frac{\xi_0}{c}\exp\{i(kz - \omega t)\} + c.c)\Bigg) \tag{2.186}$$

and y-component is

$$(\boldsymbol{p}_j \times \boldsymbol{B})_y = p_{zj}B_x = p_{zj}\Bigg(\frac{B_w}{2}(\exp\{-ik_w z\} + c.c) - \frac{i}{2}(\frac{\xi_0}{c}\exp\{i(kz - \omega t)\} - c.c)\Bigg). \tag{2.187}$$

By substituting equations 2.186 and 2.187 the r.h.s. of equation 2.183 written in full is

$$\begin{aligned}
&= -\frac{e}{2k_w\rho c\beta_{zj}}\Bigg(\frac{\xi_0}{\sqrt{2}}\exp\{i(kz - \omega t)\} + \frac{p_{zj}}{\sqrt{2}\gamma_j m}\Bigg[\frac{iB_w}{2}\left(\cancel{\exp\{ik_w z\}} - \exp\{-ik_w z\}\right) \\
&- \frac{1}{2}\left\{\frac{\xi_0}{c}\exp\{i(kz - \omega t)\} + \cancel{\frac{\xi_0^*}{c}\exp\{-i(kz - \omega t)\}}\right\} - \frac{iB_w}{2}\left(\cancel{\exp\{ik_w z\}} + \exp\{-ik_w z\}\right) \\
&- \frac{1}{2}\left\{\frac{\xi_0}{c}\exp\{i(kz - \omega t)\} - \cancel{\frac{\xi_0^*}{c}\exp\{-i(kz - \omega t)\}}\right\}\Bigg]\Bigg)
\end{aligned} \tag{2.188}$$

$$\begin{aligned}
&= -\frac{e}{2k_w\rho c\beta_{zj}}\Bigg(\frac{\xi_0}{\sqrt{2}}\exp\{i(kz - \omega t)\} + \frac{p_{zj}}{\sqrt{2}\gamma_j m}\Bigg[-iB_w \exp\{-ik_w z\} \\
&\qquad - \frac{\xi_0}{c}\exp\{i(kz - \omega t)\}\Bigg]\Bigg).
\end{aligned} \tag{2.189}$$

Subsequently, calculation of equations 2.182 and 2.189 are brought together and the additional scaling for $p_{\perp j}$, ξ_0, εQ_j and B_w are incorporated as follows

$$\begin{aligned}
\frac{1}{\sqrt{2}}\frac{dp_{\perp j}}{d\bar{z}} &= -\frac{e}{2k_w\rho c\beta_{zj}}\left(\frac{\xi_0}{\sqrt{2}}\exp\{i(kz-\omega t)\}+\frac{p_{zj}}{\sqrt{2}\gamma_j m}\left[-iB_w\exp\{-ik_w z\}\right.\right.\\
&\qquad\left.\left.-\frac{\xi_0}{c}\exp\{i(kz-\omega t)\}\right]\right)\\
\frac{dp_{\perp j}}{d\bar{z}} &= -\frac{e}{2k_w\rho c\beta_{zj}}\left(\xi_0\exp\{i(kz-\omega t)\}+\frac{p_{zj}}{\gamma_j m}\left[-iB_w\exp\{-ik_w z\}\right.\right.\\
&\qquad\left.\left.-\frac{\xi_0}{c}\exp\{i(kz-\omega t)\}\right]\right) \text{ where } {}_{p_{zj}=\gamma_j mc\beta zj}\\
&= -\frac{e}{2ck_w\rho}\left[\frac{\xi_0}{\beta_{zj}}\exp\{i(kz-\omega t)\}-icB_w\exp\{-ik_w z\}-\xi_0\exp\{i(kz-\omega t)\}\right]\\
&= \frac{e}{2k_w\rho}\left[iB_w\exp\{-ik_w z\}-\frac{1-\beta_{zj}}{\beta_{zj}}\frac{\xi_0}{c}\exp\{i(kz-\omega t)\}\right]\\
&= \frac{e}{2k_w\rho mc}\left[iB_w\exp\{-ik_w z\}-\frac{1-\beta_{zj}}{\beta_{zj}}\frac{\xi_0}{c}\exp\{i(kz-\omega t)\}\right] \text{ where } {}_{\bar{p}_\perp=\frac{p_\perp}{mc}}\\
&= \frac{e}{2k_w\rho mc}\left[ia_w\frac{mck_w}{e}\exp\{-ik_w z\}-\varepsilon Q_j\frac{\xi_0}{c}\exp\{i(kz-\omega t)\}\right] \text{ where } {}_{a_w=\frac{eB_w}{mck_w}}\\
&= \frac{1}{2\rho}\left[ia_w\exp\left\{-\frac{i\bar{z}}{2\rho}\right\}-\frac{e}{k_w mc^2}\varepsilon Q_j\xi_0\exp\left\{-\frac{i\bar{z}_{2j}}{2\rho}\right\}\right] \text{ where } {}_{\frac{e\xi_0}{mc^2k_w}=\frac{1}{\cancel{k_w}c}A\frac{\gamma_r^2\rho^2 4c\cancel{k_w}}{a_w}}\\
\Rightarrow \frac{dp_{\perp j}}{d\bar{z}} &= \frac{a_w}{2\rho}\left[i\exp\left\{-\frac{i\bar{z}}{2\rho}\right\}-\left(\frac{2\gamma_r\rho}{a_w}\right)^2\varepsilon Q_j A\exp\left\{-\frac{i\bar{z}_{2j}}{2\rho}\right\}\right]. \qquad (2.190)
\end{aligned}$$

This equation describes the transverse momentum of the particle. The second electron equation describing axial motion is derived from the z-component of the Lorentz equation and is given in the next section.

2.6.6 Electron equation in the longitudinal direction

According to the definition in equation 2.38 in section 2.3.2, since the radiation field varies in the x and y direction as well as propagating forward in the z-direction, there is no z-component in the electric field. This means the Lorentz force equation to be used only has a contribution from the magnetic field. The calculation of the second electron equation begins with the scaled Lorentz equation 2.181:

$$\frac{d\boldsymbol{p}_j}{d\bar{z}} = -\frac{e}{2k_w\rho c\beta_{zj}}\left(\frac{\boldsymbol{p}_j}{\gamma_j m}\times\boldsymbol{B}\right). \qquad (2.191)$$

The z-component of $\boldsymbol{p}_j \times \boldsymbol{B}$ is computed and, using the definitions of equation 2.102 for p_x and p_y, equation 2.185 for B_x and B_y;

$$(\boldsymbol{p}_j \times \boldsymbol{B})_z = p_x B_y - p_y B_x \tag{2.192}$$

$$= \frac{1}{2}(p_\perp + p_\perp^*)\left[-\frac{iB_w}{2}(\exp\{ik_w z\} - c.c.) + \frac{1}{2}\left(\frac{\xi_0}{2}\exp\{i(kz-\omega t)\} + c.c.\right)\right] - \frac{i}{2}(p_\perp - p_\perp^*)\left[\frac{B_w}{2}(\exp\{ik_w z + c.c.\}) - \frac{i}{2}\left(\frac{\xi_0}{2}\exp\{i(kz-\omega t)\} - c.c.\right)\right] \tag{2.193}$$

$$= \frac{p_\perp}{2}\left(\frac{\xi_0^*}{c}\exp\{-i(kz-\omega t)\} - iB_w \exp\{ik_w z\}\right) + c.c. \tag{2.194}$$

Adding the derived expression 2.194 in equation 2.191, the z-component is,

$$\frac{dp_{zj}}{d\bar{z}} = -\frac{e}{2k_w \rho c \beta_{zj}}\left[\frac{p_\perp}{2\gamma_j m}\left(\frac{\xi_0^*}{c}\exp\{-i(kz-\omega t)\} - iB_w\exp\{ik_w z\}\right) + c.c.\right]. \tag{2.195}$$

The derivatives on the l.h.s. of 2.195 can be further expanded in this way shown below,

$$\frac{dp_{zj}}{d\bar{z}} = \frac{d}{d\bar{z}}(\gamma_j mc\beta_{zj}) \tag{2.196}$$

$$= mc\left(\gamma_j \frac{d\beta_{zj}}{d\bar{z}} + \beta_{zj}\frac{d\gamma_j}{d\bar{z}}\right) \tag{2.197}$$

$$\text{where } \frac{d\gamma_j}{dt} = -\frac{e}{mc}\boldsymbol{\beta}_j \cdot \boldsymbol{E} \tag{2.198}$$

$$\frac{d\gamma_j}{d\bar{z}} = -\frac{e}{2k_w c^2 m\rho\beta_{zj}}\boldsymbol{\beta}_j \cdot \boldsymbol{E}. \tag{2.199}$$

The term $\boldsymbol{\beta}_j \cdot \boldsymbol{E}$ is expressed in terms of momentum and electric field:

$$\boldsymbol{\beta}_j \cdot \boldsymbol{E} = \frac{\boldsymbol{p}_j}{\gamma_j mc}\cdot \boldsymbol{E} \tag{2.200}$$

$$= \frac{1}{\gamma_j mc}(p_{xj}E_x + p_{yj}E_y) \tag{2.201}$$

$$= \frac{1}{\gamma_j mc}\left[\frac{1}{2}(p_\perp + p_\perp^*)\frac{1}{2}\left(\xi_0\exp\{i(kz-\omega t)\} + \frac{\xi_0^*}{c}\exp\{-i(kz-\omega t)\}\right) + \frac{i}{2}(p_\perp - p_\perp^*)\frac{i}{2}\left(\xi_0\exp\{i(kz-\omega t)\} - \frac{\xi_0^*}{c}\exp\{-i(kz-\omega t)\}\right)\right] \tag{2.202}$$

$$= \frac{1}{2\gamma_j mc}\left[p_{\perp j}\xi_0^*\exp\{-i(kz-\omega t)\} + p_{\perp j}^*\xi_0\exp\{i(kz-\omega t)\}\right]. \tag{2.203}$$

Gathering equations 2.195 and 2.203, the second electron equation becomes:

$$\gamma_j \frac{d\beta_{zj}}{d\bar{z}} - \frac{e}{2k_w c^2 m\rho}\boldsymbol{\beta}_j \cdot \boldsymbol{E} = -\frac{e}{2k_w \rho m c^2 \beta_{zj}} \left[\frac{p_{\perp j}}{2\gamma_j m}\left(\frac{\xi_0^*}{c}\exp\{-i(kz-\omega t)\} - iB_w \exp\{ik_w z\}\right) + c.c.\right]. \tag{2.204}$$

Substituting for equation 2.203 into equation 2.204 yields:

$$\gamma_j \frac{d\beta_{zj}}{d\bar{z}} - \frac{e}{2k_w c^2 m\rho}\left[\frac{p_{\perp j}}{2\gamma_j mc}\xi_0^* \exp\{-i(kz-\omega t)\} + \frac{p_{\perp j}^*}{2\gamma_j mc}\xi_0 \exp\{i(kz-\omega t)\}\right] = -\frac{e}{2k_w \rho m c^2 \beta_{zj}}\left[\frac{p_{\perp j}}{2\gamma_j mc}\xi_0^* \exp\{-i(kz-\omega t)\} + \frac{p_{\perp j}^*}{2\gamma_j mc}\xi_0 \exp\{i(kz-\omega t)\} - \frac{ip_{\perp j}}{2\gamma_j m}B_w \exp\{ik_w z\} + \frac{ip_{\perp j}^*}{2\gamma_j m}B_w \exp\{-ik_w z\}\right] \tag{2.205}$$

$$\gamma_j \frac{d\beta_{zj}}{d\bar{z}} = \frac{e}{2mc^2 k_w \rho}\left[\left(1-\frac{1}{\beta_{zj}}\right)\left(\frac{p_{\perp j}^*}{2\gamma_j mc}\xi_0 \exp\{i(kz-\omega t)\} + c.c.\right) - \frac{i}{2\gamma_j m\beta_{zj}}(p_{\perp j}^* B_w \exp\{-ik_w z\} - c.c.)\right] \tag{2.206}$$

$$\frac{d\beta_{zj}}{d\bar{z}} = \frac{e}{4m^2 c^3 k_w \rho \gamma_j^2}\left[\left(1-\frac{1}{\beta_{zj}}\right)(p_{\perp j}^* \xi_0 \exp\{i(kz-\omega t)\} + c.c.) - \frac{ic}{\beta_{zj}}(p_{\perp j}^* B_w \exp\{-ik_w z\} - c.c.)\right] \tag{2.207}$$

$$\frac{d\beta_{zj}}{d\bar{z}} = -\frac{e}{4m^2 c^3 k_w \rho \gamma_j^2}\left[\left(\frac{1-\beta_{zj}}{\beta_{zj}}\right)(p_{\perp j}^* \xi_0 \exp\{i(kz-\omega t)\} + c.c.) + \frac{ic}{\beta_{zj}}B_w(p_{\perp j}^* \exp\{-ik_w z\} - c.c.)\right]. \tag{2.208}$$

Using the definition of the relativistic factor,

$$\gamma_j^{-2} = 1 - \beta_{zj}^2 - \beta_{xj}^2 - \beta_{yj}^2 \tag{2.209}$$

$$= 1 - \beta_{zj}^2 - \frac{1}{\gamma_j^2 m^2 c^2}(p_{xj}^2 + p_{yj}^2) \text{ with } \boldsymbol{\beta}_j = \frac{\boldsymbol{p}_j}{\gamma_j mc} \tag{2.210}$$

$$\gamma_j^{-2}\left(1 + \frac{p_\perp p_\perp^*}{m^2c^2}\right) = 1 - \beta_{zj}^2 \tag{2.211}$$

$$\gamma_j^{-2}\left(1 + \bar{p}_\perp \bar{p}_\perp^*\right) = 1 - \beta_{zj}^2 \tag{2.212}$$

$$\gamma_j^{-2} = \frac{1 - \beta_{zj}^2}{1 + |\bar{p}_\perp|_j^2} \tag{2.213}$$

and equation 2.159 provides the definition of εQ_j, so the derivative of equation 2.208 has changed to Q and it evolved as

$$\frac{dQ_j}{d\bar{z}} = -\frac{1}{\varepsilon\beta_{zj}^2}\frac{d\beta_{zj}}{d\bar{z}} \tag{2.214}$$

$$\frac{dQ_j}{d\bar{z}} = \frac{1}{\varepsilon\beta_{zj}^2}\frac{e}{4m^2c^3k_w\rho}\frac{1}{\gamma_j^2} \left[\varepsilon Q_j\left(p_{\perp j}^*\xi_0 \exp\left\{-i\frac{\bar{z}_{2j}}{2\rho}\right\} + c.c.\right) + \frac{ic}{\beta_{zj}}B_w\left(p_{\perp j}^* \exp\left\{-i\frac{\bar{z}}{2\rho}\right\} - c.c.\right)\right] \tag{2.215}$$

$$\frac{dQ_j}{d\bar{z}} = \frac{1}{\varepsilon\beta_{zj}^2}\frac{1 - \beta_{zj}^2}{1 + |\bar{p}_\perp|_j^2}\frac{e\ mc}{4m^2c^3k_w\rho} \left[\varepsilon Q_j\left(\bar{p}_{\perp j}^*\xi_0 \exp\left\{-i\frac{\bar{z}_{2j}}{2\rho}\right\} + c.c.\right) + \frac{ic}{\beta_{zj}}B_w\left(\bar{p}_{\perp j}^* \exp\left\{-i\frac{\bar{z}}{2\rho}\right\} - c.c.\right)\right] \tag{2.216}$$

$$\text{where } \frac{1 - \beta_{zj}^2}{\beta_{zj}^2} = \frac{1 - \beta_{zj}}{\beta_{zj}}\frac{1 + \beta_{zj}}{\beta_{zj}}$$

$$= \frac{1 - \beta_{zj}}{\beta_{zj}}\left(\frac{1 - \beta_{zj}}{\beta_{zj}} + 2\right)$$

$$= \varepsilon Q_j(\varepsilon Q_j + 2) \text{ has been used.}$$

$$\Rightarrow \frac{dQ_j}{d\bar{z}} = \frac{e}{4mc^2k_w\rho}\frac{Q_j(\varepsilon Q_j+2)}{1+|\bar{p}_\perp|_j^2}\left[\varepsilon Q_j\left(\bar{p}^*_{\perp j}\xi_0\exp\left\{-i\frac{\bar{z}_{2j}}{2\rho}\right\}+c.c.\right)+\right.$$
$$\left.\frac{ic}{\beta_{zj}}B_w(\bar{p}^*_{\perp j}\exp\left\{-i\frac{\bar{z}}{2\rho}\right\}-c.c.)\right] \quad (2.217)$$
$$= \frac{1}{4\rho}\frac{Q_j(\varepsilon Q_j+2)}{1+|\bar{p}_\perp|_j^2}\left[\varepsilon Q_j\left(\bar{p}^*_{\perp j}\frac{e\xi_0}{mck_w}\exp\left\{-i\frac{\bar{z}_{2j}}{2\rho}\right\}+c.c.\right)\right.$$
$$\left.+ia_w(\varepsilon Q_j+1)\left(\bar{p}^*_{\perp j}\exp\left\{-i\frac{\bar{z}}{2\rho}\right\}-c.c.\right)\right] \quad (2.218)$$
$$= \frac{1}{4\rho}\frac{Q_j(\varepsilon Q_j+2)}{1+|\bar{p}_\perp|_j^2}\left[\varepsilon Q_j\left(\bar{p}^*_{\perp j}\frac{4\gamma_r^2\rho^2A}{a_w}\exp\left\{-i\frac{\bar{z}_{2j}}{2\rho}\right\}+c.c.\right)\right.$$
$$\left.+ia_w(\varepsilon Q_j+1)\left(\bar{p}^*_{\perp j}\exp\left\{-i\frac{\bar{z}}{2\rho}\right\}-c.c.\right)\right] \quad (2.219)$$
$$\frac{dQ_j}{d\bar{z}} = \frac{a_w}{4\rho}\frac{Q_j(\varepsilon Q_j+2)}{1+|\bar{p}_\perp|_j^2}\left[i(\varepsilon Q_j+1)\left(\bar{p}^*_{\perp j}\exp\left\{-i\frac{\bar{z}}{2\rho}\right\}-c.c.\right)\right.$$
$$\left.+\left(\frac{2\gamma_r\rho}{a_w}\right)^2\varepsilon Q_j\left(\bar{p}^*_{\perp j}A\exp\left\{-i\frac{\bar{z}_{2j}}{2\rho}\right\}+c.c.\right)\right] \quad (2.220)$$

Notice that the two equations, 2.190 and 2.220, for the three-dimensional system are identical to the one-dimensional case. However, no focussing in the transverse plane has been included in the electron equations yet but this is derived in the section 2.6.10.

The final three equations to be derived in the next section are the equations describing the electrons' axial positions and their initial conditions.

2.6.7 Equations for electrons' axial positions

The first equation that is derived is in the axial position $\bar{z}_{2j}$ which is calculated from the definition of $\bar{z}_{2j}$ using equation (2.50) and (2.90),

$$\frac{d\bar{z}_{2j}}{dz} = 2k_w\rho\frac{\bar{\beta}_z}{1-\bar{\beta}_z}\left(c\frac{dt_j}{dz}-1\right) \quad (2.221)$$
$$\frac{d\bar{z}_{2j}}{d\bar{z}} = \frac{\bar{\beta}_z}{1-\bar{\beta}_z}\left(\frac{1}{\beta_{zj}}-1\right) \text{ where } \tfrac{\partial}{\partial\bar{z}}=\tfrac{1}{2k_w\rho}\tfrac{\partial}{\partial z} \quad (2.222)$$
$$= \frac{\bar{\beta}_z}{1-\bar{\beta}_z}\left(\frac{1-\beta_{zj}}{\beta_{zj}}\right) \text{ and } \tfrac{dt_j}{dz}=\tfrac{1}{v_j} \quad (2.223)$$
$$= \frac{1}{\varepsilon}\,\varepsilon Q_j \quad (2.224)$$
$$= Q_j \quad (2.225)$$

Equation 2.225 is the equation of the scaled electron "velocity" in the $\bar{z}_2$ direction. The corresponding electron equations in the $\bar{x}$ and $\bar{y}$ directions are now derived.

The electron equation describing evolution in the transverse plane is calculated from the definition of $\bar{p}_\perp$;

$$\bar{p}_{xj} = \gamma_j \beta_{xj} \tag{2.226}$$

$$= \gamma_j \frac{dx_j}{c\ dt} \tag{2.227}$$

$$\Rightarrow \frac{dx_j}{c\ dt} = \frac{\bar{p}_{xj}}{\gamma_j} \tag{2.228}$$

$$\Rightarrow \frac{dx_j}{d\bar{z}} = \frac{\bar{p}_{xj}}{2k_w \rho \beta_{zj} \gamma_j} \tag{2.229}$$

$$\text{so that: } \frac{d\bar{x}_j}{d\bar{z}} = \frac{\bar{p}_{xj}}{2k_w \rho \beta_{zj} \gamma_j} 2\rho \sqrt{\frac{k}{k_w}} \tag{2.230}$$

$$= \frac{\bar{p}_{xj}}{\beta_{zj} \gamma_j \sqrt{\varepsilon}}. \tag{2.231}$$

Similarly for the $\bar{y}$ direction,

$$\frac{d\bar{y}_j}{d\bar{z}} = \frac{\bar{p}_{yj}}{\beta_{zj} \gamma_j \sqrt{\varepsilon}}. \tag{2.232}$$

The three electrons' axial equations have been derived. It is important to also calculate their initial values so they will propagate in a stable orbit. This is carried out in the next section.

2.6.8 Electron initial conditions

The initial conditions for the electrons in the transverse plane, $\bar{x}_0, \bar{y}_0$ and the momentum transverse plane, $\bar{p}_{x0}, \bar{p}_{y0}$ were obtained from the electron equations 2.190, for $\frac{d\bar{p}_{\perp j}}{d\bar{z}}$. The initial values vary depending on the starting point in $\bar{z}$. Usually $\bar{z} = 0$ is the initial position and as ε and ρ are $\ll 1$, we only take first order terms of ε and ρ. The relation between Q_j and p_j is exactly

$$Q_j = 1 - 2\rho\ p_j. \tag{2.233}$$

Recall that p_j appeared in the one-dimensional FEL equation 2.53 and described the relative energy variation. Taking equation 2.233 and substituting into equation 2.190 obtains:

$$\frac{d\bar{p}_{\perp j}}{d\bar{z}} = \frac{a_w}{2\rho}\left[i\exp\left\{-\frac{i\bar{z}}{2\rho}\right\} - \left(\frac{2\gamma_r\rho}{a_w}\right)^2 \varepsilon(1-2\rho\ p_j)A\exp\left\{-\frac{i\bar{z}_{2j}}{2\rho}\right\}\right] \tag{2.234}$$

$$\simeq \frac{a_w}{2\rho}\left[i\exp\left\{\frac{i\bar{z}}{2\rho}\right\} - \left(\frac{2\gamma_r\rho}{a_w}\right)^2 \varepsilon A\exp\left\{-\frac{i\bar{z}_{2j}}{2\rho}\right\}\right]. \tag{2.235}$$

A is assumed to be a constant. Before carrying out the integration on 2.235, the derivative of $\bar{z}_{2j}$ in equation 2.225 may be integrated with respect to $\bar{z}$, at $\bar{z}=0$, when the electrons are at resonance, to obtain:

$$\frac{d\bar{z}_{2j}}{d\bar{z}} \simeq 1 \tag{2.236}$$

$$\bar{z}_{2j} = \bar{z} + \bar{z}_{2j_0} \tag{2.237}$$

Continue with the integration of equation 2.235; the integral of $\bar{z}_{2j}$ over $\bar{z}$ is approximately unity therefore the integration of equation 2.235 yields:

$$\bar{p}_{\perp j} = \frac{a_w}{2\rho}\left(-i\frac{2\rho}{i}\exp\left\{-\frac{i\bar{z}}{2\rho}\right\} - \left(\frac{2\gamma_r\rho}{a_w}\right)^2 \varepsilon A\frac{2\rho}{-i}\exp\left\{-\frac{i\bar{z}_{2j}}{2\rho}\right\}\right) \tag{2.238}$$

$$= a_w\left(-\exp\left\{-\frac{i\bar{z}}{2\rho}\right\} - i\left(\frac{2\gamma_r\rho}{a_w}\right)^2 \varepsilon A\exp\left\{-\frac{i\bar{z}_{2j}}{2\rho}\right\}\right) \tag{2.239}$$

$$= -a_w\left(\exp\left\{-\frac{i\bar{z}}{2\rho}\right\} + i\left(\frac{2\gamma_r\rho}{a_w}\right)^2 \varepsilon A\exp\left\{-\frac{i\bar{z}_{2j}}{2\rho}\right\}\right) \tag{2.240}$$

$$\text{Also } \bar{p}^*_{\perp j} = -a_w\left(\exp\left\{\frac{i\bar{z}}{2\rho}\right\} - i\left(\frac{2\gamma_r\rho}{a_w}\right)^2 \varepsilon A^*\exp\left\{\frac{i\bar{z}_{2j}}{2\rho}\right\}\right) \tag{2.241}$$

At the beginning of the wiggler, before any interaction has taken place between the field and the electrons, A is small.

$$\Rightarrow \bar{p}_{\perp j} = -a_w\exp\left\{-\frac{i\bar{z}}{2\rho}\right\}. \tag{2.242}$$

The real and imaginary parts of $\bar{p}_{\perp j}$ are related to $\bar{p}_x$ and $\bar{p}_y$ from equation 2.98 so the initial values of the scaled momentum are

$$\Re(\bar{p}_\perp) = \bar{p}_{x_0} = -a_w\cos\frac{\bar{z}}{2\rho} \tag{2.243}$$

$$\Im(\bar{p}_\perp) = \bar{p}_{y_0} = -a_w\sin\frac{\bar{z}}{2\rho}. \tag{2.244}$$

If the electrons are centred around these initial values, at $\bar{z} = 0$ then $\bar{p}_{x_0} = -a_w$ and $\bar{p}_{y_0} = 0$.

The next step is to calculate the initial conditions for $\bar{x}$ and $\bar{y}$. It is important that the electrons are initially positioned correctly so that when they propagate through the undulator they travel along a stable orbital path. For example, in the absence of any FEL interaction between the field and the electrons, the electrons' trajectories would have a helical motion inside the undulator as expected, for a properly injected beam.

Now $\bar{x}_0$ and $\bar{y}_0$ are calculated from the momentum,

$$\bar{p}_{x_j} = \frac{p_x}{mc} = \frac{\gamma_j m v_{xj}}{mc} \tag{2.245}$$

$$\frac{\gamma_j v_{xj}}{c} = -a_w \cos\frac{\bar{z}}{2\rho} \tag{2.246}$$

$$\frac{\gamma_j}{c}\frac{dx_j}{dt} = -a_w \cos\frac{\bar{z}}{2\rho} \quad \text{since } \tfrac{d}{dt}=2k_w\rho c\beta_{zj}\tfrac{d}{d\bar{z}} \tag{2.247}$$

$$\frac{\gamma_j}{c}2k_w\rho c\beta_{zj}\frac{dx_j}{d\bar{z}} = -a_w \cos\frac{\bar{z}}{2\rho} \tag{2.248}$$

$$\frac{dx_j}{d\bar{z}} = \frac{-a_w}{2k_w\rho\gamma_j\beta_{zj}} \cos\frac{\bar{z}}{2\rho} \tag{2.249}$$

$$\sqrt{l_g l_c}\,\frac{d\bar{x}_j}{d\bar{z}} = \frac{-a_w}{2k_w\rho\gamma_j\beta_{zj}} \cos\frac{\bar{z}}{2\rho} \tag{2.250}$$

$$\frac{d\bar{x}_j}{d\bar{z}} = \frac{-a_w}{2k_w\rho\gamma_j\beta_{zj}}\ 2\rho\sqrt{k_w k}\ \cos\frac{\bar{z}}{2\rho} \tag{2.251}$$

$$\frac{d\bar{x}_j}{d\bar{z}} = \frac{-a_w}{\gamma_j\beta_{zj}}\sqrt{\frac{k}{k_w}}\ \cos\frac{\bar{z}}{2\rho} \quad \text{whereas } \tfrac{k_w}{k}=\tfrac{1-\bar{\beta}_z}{\beta_z}=\varepsilon \tag{2.252}$$

$$\Rightarrow \frac{d\bar{x}_j}{d\bar{z}} = \frac{-a_w}{\gamma_j\beta_{zj}\ \sqrt{\varepsilon}}\ \cos\frac{\bar{z}}{2\rho} \tag{2.253}$$

Integrating the latter equation with respect to $\bar{z}$ and an expression of the initial condition in the $\bar{x}$ direction is obtained.

$$\bar{x}_{0j} = -\frac{2a_w\rho}{\gamma_j\beta_{zj}\ \sqrt{\varepsilon}}\ \sin\frac{\bar{z}_0}{2\rho} \tag{2.254}$$

Similar calculations was performed for the $\bar{y}$ direction yields

$$\bar{y}_{0j} = \frac{2a_w\rho}{\gamma_j\beta_{zj}\ \sqrt{\varepsilon}}\ \cos\frac{\bar{z}_0}{2\rho}. \tag{2.255}$$

The β_{zj} parameter found in equations 2.254 and 2.255 can be defined using

the definition of εQ_j in equation 2.158.

$$\beta_{zj} = \frac{1}{1+\varepsilon Q_j}. \tag{2.256}$$

As previously stated, before any interaction takes place $Q_j \simeq 1$, therefore

$$\beta_{zj_0} = \frac{1}{1+\varepsilon} \tag{2.257}$$

where ε is given by

$$\varepsilon = \frac{1+a_w^2}{2\gamma_r^2},$$

which is the resonance condition. The γ_j^{-1} parameter found in equations 2.254 and 2.255 was also computed using equation 2.213 at $\bar{z} = 0$;

$$\gamma_{j_0}^{-2} = \frac{1-\beta_{zj}^2(\bar{z}_0)}{1+|\bar{p}_\perp|_j^2} \tag{2.258}$$

$$= \frac{1-\bar{\beta}_z^2}{1+a_w^2} \tag{2.259}$$

where $|\bar{p}_\perp|_j^2 = \bar{p}_\perp \bar{p}_\perp^* = a_w^2$ see equation (2.242)

$$\Rightarrow \gamma_{j_0}^{-2} = \frac{1-\left(\frac{1}{1+\varepsilon}\right)^2}{2\gamma_r^2\varepsilon} \tag{2.260}$$

$$= \frac{\varepsilon^2+2\varepsilon}{2\gamma_r^2\varepsilon}\frac{1}{(1+\varepsilon)^2} \tag{2.261}$$

$$= \frac{\varepsilon+2}{2\gamma_r^2(1+\varepsilon)^2} \tag{2.262}$$

$$\Rightarrow \gamma_{j_0}^{-1} = \frac{\sqrt{\varepsilon+2}}{\sqrt{2}\gamma_r(1+\varepsilon)} \tag{2.263}$$

and the coefficient of $\bar{x}$ and $\bar{y}$ in equations 2.254 and 2.255 becomes

$$\frac{2a_w\rho}{\gamma_{j_0}\beta_{zj_0}\sqrt{\varepsilon}} = 2a_w\rho\frac{\sqrt{\varepsilon+2}}{\sqrt{2}\gamma_r(1+\varepsilon)}\frac{1+\varepsilon}{\sqrt{\varepsilon}} \tag{2.264}$$

$$= \frac{2a_w\rho}{\gamma_r}\frac{\sqrt{\varepsilon+2}}{\sqrt{2}}\frac{1}{\sqrt{\varepsilon}} \tag{2.265}$$

$$= \frac{2a_w\rho}{\gamma_r}\sqrt{1+\frac{\varepsilon}{2}}\frac{1}{\sqrt{\varepsilon}} \tag{2.266}$$

$$= \frac{2a_w\rho}{\gamma_r}\sqrt{\frac{1}{\varepsilon}+\frac{1}{2}} \tag{2.267}$$

After all the calculations, the final form of all the initial values are therefore:

$$\bar{x}_0 = -\frac{2a_w\rho}{\gamma_r}\sqrt{\frac{1}{\varepsilon}+\frac{1}{2}}\ \sin\frac{\bar{z}_0}{2\rho} \tag{2.268}$$

$$\bar{y}_0 = \frac{2a_w\rho}{\gamma_r}\sqrt{\frac{1}{\varepsilon}+\frac{1}{2}}\ \cos\frac{\bar{z}_0}{2\rho} \tag{2.269}$$

$$\bar{p}_{x_0} = -a_w\cos\frac{\bar{z}}{2\rho} \tag{2.270}$$

$$\bar{p}_{y_0} = -a_w\sin\frac{\bar{z}}{2\rho} \tag{2.271}$$

These initial values are the central values for the electron variables. For example, if the length of the electron pulse in the $\bar{x}$ is 1, $a_w = 2$, $\gamma_r = 100$ and $\rho = 1/40\pi$. Generally, the range of electron pulse would be $-0.5 < \bar{x} < 0.5$, centred at 0. When the initial offset value is included the central value the range would be $\approx -0.4799 < \bar{x} < 0.5201$.

Up to this point, all the FEL equations and appropriate initial conditions have been derived. One can show that the calculations of the FEL equations above satisfy the conservation of energy. The next section calculates such a conservation equation from the FEL equations.

2.6.9 Conservation of momentum and energy

In the first part of the split-step method, diffraction acting alone is modelled and the r.h.s. of the field equation is set to zero. Thus, the conservation of energy and momentum due to diffraction is trivial. In the second part of the Split-Step, the r.h.s. is the source term which is a function of the sum of over the electrons. This equation determines the energy transfer between radiation and electrons, and this is the equation considered in the constant of motion.

$$\frac{\partial A}{\partial\bar{z}} = \frac{\gamma_r}{a_w}\frac{1}{\bar{n}_p}\sum_{j=1}^{N}\frac{\bar{p}_{\perp j}}{(1+|\bar{p}_\perp|^2)_j^{\frac{1}{2}}}(\varepsilon Q_j(\varepsilon Q_j+2))^{\frac{1}{2}}\delta(\bar{x}-\bar{x}_j)\delta(\bar{y}-\bar{y}_j)\delta(\bar{z}_2-\bar{z}_{2j})\exp\left\{i\frac{\bar{z}_2}{2\rho}\right\}. \tag{2.272}$$

The following steps are the calculations for the constant of motion; first one can multiply equation (2.190) by $\bar{p}^*_{\perp j}$ and add its complex conjugate, where $\alpha = \frac{2\gamma_r\rho}{a_w}$,

to give:

$$\frac{d|\bar{p}_{\perp j}|^2}{d\bar{z}} = \bar{p}^*_{\perp j}\frac{d\bar{p}_{\perp j}}{d\bar{z}} + \bar{p}_{\perp j}\frac{d\bar{p}^*_{\perp j}}{d\bar{z}} \tag{2.273}$$

$$\begin{aligned}\frac{d|\bar{p}_{\perp j}|^2}{d\bar{z}} &= \frac{a_w}{2\rho}\left[i\bar{p}^*_{\perp j}\exp\left\{\frac{-i\bar{z}}{2\rho}\right\} - i\bar{p}_{\perp j}\exp\left\{\frac{i\bar{z}}{2\rho}\right\}\right. \\ &\quad \left. - \left(\frac{2\gamma_r\rho}{a_w}\right)^2 \varepsilon Q_j\left(\bar{p}^*_{\perp j}A\exp\left\{\frac{-i\bar{z}_{2j}}{2\rho}\right\} + \bar{p}_{\perp j}A^*\exp\left\{\frac{i\bar{z}_{2j}}{2\rho}\right\}\right)\right] \qquad (2.274)\\ &= \frac{a_w}{2\rho}\left[i\left(\bar{p}^*_{\perp j}\exp\left\{\frac{-i\bar{z}}{2\rho}\right\} - c.c.\right) - \alpha^2\varepsilon Q_j\left(\bar{p}^*_{\perp j}A\exp\left\{\frac{-i\bar{z}_{2j}}{2\rho}\right\} + c.c.\right)\right]. \qquad (2.275)\end{aligned}$$

The same procedures were performed on equation 2.272. One can multiply equation 2.272 by A^* and add its complex conjugate:

$$\frac{d|A|^2}{d\bar{z}} = A^*\frac{dA}{d\bar{z}} + A\frac{dA^*}{d\bar{z}} \tag{2.276}$$

$$\begin{aligned}\frac{d|A|^2}{d\bar{z}} &= \frac{\gamma_r}{a_w}\frac{1}{\bar{n}_p}\sum_{j=1}^{N}\frac{\left(\bar{p}_{\perp j}A^*\exp\left\{\frac{i\bar{z}_2}{2\rho}\right\} + \bar{p}^*_{\perp j}A\exp\left\{\frac{-i\bar{z}_2}{2\rho}\right\}\right)}{(1+|\bar{p}_\perp|_j^2)^{\frac{1}{2}}} \\ &\qquad (\varepsilon Q_j(\varepsilon Q_j+2))^{\frac{1}{2}}\delta^3(\bar{x}_j,\bar{y}_j,\bar{z}_{2j}) \qquad (2.277)\\ &= \frac{\gamma_r}{a_w}\frac{1}{\bar{n}_p}\sum_{j=1}^{N}\frac{\left(\bar{p}^*_{\perp j}A\exp\left\{\frac{-i\bar{z}_2}{2\rho}\right\} + c.c.\right)}{(1+|\bar{p}_\perp|_j^2)^{\frac{1}{2}}}(\varepsilon Q_j(\varepsilon Q_j+2))^{\frac{1}{2}}\delta^3(\bar{x}_j,\bar{y}_j,\bar{z}_{2j}) \qquad (2.278)\end{aligned}$$

$\delta^3(\bar{x}_j,\bar{y}_j,\bar{z}_{2j})$ is short for $\delta(\bar{x}-\bar{x}_j)\delta(\bar{y}-\bar{y}_j)\delta(\bar{z}_2-\bar{z}_{2j})$. The relativistic factor from equation 2.213 was used again along with the definition of β_z in equation 2.256 to give:

$$\begin{aligned}\gamma^{-2} &= \frac{1-\beta_z^2}{1+|\bar{p}_\perp|^2} \qquad (2.279)\\ &= \frac{1-\frac{1}{(1+\varepsilon Q)^2}}{1+|\bar{p}_\perp|^2} \qquad (2.280)\\ \gamma^2 &= \frac{1+|\bar{p}_\perp|^2}{1-\frac{1}{(1+\varepsilon Q)^2}} \qquad (2.281)\\ &= \frac{1+|\bar{p}_\perp|^2}{\frac{(1+\varepsilon Q)^2-1}{(1+\varepsilon Q)^2}} \qquad (2.282)\\ &= \frac{(1+|\bar{p}_\perp|^2)(1+\varepsilon Q)^2}{(1+\varepsilon Q)^2-1}. \qquad (2.283)\end{aligned}$$

The expression in equation 2.283 has shown that γ_j is related to $\bar{p}_{\perp j}$ and Q_j.

The following calculations consists of incorporating the electrons momentum equations into a single expression and then substitute into equation 2.278. First differentiate γ_j with respect to $\bar{z}$:

$$\begin{aligned} \frac{d\gamma^2}{d\bar{z}} &= 2\gamma\frac{d\gamma}{d\bar{z}} \\ \frac{d\gamma}{d\bar{z}} &= \frac{1}{2\gamma}\frac{d\gamma^2}{d\bar{z}} \end{aligned} \tag{2.284}$$

and the expression of γ^2 in equation 2.283 is substituted into equation 2.284:

$$\begin{aligned} \Rightarrow \frac{d\gamma^2}{d\bar{z}} &= \frac{d}{d\bar{z}}\left(\frac{(1+|\bar{p}_\perp|^2)(1+\varepsilon Q)^2}{(1+\varepsilon Q)^2-1}\right) \\ &= (1+|\bar{p}_\perp|^2)\underbrace{\frac{d}{d\bar{z}}\left(\frac{(1+\varepsilon Q)^2}{(1+\varepsilon Q)^2-1}\right)}_{\text{D1}} + \frac{(1+\varepsilon Q)^2}{(1+\varepsilon Q)^2-1}\frac{d}{d\bar{z}}(1+|\bar{p}_\perp|^2). \end{aligned} \tag{2.285}$$

The derivative of the D1 term on equation (2.285) was computed and letting $u = (1+\varepsilon Q)$, where $\frac{du}{d\bar{z}} = \varepsilon\frac{dQ}{d\bar{z}}$;

$$\frac{d}{d\bar{z}}\left(\frac{u^2}{u^2-1}\right) = \frac{(u^2-1)2u\frac{du}{d\bar{z}} - u^2 2u\frac{du}{d\bar{z}}}{(u^2-1)^2} \tag{2.286}$$

$$= \frac{-2u\frac{du}{d\bar{z}}}{(u^2-1)^2}. \tag{2.287}$$

Substitute $u = 1+\varepsilon Q$ to get

$$\frac{d}{d\bar{z}}\left(\frac{(1+\varepsilon Q)^2}{(1+\varepsilon Q)^2-1}\right) = \frac{-2(1+\varepsilon Q)\varepsilon\frac{dQ}{d\bar{z}}}{((1+\varepsilon Q)^2-1)^2} \tag{2.288}$$

then substitute this expression back into equation 2.285 which yields

$$\Rightarrow \frac{d\gamma^2}{d\bar{z}} = -2(1+|\bar{p}_\perp|^2)\frac{(1+\varepsilon Q)}{((1+\varepsilon Q)^2-1)^2}\varepsilon\frac{dQ}{d\bar{z}} + \frac{(1+\varepsilon Q)^2}{(1+\varepsilon Q)^2-1}\frac{d|\bar{p}_\perp|^2}{d\bar{z}}. \tag{2.289}$$

Substitute this derivative 2.289 into equation 2.284 to give:

$$\begin{aligned}\frac{d\gamma}{d\bar{z}} &= \frac{((1+\varepsilon Q)^2-1)^{\cancel{\frac{1}{2}}^{-\frac{1}{2}}}}{2(1+|\bar{p}_\perp|)^{\frac{1}{2}}\cancel{(1+\varepsilon Q)}}\left[\frac{(1+\varepsilon Q)^{\cancel{2}^{1}}}{\cancel{(1+\varepsilon Q)^2-1}}\frac{d|\bar{p}_\perp|^2}{d\bar{z}} - \frac{2(1+|\bar{p}_\perp|^2)\cancel{(1+\varepsilon Q)}}{((1+\varepsilon Q)^2-1)^{\cancel{\frac{1}{2}}^{1}}}\,\varepsilon\frac{dQ}{d\bar{z}}\right] \\ &= \frac{1}{2(1+|\bar{p}_\perp|)^{\frac{1}{2}}((1+\varepsilon Q)^2-1)^{\frac{1}{2}}}\left[(1+\varepsilon Q)\frac{d|\bar{p}_\perp|^2}{d\bar{z}} - \frac{2(1+|\bar{p}_\perp|^2)}{(1+\varepsilon Q)^2-1}\,\varepsilon\frac{dQ}{d\bar{z}}\right] \\ &= \frac{1}{2(1+|\bar{p}_\perp|)^{\frac{1}{2}}(\varepsilon Q(\varepsilon Q+2))^{\frac{1}{2}}}\left[\underbrace{(1+\varepsilon Q)\frac{d|\bar{p}_\perp|^2}{d\bar{z}}}_{\text{D3}} - \underbrace{\frac{2(1+|\bar{p}_\perp|^2)}{(\varepsilon Q(\varepsilon Q+2))}\,\varepsilon\frac{dQ}{d\bar{z}}}_{\text{D2}}\right].\end{aligned} \tag{2.290}$$

The derivative of Q, equation (2.220), is substituted into the D2 term of equation (2.290). The D2 term is simplified as:

$$\begin{aligned}\frac{2(1+|\bar{p}_\perp|^2)}{\varepsilon Q(\varepsilon Q+2)}\,\varepsilon\frac{dQ_j}{d\bar{z}} &= \frac{\cancel{2(1+|\bar{p}_\perp|^2)}}{\cancel{\varepsilon Q(\varepsilon Q+2)}}\frac{a_w}{\cancel{4}\rho}\frac{\cancel{\varepsilon Q_j(\varepsilon Q_j+2)}}{\cancel{1+|\bar{p}_\perp|_j^2}}\left[i(\varepsilon Q_j+1)\left(\bar{p}^*_{\perp j}\exp\left\{\frac{-i\bar{z}}{2\rho}\right\}-c.c.\right)\right. \\ &\quad\left.+\alpha^2\varepsilon Q_j\left(\bar{p}^*_{\perp j}A\exp\left\{-i\frac{\bar{z}_{2j}}{2\rho}\right\}+c.c.\right)\right] \qquad (2.291) \\ &= \frac{a_w}{2\rho}\left[i(\varepsilon Q_j+1)\left(\bar{p}^*_{\perp j}\exp\left\{\frac{-i\bar{z}}{2\rho}\right\}-c.c.\right)\right. \\ &\quad\left.+\alpha^2\varepsilon Q_j\left(\bar{p}^*_{\perp j}A\exp\left\{-i\frac{\bar{z}_{2j}}{2\rho}\right\}+c.c.\right)\right]. \qquad (2.292)\end{aligned}$$

The D3 term in equation 2.290 can be written substituting the derivative of $\bar{p}_\perp$ from equation 2.190:

$$\begin{aligned}(1+\varepsilon Q_j)\frac{d|\bar{p}_{\perp j}|^2}{d\bar{z}} &= (1+\varepsilon Q_j)\frac{a_w}{2\rho}\left[i\left(\bar{p}^*_{\perp j}\exp\left\{\frac{-i\bar{z}}{2\rho}\right\}-c.c.\right)\right. \\ &\quad\left.-\alpha^2\varepsilon Q_j\left(\bar{p}^*_{\perp j}A\exp\left\{\frac{-i\bar{z}_{2j}}{2\rho}\right\}+c.c.\right)\right] \qquad (2.293)\end{aligned}$$

Now the expressions of D2 in equation 2.292 and D3 in equation 2.293 are added

together:

$$(1+\varepsilon Q_j)\frac{d|\bar{p}_\perp|^2}{d\bar{z}} - \frac{2(1+|\bar{p}_\perp|^2)}{(\varepsilon Q_j(\varepsilon Q_j+2))}\,\varepsilon\frac{dQ_j}{d\bar{z}} =$$
$$\frac{a_w}{2\rho}[\cancel{i(1+\varepsilon Q_j)(\bar{p}^*_{\perp j}e^{\frac{-i\bar{z}}{2\rho}} - c.c.)} - \alpha^2\varepsilon Q_j(1+\varepsilon Q_j)(\bar{p}^*_{\perp j}Ae^{\frac{-i\bar{z}_{2j}}{2\rho}} + c.c.)$$
$$\cancel{-i(\varepsilon Q_j+1)(\bar{p}^*_{\perp j}e^{\frac{-i\bar{z}}{2\rho}} - c.c.)} - \alpha^2\varepsilon Q_j(\bar{p}^*_{\perp j}Ae^{-i\frac{\bar{z}_{2j}}{2\rho}} + c.c.)]$$
$$= -\frac{a_w}{2\rho}(2\alpha^2\varepsilon Q_j + \alpha^2\varepsilon^2 Q_j^2)\ (\bar{p}^*_{\perp j}Ae^{\frac{-i\bar{z}_{2j}}{2\rho}} + c.c.) \tag{2.294}$$

and then substituting equation 2.294 back into in equation 2.290. $\frac{d\gamma}{d\bar{z}}$, then simplifies to:

$$\frac{d\gamma_j}{d\bar{z}} = \frac{-a_w}{4\rho}\frac{1}{(1+|\bar{p}_\perp|)^{\frac{1}{2}}(\varepsilon Q_j(\varepsilon Q_j+2))^{\frac{1}{2}}}\left[(\varepsilon Q_j(\varepsilon Q_j+2))\alpha^2\left(\bar{p}^*_{\perp j}A\exp\left\{\frac{-i\bar{z}_{2j}}{2\rho}\right\} + c.c.\right)\right]$$
$$= \frac{-a_w}{4\rho}\frac{(\varepsilon Q_j(\varepsilon Q_j+2))^{\frac{1}{2}}}{(1+|\bar{p}_\perp|)^{\frac{1}{2}}}\alpha^2\left(\bar{p}^*_{\perp j}A\exp\left\{\frac{-i\bar{z}_{2j}}{2\rho}\right\} + c.c.\right). \tag{2.295}$$

Finally, substituting the latter equation into equation 2.278;

$$\frac{d|A|^2}{d\bar{z}} = \frac{\gamma_r}{a_w}\frac{1}{\bar{n}_p}\sum_{j=1}^{N}\frac{-4\rho}{a_w\alpha^2}\frac{d\gamma}{d\bar{z}}\delta(\bar{x}-\bar{x}_j)\delta(\bar{y}-\bar{y}_j)\delta(\bar{z}_2-\bar{z}_{2j})$$
$$= \frac{-1}{\gamma_r\rho\bar{n}_p}\sum_{j=1}^{N}\frac{d\gamma}{d\bar{z}}\delta(\bar{x}-\bar{x}_j)\delta(\bar{y}-\bar{y}_j)\delta(\bar{z}_2-\bar{z}_{2j}) \text{ where } \tfrac{-4\rho\gamma_r}{a_w^2\bar{n}_p}\left(\tfrac{a_w^2}{4\gamma^2\rho^2}\right)=\tfrac{-1}{\gamma_r\rho\bar{n}_p}$$

$$\Rightarrow \frac{d|A|^2}{d\bar{z}} + \frac{1}{\gamma_r\rho\bar{n}_p}\sum_{j=1}^{N}\frac{d\gamma}{d\bar{z}}\delta(\bar{x}-\bar{x}_j)\delta(\bar{y}-\bar{y}_j)\delta(\bar{z}_2-\bar{z}_{2j}) = 0. \tag{2.296}$$

All of the FEL equations are now coupled in a single equation which is used to check the constant of motion. The energy must be conserved between the electrons and the radiation.

One can now solve equation 2.296 by integrating it over $\bar{x}$, $\bar{y}$ and $\bar{z}_2$ plane from $-\infty$ to ∞, and $\tilde{A} = \int_{\bar{x}}\int_{\bar{y}}\int_{\bar{z}_2} A\ d\bar{z}_2 d\bar{y} d\bar{x}$ is defined.

$$\frac{d|\tilde{A}|^2}{d\bar{z}} + \sum_{j=1}^{N}\frac{1}{\gamma_r\rho\bar{n}_p}\frac{d\gamma_j}{d\bar{z}} = 0 \tag{2.297}$$

$$\Rightarrow \frac{d}{d\bar{z}}\left(|\tilde{A}|^2 + \sum_{j=1}^{N}\frac{1}{\gamma_r\rho\bar{n}_p}\gamma_j\right) = 0. \tag{2.298}$$

To convert real electrons to macroparticles, the summation must be changed to

$$\frac{1}{\bar{n}_p}\sum_{j=1}^{N} = \sum_{k=1}^{N_m}\bar{\chi}_k. \tag{2.299}$$

The summation in equation 2.298 maybe replaced with the new summation and the constant of motion expression becomes:

$$\frac{d}{d\bar{z}}\left(|\tilde{A}|^2 + \frac{1}{\gamma_r\rho}\sum_{k=1}^{N_m}\bar{\chi}_k\gamma_k\right) = 0 \tag{2.300}$$

$$\text{where } \gamma_k = \sqrt{\frac{(1+|\bar{p}_{\perp k}|^2)(1+\varepsilon Q_k)^2}{\varepsilon Q_k(\varepsilon Q_k+2)}}.$$

Straight forward integration was performed on equation 2.300 with respect to $\bar{z}$ and the r.h.s. is a constant which would be the initial value at $\bar{z} = 0$

$$|\tilde{A}|^2 + \frac{1}{\gamma_r\rho}\sum_{k=1}^{N_m}\bar{\chi}_k\gamma_k = |\tilde{A}|_0^2 + \frac{1}{\gamma_r\rho}\sum_{k=1}^{N_m}\bar{\chi}_k\gamma_{k0} \tag{2.301}$$

$$\int_{\bar{x}}\int_{\bar{y}}\int_{\bar{z}_2}(|A|^2 - |A|_0^2)\; d\bar{z}_2 d\bar{y} d\bar{x} + \frac{1}{\gamma_r\rho}\sum_{k=1}^{N_m}\bar{\chi}_k(\gamma_k - \gamma_{k0}) = 0. \tag{2.302}$$

The equation of the conservation of energy (2.302) has been derived and is an useful equation to check whether the numerical results in the 3D FEL model has been solved correctly.

When a non-zero emittance electron beam is used, the radius of a Gaussian electron beam may be calculated according to the matched beam condition. A natural focussing of the undulator forced the electrons to oscillate within its beam envelope and the matched beam radius would remain a constant as the electron beam propagates along the undulator. These focussing effects and matched beam condition are discussed in the next section.

2.6.10 Electron dynamics in the undulator

The magnetic field from the helical undulator forms a sinusoidal wave in three dimensional space and the electrons' trajectory path is affected by this helical magnetic field. When the emittance of the electron beam is non-zero, the electrons propagate with a random transverse velocity about the mean without any focussing. When the undulator is long, a focussing in both transverse planes is required so the electrons stay inside a beam envelope. The motion of the electrons with a linear focussing is sinusoidal and they oscillate inside the beam envelope.

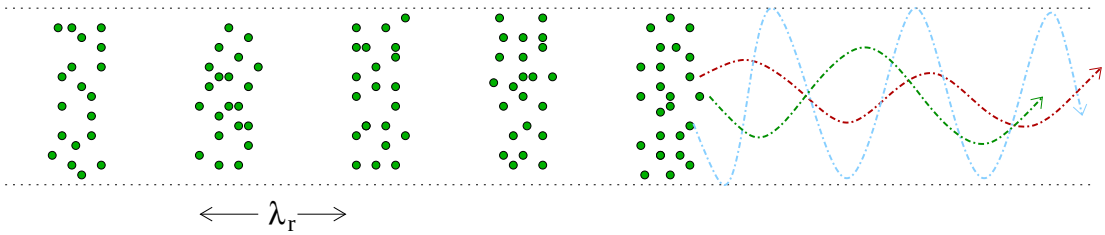

Figure 2.15: The electrons bunch over a radiation period and are confined within their beam envelope. Trajectories are shown on right.

The focussing force may be included in the momentum equation. A restoring force is naturally present in a helical undulator. This natural focussing is weaker than external focussing, such as a lattice of magnetic quadrupoles. The oscillating motion of the electrons in a focussing lattice is called a betatron motion.

This is shown schematically in figure 2.15. Each individual electron oscillates inside an envelope due to the natural focussing force. In a helical undulator, natural focussing occurs in both x and y planes and other focussing is not required. The natural focussing force defined in [31] for a helical undulator is

$$\frac{d^2x}{dz^2} = -k_{\beta h}^2 x, \tag{2.303}$$

$$\frac{d^2y}{dz^2} = -k_{\beta h}^2 y \tag{2.304}$$

$$\text{where } k_{\beta h}^2 = \frac{a_w^2 k_w^2}{2\gamma^2}. \tag{2.305}$$

The betatron wave number is denoted by $k_{\beta h}$. The restoring force of equations 2.303 and 2.304 is then added to the existing momentum equation $\frac{d\bar{p}_\perp}{d\bar{z}}$ (2.190). These terms were ignored when deriving the electron's momentum equation in section 2.6.5 in the calculation of the cross product in equations 2.186–2.187.

The magnetic field, due to the undulator, used in the derivation in equations 2.186–2.187 is only valid near the on-axis plane where there is a small deviation of the longitudinal magnetic field away from zero about the axis. The expression of $\boldsymbol{B}$ as defined in equation 2.4 does not satisfy the Maxwell equation in the absence of a current:

$$\nabla \times \boldsymbol{B} = 0. \tag{2.306}$$

The total magnetic field equation from a helical undulator in full should in fact

be written:

$$\boldsymbol{B}_w = B_w(\sin k_w z\ \underline{\hat{x}}, \cos k_w z\ \underline{\hat{y}}, k_w x \cos k_w z + k_w y \sin k_w z\ \underline{\hat{z}}). \tag{2.307}$$

To include the restoring force in the momentum equation, an expression for the scaled momentum in terms of the focussing derivatives may be derived from the momentum equation as follows:

$$\bar{p}_{xj} = \frac{\gamma_j}{c}\frac{dx_j}{dt} \tag{2.308}$$

$$\frac{d\bar{p}_{xj}}{dt} = \frac{\gamma_j}{c}\frac{d^2x_j}{dt^2} \tag{2.309}$$

$$2k_w\rho\beta_{zj}c\frac{d\bar{p}_{xj}}{d\bar{z}} = (2k_w\rho)^2\frac{\gamma_j}{c}(\beta_{zj}c)^2\frac{d^2x_j}{d\bar{z}^2} \tag{2.310}$$

$$\frac{d\bar{p}_{xj}}{d\bar{z}} = 2k_w\rho\gamma_j\beta_{zj}\frac{d^2x_j}{d\bar{z}^2}. \tag{2.311}$$

The focussing equation is presented in equation 2.303 for the x direction in SI units and some scaling must be applied to this equation so it can be substituted into equation 2.311:

$$\frac{d^2x_j}{dz^2} = -k_{\beta j}^2 x_j \tag{2.312}$$

$$(2k_w\rho)^2\frac{d^2\bar{x}_j}{d\bar{z}^2} = -k_{\beta j}^2\bar{x}_j \tag{2.313}$$

$$\frac{d^2\bar{x}_j}{d\bar{z}^2} = \frac{-k_{\beta j}^2\bar{x}_j}{4k_w^2\rho^2} \tag{2.314}$$

$$= -\frac{1}{4k_w^2\rho^2}\frac{a_w^2k_w^2}{2\gamma^2}\bar{x}_j \tag{2.315}$$

$$= -\frac{a_w^2}{8\rho^2\gamma^2}\bar{x}_j \tag{2.316}$$

$$= -\bar{k}_{\beta j}^2\bar{x}_j \text{ where } \bar{k}_{\beta j}^2 = \frac{a_w^2}{8\rho^2\gamma^2}. \tag{2.317}$$

Now, the newly scaled betatron wave number is defined as, $\bar{k}_{\beta j} = \frac{a_w}{2\sqrt{2}\rho\gamma}$ and the scaled focussing equation, 2.317, in $\bar{x}$ direction will now substitute into equation

2.311, giving:

$$\frac{d\bar{p}_{xj}}{d\bar{z}} = 2k_w\rho\gamma_j\beta_{zj}\sqrt{l_g l_c}\frac{d^2\bar{x}_j}{d\bar{z}^2} \tag{2.318}$$

$$= -2k_w\rho\gamma_j\beta_{zj}\sqrt{l_g l_c}\frac{a_w^2}{8\rho^2\gamma^2}\bar{x}_j \tag{2.319}$$

$$= -\frac{a_w^2\beta_{zj}}{4\rho\gamma_j}\frac{k_w}{2\rho\sqrt{k_w k}}\ \bar{x}_j \tag{2.320}$$

$$= -\frac{a_w^2\beta_{zj}\sqrt{\epsilon}}{8\rho^2\gamma_j}\ \bar{x}_j. \tag{2.321}$$

For the $\bar{y}$ direction, the scaled focussing force equation in y has the same coefficient as in equation 2.321,

$$\frac{d\bar{p}_{yj}}{d\bar{z}} = -\frac{a_w^2\beta_{zj}\sqrt{\epsilon}}{8\rho^2\gamma_j}\ \bar{y}_j \tag{2.322}$$

to obtain:

$$\frac{d\bar{p}_{\perp}}{d\bar{z}} = \frac{d(\bar{p}_x - i\bar{p}_y)}{d\bar{z}} = \frac{a_w^2\beta_{zj}\sqrt{\epsilon}}{8\rho^2\gamma_j}(-\bar{x}_j + i\bar{y}_j). \tag{2.323}$$

The focussing force is then applied on the transverse plane in order to keep the electrons focussed within their beam envelope. Therefore the radius of the transverse beam envelope, r_σ, remains a constant as it propagates along a helical undulator. This equilibrium radius can be calculated from the emittance (ϵ) of the electron beam and the betatron wave number [31].

$$r_\sigma = \left(\frac{\epsilon}{k_\beta}\right)^{1/2} \tag{2.324}$$

The performance of an FEL is greatly dependent on the emittance and diffraction, as discussed in the section 2.6.11. When an electron beam is said to be matched, the transverse area of the beam does not vary as it propagates through the undulator. For a relativistic electron beam, the emittance is defined as

$$\epsilon_x = \sigma_x\sigma_{x'} \text{ where } {}^{x'=\frac{dx}{dz}} \tag{2.325}$$

and similarly for y. Often a value of normalised beam emittance, ϵ_{xn}, is used instead of ϵ_x, so it is easier to compute the matched beam radius in terms of ϵ_{xn}. The relationship between beam emittance and normalised beam emittance

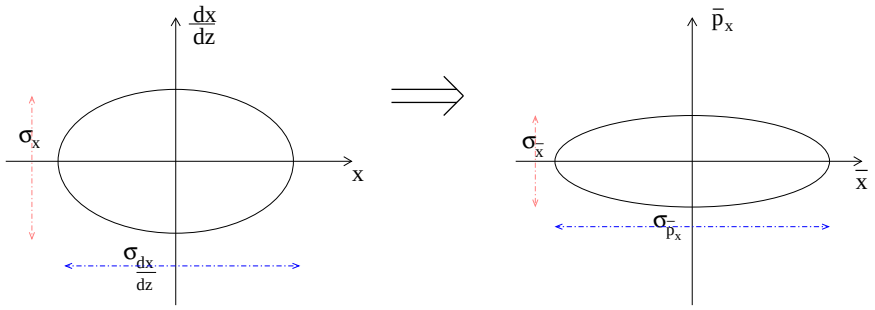

Figure 2.16: On the left, the emittance of an electron beam is in $(x,\ x^{'})$. After the scaling is applied to this emittance phase, it is changed to $(\bar{x},\bar{p}_x)$ as shown on the right.

is defined as

$$\epsilon_{xn} = \epsilon_x \gamma_r \tag{2.326}$$

$$= \gamma_r \sigma_x \sigma_{x'} \tag{2.327}$$

and σ_x is the the spread in a gaussian distribution beam in the x direction, correspondingly, $\sigma_{x'}$ is for the $\dfrac{dx}{dz}$ direction. The variables in the emittance equation required to be scaled in terms of $\sigma_{\bar{x}}$ and $\sigma_{\bar{p}_x}$; a simple diagram in figure 2.16 illustrates the conversion of the emittance variables. The updated emittance equation is

$$\epsilon_{xn} = \sqrt{l_g l_c}\sigma_{\bar{x}}\sigma_{\bar{p}_x} \tag{2.328}$$

The detailed mathematics on how $x^{'}$ relates to $\bar{p}_x$ is shown in appendix B. The expression of the normalised beam emittance is in scaled units and can be substituted into the matched beam condition equation 2.324. The definition of $\bar{k}_\beta$ was given in equation 2.317 and $l_c = \varepsilon l_g$, which are used in the following derivations.

$$r_\sigma = \left(\frac{\epsilon_n}{\gamma_r k_\beta}\right)^{1/2} \tag{2.329}$$

$$= \left(\frac{\epsilon_n l_g}{\gamma_r \bar{k}_\beta}\right)^{1/2} \tag{2.330}$$

$$\sqrt{l_g l_c}\bar{r}_\sigma = \left(\frac{\epsilon_n l_g}{\gamma_r \bar{k}_\beta}\right)^{1/2} \tag{2.331}$$

$$\bar{r}_\sigma = \left(\frac{\epsilon_n}{\gamma_r \bar{k}_\beta l_c}\right)^{1/2} \tag{2.332}$$

$$= \left(\frac{\sqrt{8}\rho\gamma_r\epsilon_n}{\varepsilon a_w \gamma_r l_g}\right)^{1/2} \tag{2.333}$$

$$\Rightarrow \bar{r}_\sigma = \left(\frac{\sqrt{8}\rho\epsilon_n}{\varepsilon a_w l_g}\right)^{1/2} \tag{2.334}$$

The matched beam radius, $\bar{r}_\sigma$, is the r.m.s. radius of a gaussian beam. When the beam emittance on both $\bar{x}$ and $\bar{y}$ plane is considered to be the same so this is said to be a circular beam and a general notation of the standard deviation σ is used.

$$\sigma = \sigma_{\bar{x}} = \sigma_{\bar{y}} \tag{2.335}$$

The equation for computing the individual $\sigma_{\bar{x}}$ or $\sigma_{\bar{y}}$ if the beam emittance has an elliptical shape would be

$$\bar{r}_\sigma = \sqrt{\frac{\sigma_{\bar{x}}^2 + \sigma_{\bar{y}}^2}{2}} \tag{2.336}$$

The standard deviation in $\bar{p}_x$ or $\bar{p}_y$ could be calculated using equation 2.328 along with the calculated $\sigma_{\bar{x}}$ or $\sigma_{\bar{y}}$ in equation 2.336

$$\bar{p}_x = \frac{\epsilon_{xn}}{\sqrt{l_g l_c}\sigma_{\bar{x}}}, \bar{p}_y = \frac{\epsilon_{yn}}{\sqrt{l_g l_c}\sigma_{\bar{y}}} \tag{2.337}$$

In this section a complete momentum equation has been derived as shown below:

$$\Rightarrow \frac{dp_{\perp j}}{d\bar{z}} = \frac{a_w}{2\rho}\left[i\exp\left\{-\frac{i\bar{z}}{2\rho}\right\} - \left(\frac{2\gamma_r\rho}{a_w}\right)^2 \varepsilon Q_j A \exp\left\{-\frac{i\bar{z}_{2j}}{2\rho}\right\}\right] + \frac{a_w^2\beta_{zj}\sqrt{\epsilon}}{8\rho^2\gamma_j}(-\bar{x}_j + i\bar{y}_j) \tag{2.338}$$

Equation 2.338 is coded in the simulation code and if the electron beam has zero emittance then the last term in this equation is set to zero. Otherwise the

full equation is calculated when emittance is non-zero.

The final equations of the 3D system are presented in the next section where the effects of diffraction are briefly investigated in the scaled unit used here.

2.6.11 Diffraction

One of the main features of the new three dimensional calculations is the effects of the diffraction on the transverse plane. Recall the final form of the scaled Maxwell wave equation is

$$-i\rho\left(\frac{\partial^2 A}{\partial\bar{x}^2}+\frac{\partial^2 A}{\partial\bar{y}^2}\right)+\frac{\partial A}{\partial\bar{z}}+2i\rho\frac{\partial^2 A}{\partial\bar{z}\partial\bar{z}_2}=\frac{\gamma_r}{a_w}\frac{\partial}{\partial\bar{z}_2}\sum_{k=1}^{N_m}\bar{\chi}_k\frac{\bar{p}_{\perp k}}{(1+|\bar{p}_\perp|^2)_k^{\frac{1}{2}}}$$
$$(\varepsilon Q_k(\varepsilon Q_k+2))^{\frac{1}{2}}\delta(\bar{x}-\bar{x}_k)\delta(\bar{y}-\bar{y}_k)\delta(\bar{z}_2-\bar{z}_{2k})\exp\left\{i\frac{\bar{z}_2}{2\rho}\right\} \quad (2.339)$$

where A the scaled complex field envelope. Diffraction effects are described implicitly in the solution of A. Previously, an analytical solution of A for the first half of the SSFM was displayed in equation 2.147 and the effects of diffraction were included in this solution. It was then used as an initial value for the next half-step of the integration. At the end of the propagation step, the solution will also include the electron source term which drives the radiation field. The diffraction theory is now briefly discussed.

At the beginning of the interaction ($z = 0$) there may be a Gaussian transverse intensity profile and by definition the intensity of the radiation reduces to $1/e^2$ of its peak value after propagation of one Rayleigh range distance from $z = 0$. The radiation transversely spreads out as it propagates along the undulator. This is the effect of diffraction. Generally a gaussian beam intensity profile is given in the following form:

$$I(r,z)\sim|\xi_0(r)|^2\exp\left\{\frac{-2r^2}{w^2}\right\}. \quad (2.340)$$

The beam waist, w, and radius r, are the distances from the z axis as shown in figure 2.17. The beam waist as a function of z is given by:

$$w(z)=w_0\sqrt{1+\frac{z^2}{z_R^2}}. \quad (2.341)$$

The beam waist at $z = 0$ is denoted by w_0, this position was also shown in figure

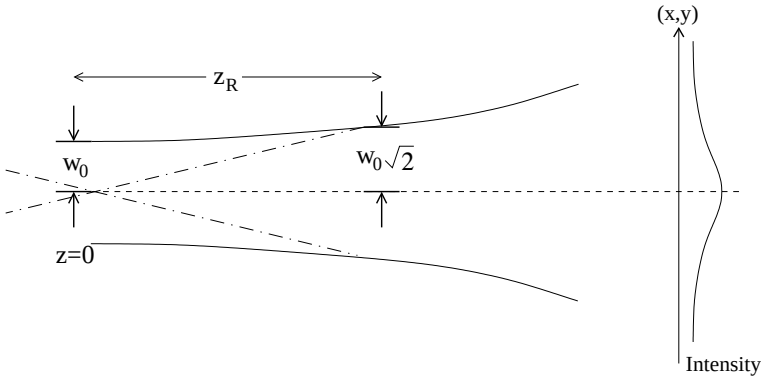

Figure 2.17: The beam waist of the intensity in the transverse plane at $z = 0$ is w_0. After one Raleigh range the beam waist increases to $\sqrt{2}w_0$.

2.17 and z_R is called the Rayleigh range defined by:

$$z_R = \frac{\pi w_0^2}{\lambda_r}. \tag{2.342}$$

At $z = 0$ and $z = \infty$ the wavefront is planar. As the beam propagates along z; the wavefront curvature starts to increase, then after a maximum is reached, it decreases. Interestingly, the point where the curvature of the wavefront is at its maximum is the Rayleigh range, $z = z_R$. The beam waist at z_R is $\sqrt{2}w_0$, as derived from equation 2.341:

$$w(z = z_R) = w_0\sqrt{1 + \frac{z_R^2}{z_R^2}} \tag{2.343}$$

$$= w_0\sqrt{2}. \tag{2.344}$$

When the beam has travelled to two Rayleigh ranges, the beam waist would be $\sqrt{5}w_0$ using equation 2.341. From this relationship, the size of a Gaussian beam on the transverse plane can be calculated for any given longitudinal distance away from $z = 0$. Even though the effects of diffraction are not described explicitly in the wave equation, by measuring the beam waist of a Gaussian beam, one is able to say whether the diffraction has been calculated correctly in the simulation code. This is shown in chapter 4.

As previously discussed, the intensity of the field drops to $1/e^2$ at z_R, this is connected to the spread in a Gaussian distribution and may be represented by

$$G = \exp\left\{\frac{(x-\mu)^2}{2\sigma^2}\right\} \tag{2.345}$$

where $\sigma > 0$ is the standard deviation and μ is the mean. The Gaussian is centred at the origin so the value of $\mu = 0$. Equating the intensity drop to a Gaussian distribution when $x = z_R$

$$\exp\{-2\} = \exp\left\{\frac{-x^2}{2\sigma^2}\right\} \tag{2.346}$$

$$-2 = -\frac{x^2}{2\sigma^2} \tag{2.347}$$

$$x^2 = 4\sigma^2 \tag{2.348}$$

$$x = 2\sigma \quad (x = -2\sigma \text{ is invalid.}) \tag{2.349}$$

The relation between w and σ has established, $w = 2\sigma$. The σ is the standard deviation of the power of the field, so the notation should be $\sigma = \sigma_p$. However, the value used as an input is the σ_f, the sigma spread of the field. Therefore $\sigma_f = \sqrt{2}\sigma_p$. Writing the beam waist at one Raleigh range in terms of σ_f is

$$w(z_R) = \sqrt{2}(2\sigma_p) = 2\sigma_f \tag{2.350}$$

and after two Raleigh range, $w(2z_R) = \sqrt{10}\sigma_f$.

The Raleigh range equation in SI units was defined in equation 2.342 and it is scaled as follow using the relation between the beam waist and σ_f,

$$\bar{z}_R = \frac{z_R}{l_g} \tag{2.351}$$

$$= \frac{\pi w_0^2}{\lambda_r l_g} \tag{2.352}$$

$$= \frac{\pi}{\lambda_r}\frac{l_g l_c \bar{w}_0^2}{l_g} \tag{2.353}$$

$$= \frac{\pi}{\lambda_r} l_c \bar{w}_0^2 \tag{2.354}$$

$$= \frac{\cancel{\pi}}{\cancel{\lambda_r}}\frac{\cancel{\lambda_r}}{4\cancel{\pi}\rho} 2\sigma_f^2 \tag{2.355}$$

$$= \frac{\sigma_f^2}{2\rho}. \tag{2.356}$$

Here σ_f is the sigma of the electron beam either for $\bar{x}$ direction, $\sigma_{\bar{x}}$, or $\bar{y}$ direction, $\sigma_{\bar{y}}$.

The last section of this chapter gives a summary of all input parameters and describes how the simulation code operates using parallel processors.

2.7 Numerical theory of the 3D model

In the 3D simulation code, there are three different numerical methods used and many general mathematical subroutines, so it was important to construct the code carefully. The layout of the code is divided into four parts; The constructor, `Main.f90`, the initialisation, `FEMethod.f90`, the numerical calculations, `SplitStepFunctions.f90, Derivtives.f90`, and the output, `sddsWriter.f90`. The simulation code is written to run on parallel processing machines and most of the routines used are supplied by NAG. Therefore most of the input parameters had to be imputed in certain order and additional arrays were set as 'Work' arrays used by NAG routines. The rk4 routine is a general routine from [19] which is not parallelised. There are also other routines called the BLACS (Basic Linear Algebra Communication Subprograms) routines provided by NAG, which communicate data between different processors. The two major NAG routines are the three dimensional Fast Fourier Transform (FFT) and Linear Solver (LS). Since these two routines are parallelised by NAG, the data was distributed using their own corresponding routines. Note that the way the data is distributed in FFT and LS is different. BLACS routines were used in transferring the data between these two routines.

2.7.1 Input file

The default input file name is `Run1.in` and it has sixty-two separate parameters. By making simple changes to `Main.f90`, the input file name can be read in at the terminal if more than one input file exists in the current folder. The following list is describes the essential input parameters required in the input file:

1. `nRowProcessors` and `nColProcessors` are the number of row and column processors to be used respectively. The maximum number of processors available on *hippo.phys.strath.ac.uk* are thirty-two. It is possible to use just one processor (1×1). Currently the optimum number of processors used running all the simulations is sixteen(4×4).

2. `qSeparateFiles` is a logical value for users to choose whether to store the output data in one file (`FALSE`) or in separate files (`TRUE`) for each step.

3. `qFormattedFiles` is a logical value that is either set to `TRUE` where the data to store in a ASCII formatted way and any user would be able to read the file. When it is set to `FALSE`, the data is written in binary; this is a disk saving option but the information can only be read by programs such as

MATLAB. If a quick test is to be carried out and one wished to see the output without using other programs, it is best to set this quantity to `TRUE`.

4. `sStepSize` is the integration step size, $d\bar{z}$. If the value is zero then this step size will be calculated automatically in `FEMethod.f90` and set to an eighth of $d\bar{z}_2$, the size an element in $\bar{z}_2$ direction. Ensure that the integration step size is small enough, $d\bar{z} < 0.5 \times d\bar{z}_2$, otherwise an error message will appear and the simulation will be stopped.

5. `nSteps` is the number of integration steps to take, if this parameter is set to zero then a number will be calculated so it will travel to one Rayleigh range with the corresponding `sStepsize`.

6. `sZ` is the starting position of the simulation, it is usually set at $z = 0$ and it is possible to begin the run at any point, given all the other information are correct, e.g. the initial field values.

7. `iWriteNthSteps` is the N^{th} number of steps to write the output data. For example when it is set to 1 then the output data will be written at every step, for 10 then at every 10^{th} step, e.g. $0, 10, 20, 30$.

8. `qWriteZ`, `qWriteA`, `qWriteP`, `qWriteQ`, `qWriteZ2`, `qWriteX`, `qWriteY` are all logical flags, if they are set to `TRUE` then the data for $\bar{z}$, A, $\bar{p}_\perp$, Q, $\bar{z}_2$, $\bar{x}$, $\bar{y}$ are to be stored in files.

9. `sLenEPulse` is an array with a fixed size of six corresponding to the electron pulse six phase-space dimensions, $\bar{x}$, $\bar{y}$, $\bar{z}_2$, $\bar{p}_x$, $\bar{p}_y$, $\bar{p}_{z2}$, `sLenEPulse(1)` for $\bar{x}$ direction, etc. It is possible to set `sLenEPulse(4-6)` to zero, (better to be 1×10^{-6}) which means that the electron beam is perfectly mono-energetic. The three spacial dimensions, must have a non-zero value, it is not physically correct to have a beam size of zero.

10. `iNumElm` is number of elements required for each spacial dimension. This is an array with a fixed size of three.

11. `sWigglerLength` is an array containing the slippage length in $\bar{z}_2$ to allow for electron propagation, and transverse lengths to allow for diffraction.

12. `i_RealE` is the number of real electrons in the electron beam, if the charge of the electron beam is $Q_c = 1nC$ then this value is approximately 6.24×10^9.

13. `q_noise` is a logical determining whether shot-noise exists in the electron beam. When to `TRUE`, the macroparticle positions are randomised using fortran its own random number routine. The particles will be spaced evenly along the range of the electron beam if `FALSE`.

14. `iNumElectrons` is the number of macro-electrons used in all six dimensions so this is an array with a fixed size of six. It is important to ensure that there must be at least one electron per $d\bar{z}_2$ element, not including any macro-electrons in the transverse plane. An additional restriction applies depending on other factors such as the shape of the electron beam distribution. This point will be discussed further in the next section.

15. `sSigmaElectrons` is the sigma spread for a Gaussian electron beam in six dimensions and therefore is an array. When it is set to a large value like 1×10^8 then the shape of the electron beam is a 'top-hat'. It should not be any value too small (7×10^{-3}), otherwise the Gaussian routine fails and causes the simulation to stop. This quantity is calculated in the transverse phase-space plane when a matched beam is used.

16. `sElectronThreshold` is a percentage the averaged number of real electrons per macro-electrons will be removed in the electron beam. For example, this quantity is 1.0 and the averaged value of real electrons is 2000 per macro-electron then any macro-electron which has 1% of 2000 which is 20 real electrons will be removed since the impact of these macro-electrons are negligible.

17. `sA0_Re` and `sA0_Im` are the initial values of the A for the real and imaginary part.

18. `sEmit_n` is the normalised emittance value of the electron beam in SI units.

19. `rho` is the Pierce parameter.

20. `aw` is the wiggle parameter defined in equation 1.7.

21. `gamma_r` is the resonant relativistic factor.

22. `sFocusfactor` is set to $\sqrt{2}$ for a natural helical undulator focussing. It could be varied to simulate different strengths of the focussing.

23. `sWigglerWavelength` is λ_w, the undulator period.

24. `sSeedSigma` is a sigma spread of a gaussian distribution initial radiation field, if present, in all three space dimensions. This value will be set equal to the sigma value of the electron beam if matched beam is used.

25. `qDiffraction` is a logical flag, which is set to `TRUE` when the effects of diffraction on the transverse plane are included and `FALSE` otherwise. More elements are required in the transverse plane where diffraction is simulated to ensure there is enough space for the field to diffract.

26. `qFieldEvolve` is set to `FALSE` logical to ignore when the electron source term in the wave equation.

27. `qElectronsEvolve` is a logical value and it determines whether the electrons' equation are solved.

28. `qElectronFieldCoupling` is a logical flag set to allow the radiation field to interact with the electrons. When the value is `FALSE` the electrons are not be affected by the radiation field.

29. `qInitialGaussField` is a logical flag that if set to `TRUE`, a Gaussian initial seed field is used whereas there will be a constant field value if this is a `FALSE` setting.

30. `qFocussing` is set to `TRUE` when beam focussing is applied, otherwise its `FALSE`.

31. `qMatchedBeam` is a logical flag. When the emittance is non-zero, `sEmit_n`$\neq$ 0, a matched beam condition is applied to the transverse electron variables, `sSigmaElectrons`.

The final section of this chapter now discusses how the 3D model operates using parallel architecture machines. The full simulation codes written in Fortran 95 can be found in a CD-ROM which is attached in this thesis in an envelope.

2.7.2 Outline of the three dimensional simulation code

A flow chart is shown in figure 2.18 giving the structure of the 3D simulation code. A detailed description of each part is listed below;

- Begin from `Main.f90` where all the initial parameters on parallel processing, integration size, electron beam information, initial radiation field setup and FEL fundamental parameters are read in from an input file called `Run1.in`.

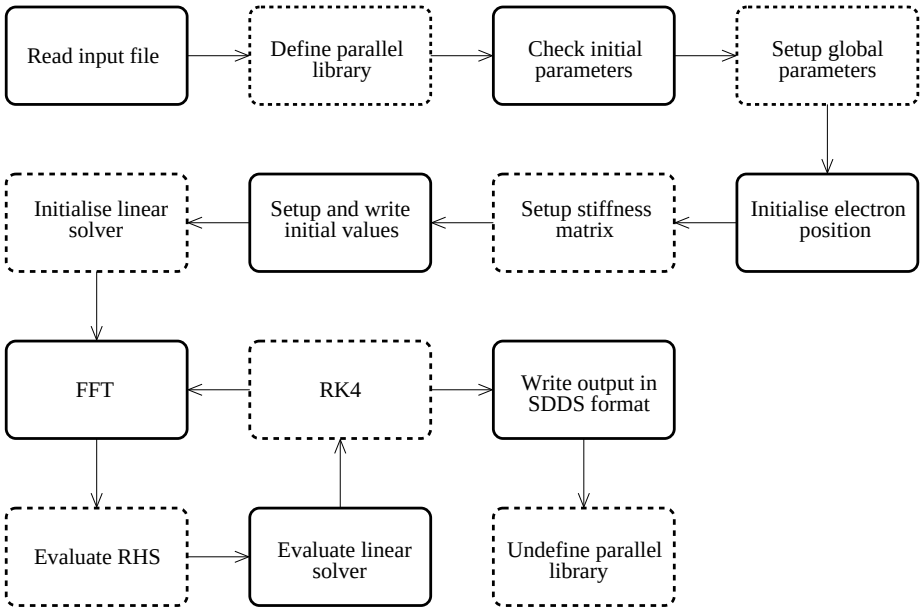

Figure 2.18: The flow chart in this diagram shows a summary of how the 3D simulation code operates.

- This 3D simulation code is written to run on parallel processing machines, therefore initialisation of parallel library information is required by NAG. The routines used to define the parallel libraries are from NAG libraries and specific input parameters are manditory. This step is executed at the start of `FEMethod.f90`.

- Continue in `FEMethod.f90` all the initial parameters must be checked for invalid values. For example, the integration step size must be smaller than the element size in $\bar{z}_2$ to ensure that there are enough integration steps within one $\bar{z}_2$ step, otherwise the solution will be invalid.

- Defining global parameters in the next step. Some of the parameters such as ε required to be computed and are dependent on a_w and γ_r. Also, the number of nodes in each of the three space dimensions are stored as global variable names accessible anywhere within the code.

- The initialisation process of the electron beam. If shot-noise is present then their phase-space position will be adjusted according to their statistical properties. The weighting function $\bar{\chi}$ is calculated at this point (an explanation on how $\bar{\chi}$ is derived in appendix C).

- In section 2.6.4, the stiffness matrix was introduced in the Galerkin Method displayed in equation 2.176 for one hexahedral element. When the system is

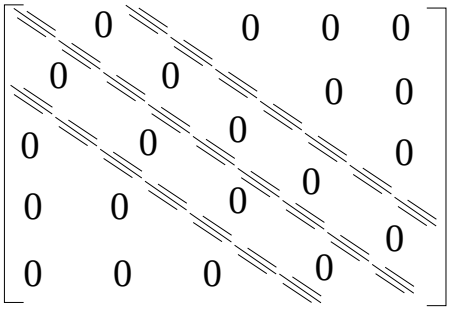

Figure 2.19: The structure of the stiffness matrix. Nonzero entries are present in the tri-band diagonal and zero everywhere else.

larger than using many more elements in 3D space, the size of this stiffness matrix increases. Each node of the whole system has its own global number and this is where the transformation of a 3D system into a 2D matrix takes place. A tri-band diagonal matrix is formed for a large system. Figure 2.19 shown the form of the whole stiffness matrix.

- After the setup of all the parameters, calculated variables, electron beam and radiation field matrix, the information is stored in files before any interaction takes place. These data are stored in SDDS format and it can be written as ASCII or in binary.

- The last step before the integration of all the equations. It is to initialize the NAG linear solver routines. This involves choosing which method to use depending on the pattern of the stiffness matrix. The data is distributed over the parallel processors.

- The first part of the SSFM discussed in section 2.6.3 involves using the NAG version of FFT. The procedure of the FFT and the multiplication of the exponential term is carried out. This is the start of integration process.

- The r.h.s. of the wave equation is the electron source term is evaluated after FFT step. The r.h.s. terms on the electrons' equations are calculated.

- All the variables in the Maxwell-Lorentz equations have been calculated and the process of the linear solver is to take the inverse of the stiffness matrix to the r.h.s. of the wave equation.

- The Runge-Kutta fourth order is used to integrate all the equations and an solution is evaluated. This solution is used as the initial condition for the next integration step. The integration process repeated from FFT to this step until the end of the propagation length, $\bar{z}$.

- The output data at every N^{th} step is stored into files, this is similar step when saving the initial data.

- To undefine the parallel libraries is the final step of this simulation code. This is an important step, otherwise the simulation run will not be ended correctly.

The theories of the 3D model and the FEL equations has been presented and derived in this chapter. The results in the 1D model have been reproduced using the 3D model are discussed in the next chapter.

Chapter 3

The 3D model in the 1D limit

In the previous chapter, the mathematics of the one- and three-dimensional systems were derived. The main difference between the two systems is the extra transverse derivative terms which are displayed in the 3D wave equation 2.84. The focussing term in the 3D electrons' transverse equation is another difference compared to the similar 1D equations.

To show that the FEL equations derived and the equations has been solved correctly using the numerical methods, previously published 1D results may be reproduced using the 3D model. An introduction to the elements used in the 3D system and the electron initialisation is discussed before examining the reproduced 1D results. The four instances that has been reproduced firstly simulate the effects of Coherent Spontaneous Emission before the FEL interaction is included. The effects of shot-noise in the electron beam are also examined. Finally the model is used to simulate the effects of electron energy spread, shot-noise and includes FEL interaction.

3.1 The element

It is important to choose an appropriate element before application of the numerical method to the FEL equations and it is now discussed.

In section 2.5.1, the numerical method used in the 1D FEL model that used electron pulse was the Streamline Diffusion method and the Galerkin method was applied in the 3D model. A sketch of the 3D element used is shown in figure 2.13.

Figure 2.13 shows the 3D elements that has eight nodes. A third order interpolation function was used in the 1D model and in the 3D model the linear interpolation function was used. To reduce error, a greater number of linear elements are required for the 3D case.

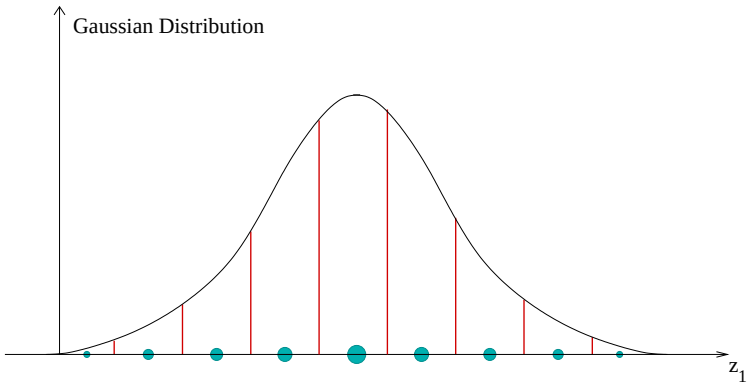

Figure 3.1: In a Gaussian distribution the macroparticles are uniformly spaced. Their charge weight are different with the largest χ factor in the centre of the distribution.

In section 2.6.4, discussion on how the field is discretised in $\bar{x}$, $\bar{y}$ and $\bar{z}_2$ was explained with each node representing by a value of the field. In calculating the r.h.s. of the wave equation the interpolation function allocates the electron contribution to the field between the nodes. When an electron emits radiation inside an element, its contribution is "shared" among the nodes as illustrated in figure 2.13 with the interpolation function determining the proportion of the source each node would receive.

The next section describes the initialisation of the macroparticles in each of the phase-space directions.

3.2 Macroparticle initialisation

When the field equation was derived in the previous chapter, in the second part of the SSFM, a summation over real electrons was changed to sum over a fewer number of macroparticles. Therefore the term 'macroparticles' are used to describe the initialisation of electron variables in this section.

In the 1D electron pulse model, the macroparticles were initially evenly spaced within the electron pulse in $\bar{z}_1$ with a Gaussian distribution in the weighting factor χ. In figure 3.1, the macroparticles are uniformly spaced along $\bar{z}_1$ and the macroparticle with the largest χ value is located in the centre of the electron beam, whereas those at the ends have smaller χ. The macroparticles at the edge of the electron beam have a smaller χ value, and therefore represent fewer real electrons. The effect of these macroparticles with smaller χ is therefore weaker.

One option to reduce the number of macroparticles is to set up a different non-uniformly spaced Gaussian grid. Rather than having uniformly spaced macropar-

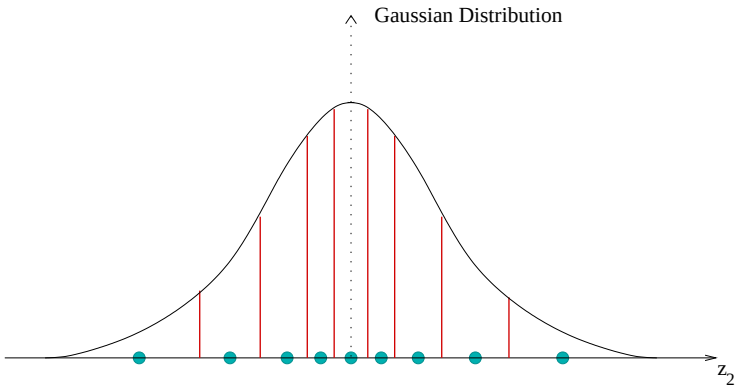

Figure 3.2: The macroparticles have equal charge weight, but the spacing is uneven. There are more macroparticles closer to the centre of the distribution.

ticles, their χ values are chosen approximately equal so that all the macroparticles represent the same number of real electrons. However, their positions are then not equally spaced; see figure 3.2. As a result there are fewer macroparticles at the edges of the beam with more around the centre of the beam.

The discussion on how the macroparticles are initialised is particularly useful for the next section where previous 1D results are reproduced.

3.3 Simulation in the 1D limit

The aim of this section is to show that the 3D simulation code can correctly reproduce the 1D results. During the code development, tests were carried out using the parameters in [18] and [32]. Four different examples show these 1D results can be reproduced. The first 1D model simulates the generation of Coherent Spontaneous Emission using a rectangular profile electron pulse of length $\ell_e = 2$, which is described in the next section.

3.3.1 Coherent Spontaneous Emission (CSE)

A Coherent Spontaneous Emission arises when the current gradient gives a non-uniform electron distribution over a radiation wavelength. A rectangular (or top-hat) current profile of the electron beam is used, the length of the electron pulse in $\bar{z}_2$ direction is $\ell_e = 2$. The initialisation of the electron beam and the elements in the 3D model are discussed below in order to reproduce CSE effects. First, a table of the parameters used are listed in table 3.1.

From table 3.1, the charge of the electron pulse is 1nC therefore there are approximately 6.24×10^9 real electrons and this value is the `i_RealE` in the input

Electron beam parameters		
Bunch Charge	Q_e	1 nC
Resonant electron energy	γ_r	100
Length of pulse in $\bar{z}_2$	ℓ_e	2
Distribution of electron beam in $\bar{z}_2$		Top-hat
Shot-noise		No
Undulator parameters		
Undulator Type		Helical
Pierce parameter	ρ	0.01
Undulator deflection parameter	a_w	2
Propagation distance	$\bar{z}$	1

Table 3.1: Parameters for 1D CSE.

file. For this model the effects of shot-noise were not included, therefore `q_noise` is set to "FALSE" in the input file. The value of ρ, ℓ_e and the propagation distance are taken from [32].

The number of macroparticles used and the number of elements required in the transverse plane is one. These are the 1D-limits to be set in the 3D model in order to re-produce any 1D results. There are more 1D-limits but they will be discussed as appropriate in the chapter.

In this simulation, there is no FEL interaction between the radiation and the electrons therefore the coupling terms in the electrons' equation were zero by setting the logical flag of `qElectronFieldCoupling` to "FALSE" in the input file.

In section 3.2, the electrons' initialisation was discussed, so either a uniform or Gaussian grid could be used in the transverse direction since only one macroparticle is required. A uniform grid was used to setup the macroparticles in the $\bar{z}_2$ direction. There were 25 elements per radiation period (range of $\bar{z}_2$ of $4\pi\rho$) and 5 macroparticles per element; therefore, there exist approximately 16 radiation period and 2000 macroparticles in the electron pulse. Since only one element is used in the transverse plane, the coupling of the macroparticles to each node is computed via the interpolation function.

The results produced by the 3D simulation code are plotted in figure 3.3. At $\bar{z} = 0$, the head of the electron beam is at $\bar{z}_2 = 0$ and the tail is at $\bar{z}_2 = \ell_e$. The scaled power is calculated by integrating $|A|^2$ across the transverse plane and the results plotted in figure 3.3. The macroparticles (in red) have propagated to between $1 < \bar{z}_2 < 3$ corresponding to $0 < \bar{z}_1 < 2$ in $\bar{z}_1$ frame of [32]. As the electron pulse propagates along the undulator without the FEL interaction,

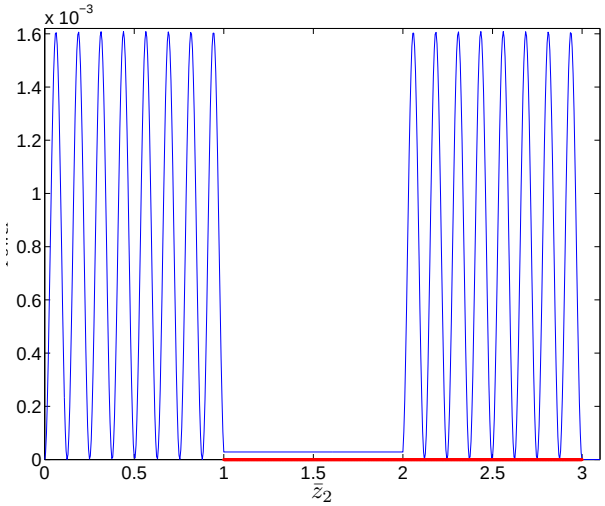

Figure 3.3: The scaled power of the CSE model plotted as a function of $\bar{z}_2$ when $\bar{z} = 1$ (approx. eight undulator periods). A rectangular electron pulse current profile of length $\ell_e = 2$ is used and shown in red.

radiation pulses are emitted at both ends with a duration of one radiation cycle. The macroparticles were uniformly spaced within the electron pulse (in $\bar{z}_2$) and their χ_j factors were equal. Over a radiation period in the middle of the pulse, the macroparticles emit in phase and constructive interference occurs. At the edge of the electron pulse the radiation emitted acts as a strong seed field since the current gradient of the electron pulse is discontinuous. The macroparticles existed in half of the radiation period and the other half was empty after $\bar{z} = 2\pi\rho$. The sum of the macroparticles' to the bunching parameter is therefore non-zero and radiation pulses develop at the pulse edges. From the CSE theory, the oscillatory amplitude of $|A|^2 \simeq 16\rho^2$ of figure 3.3 and agrees well with simulations of [32] at $\bar{z}_2 = 1$.

Another 1D limit is the electron beam radius must be significantly larger than the orbital radius in the transverse plane. The positions of macroparticles do not change very much and remain close to their initial values as the interaction distance $\bar{z} = 1$ is small; hence the numerical solution approximates the analytical solution given by equation 10 in [32].

A simulation including the FEL interaction is now simulated using a longer electron pulse of $\ell_e = 10$ and with a longer FEL interaction distance.

Electron beam parameters		
Bunch Charge	Q_e	1 nC
Resonant electron energy	γ_r	100
Length of pulse in $\bar{z}_2$	ℓ_e	10
Distribution of electron beam in $\bar{z}_2$		Top-hat
Shot-noise		No
Undulator parameters		
Undulator Type		Helical
Pierce parameter	ρ	0.005
Undulator deflection parameter	a_w	2
Propagation distance	$\bar{z}$	15

Table 3.2: 1D parameters for SACSE with FEL interaction.

3.3.2 Self-Amplified Coherent Spontaneous Emission (SACSE) and Coupling

SACSE occurs when the radiation pulse emitted as CSE acts as a strong seed and this supperadiant pulse grows rapidly when the propagation distance is longer than the electron pulse. The previous simulation of the FEL interaction did not include FEL coupling. Here the interaction between the radiation and the electrons is present.

A longer rectangular current profile, $\ell_e = 10$ is used with propagation further along the undulator to $\bar{z} = 15$. The parameters used are shown in table 3.2.

Same electron charge was used therefore the number of real electrons is the same as the model in the previous section, $\approx 6.24 \times 10^9$. Shot-noise was not included in the electron beam. The parameter $\rho = 0.005$ and there are approximately 160 radiation periods in the electron pulse. The number of macroparticles is 6000 in the $\bar{z}_2$ direction with one macroparticle in the transverse direction. According to the 1D-limits, one element and a uniform distribution for the electron beam was used in the transverse plane. The FEL coupling terms in the electrons' equation is switched on by setting the logical flag `qElectronFieldCoupling` to "TRUE".

The integrated $|A|^2$ plots (the scaled power) are shown in figure 3.4 and there are four separate plots showing the evolution of the radiation and the macroparticles (in red) propagating in $\bar{z}_2$ from $0 < \bar{z}_2 < 10$ to $15 < \bar{z}_2 < 25$. In figure 3.4(a) the macroparticles have propagated approximately 10 undulator periods and the radiation emitted is CSE. This is similar to the results of the previous section-pulses of radiation were emitted at the edges of the electron pulse due to the

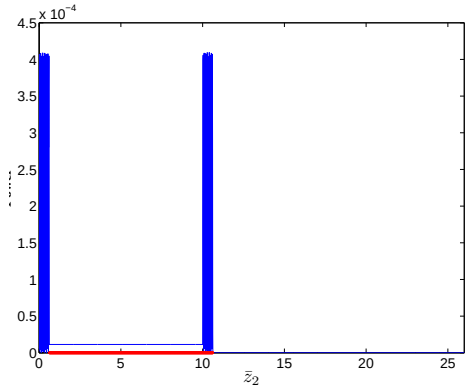

(a) $\bar{z} = 0.625$, approx. 10 undulator periods

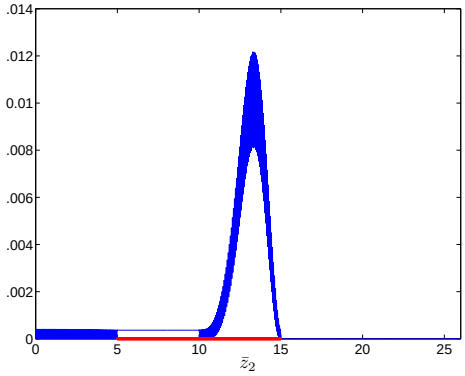

(b) $\bar{z} = 5$

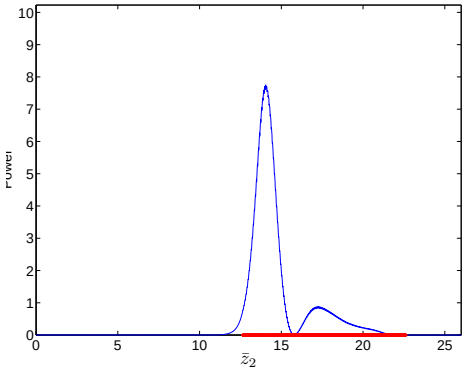

(c) $\bar{z} = 12.625$, approx. 200 undulator periods

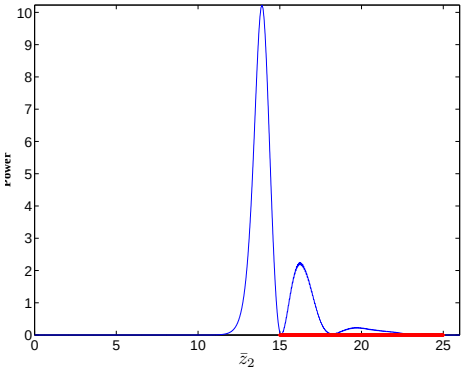

(d) $\bar{z} = 15$

Figure 3.4: The evolution of the power plots for a rectangular electron pulse is shown in four different plots. The electron pulse (in red), of length $\ell_e = 10$, interacts with the radiation field and for an interaction distance of $\bar{z} = 15$. Note the different y-axis ranges.

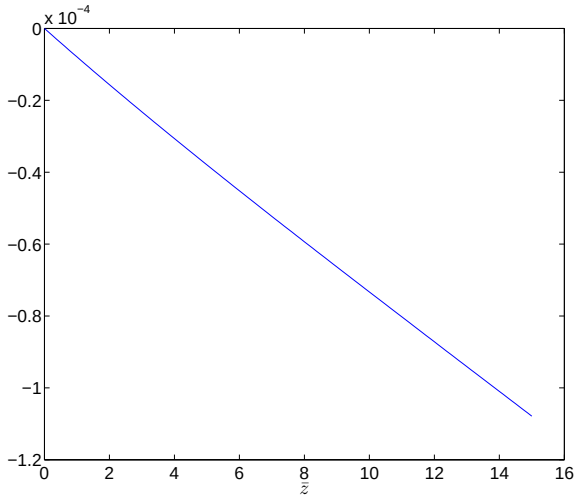

Figure 3.5: An $\ell_e = 10$ electron pulse has propagated to $\bar{z} = 15$. The energy conservation between radiation and electrons is plotted as a function of $\bar{z}$. It has a small relative error of 10^{-4}.

large electron current gradient. At $\bar{z} = 5$ figure 3.4(b) the radiation in the region $0 < \bar{z}_2 < 5$ is in vacuum. The steady-state region exist in the region $5 < \bar{z}_2 < 10$. The radiation in the slippage region, $10 < \bar{z}_2 < 15$, acts as a strong seed field and it began to grow as shown in figure 3.4(b). After the macroparticles have propagated approximately 200 undulator periods, the radiation has been amplified further, see figure 3.4(c), from $\bar{z} = 5$ and there is no steady-state region i.e. the propagation distance is greater than ℓ_e. At $\bar{z} = 15$, in figure 3.4(d), the radiation has grown exponentially and saturation was reached. The electron pulse lies between 15 and 25; any radiation on the left of the electron pulse, $\bar{z}_2 < 10$, has propagated into free space and no longer interacts with the macroparticles. The non-linear evolution of SACSE has been demonstrated in this simulation and figure 2 of [32] has been reproduced in figure 3.4(d) using the 3D model.

One way to show that the 3D model has been solving the FEL equations correctly is to check the constant of motion, i.e. that energy is conserved between the radiation and electrons. The equation for the constant of motion was derived in previous chapter in equation 2.302.

The constant of motion is calculated numerically and plotted against $\bar{z}$ as shown in figure 3.5. The constant agrees to within a fractional 10^{-4} of its original value, a result that is considered good.

In section 2.3.3, discussion on the electrons bunching mechanism was given and the bunching parameter for 1D model was defined in section 2.4.1. In a 3D

model, the bunching parameter is defined as:

$$b(\bar{z}_2) = \frac{1}{V_{ep}} \sum_{j=1}^{N} \chi_j \exp\left\{\frac{i\bar{z}_2}{2\rho}\right\} \tag{3.1}$$

where V_{ep} is the scaled volume of the electron pulse. In the 3D model, the bunching was calculated over two radiation periods. For example, for macroparticles within a region $0 < \bar{z}_2 < 8\pi\rho$, $b_1(\bar{z}_2)$ is calculated as:

$$b_1(0 < \bar{z}_2 < 8\pi\rho) = \frac{1}{Le_{\bar{x}}\ Le_{\bar{y}}\ 8\pi\rho} \sum_{j=1}^{N} \chi_j \exp\left\{\frac{i\bar{z}_2}{2\rho}\right\} \tag{3.2}$$

where $Le_{\bar{x}}$ and $Le_{\bar{y}}$ is the length of the electron pulse in $\bar{x}$ and $\bar{y}$ direction respectively. The bunching parameters are calculated in this model and four figure are plotted with the same $\bar{z}$ values as figure 3.4.

After 10 undulator periods, the value of $|b|$ is seen to be small in figure 3.6(a). In figure 3.6(b) $|b|$ begins to increase at the tail of the electron pulse, causing the radiation to grow, see figure 3.4(b). At $\bar{z} = 12.5625$ figure 3.6(c) through to $\bar{z} = 15$ figure 3.6(d) the radiation is amplified exponentially the macroparticles were emitting in phase. The bunching $|b|$ is close to the maximum of unity within this interval indicating saturated behaviour.

The effects of FEL interaction has been demonstrated in this model using a top-hat current profile electron pulse and in the next section, a Gaussian current profile is used with shot-noise but without the FEL interaction.

3.3.3 CSE and Shot-noise

In both of the models discussed previously, the current profile of the electron pulse was a top-hat distribution. A less extreme Gaussian distribution in the $\bar{z}_2$ direction is used in the simulation of this section. The transverse coordinates of the macroparticles in the previous simulations were the same for all $\bar{z}_2$ as there was no shot-noise in the electron beam. In this section electron shot-noise is included using the method of [18] so that the macroparticles' phase-space positions and charge weight will be randomly varied about the mean uniformly distributed values.

The parameters used to model a Gaussian profile electron beam with shot-noise are listed in table 3.3 and the analysis is described below. Most of the parameters used were obtained from [18]. The same electron charge, 1nC was used, but the electron beam has a Gaussian distribution with $\sigma_{\bar{z}_2} = 3$, so the

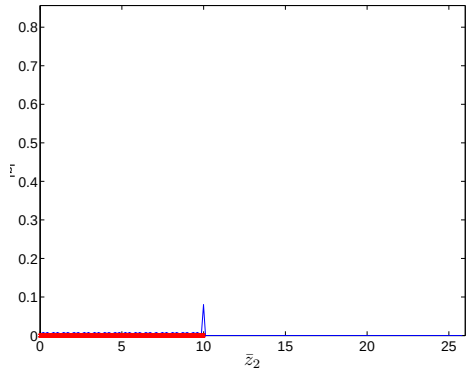

(a) $\bar{z} = 0.625$, approx. 10 undulator periods

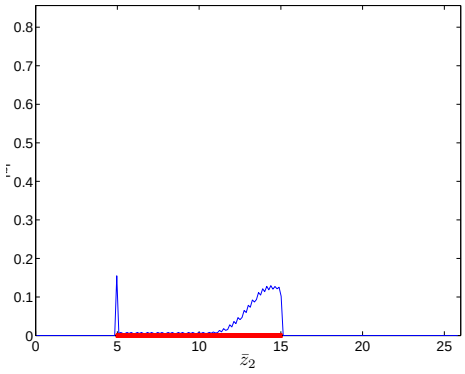

(b) $\bar{z} = 5$

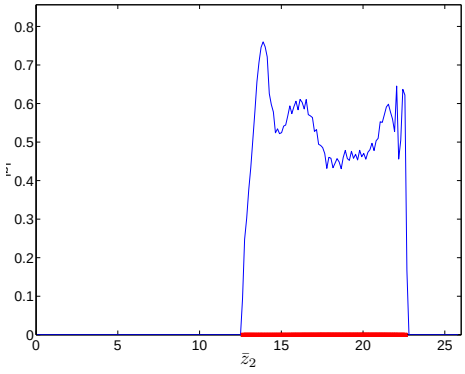

(c) $\bar{z} = 12.625$, approx. 200 undulator periods

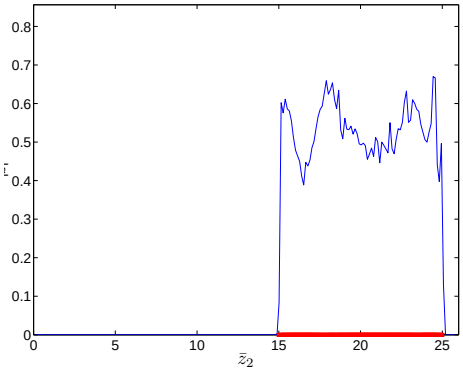

(d) $\bar{z} = 15$

Figure 3.6: The bunching parameter is close to zero at $\bar{z} = 0$ across the electron pulse, of length $\bar{z}_2 = 10$, and begins to increase at the tail of an electron pulse at $\bar{z} = 5$. At $\bar{z} = 12.625$ and $\bar{z} = 15$, the bunching parameter indicates that the macroparticles have bunched across the electron pulse. The red line indicates position of the electron pulse.

Electron beam parameters		
Bunch Charge	Q_e	1 nC
Resonant electron energy	γ_r	100
Length of pulse in $\bar{z}_2$	ℓ_e	18
Sigma in $\bar{z}_2$	$\sigma_{\bar{z}_2}$	3
Distribution of electron beam in $\bar{z}_2$		Gaussian
Shot-noise		Yes
Undulator parameters		
Undulator Type		Helical
Pierce parameter	ρ	$\frac{1}{40\pi}$
Undulator deflection parameter	a_w	2
Propagation distance	$\bar{z}$	2

Table 3.3: 1D CSE & Shot-noise parameters.

range of the electron pulse in $\bar{z}_2$ is $0 < \bar{z}_2 < 18$. The full range of 6 sigma accounts for 99.7% of a Gaussian distribution. The logical flag `q_noise` is set to "TRUE" in the input file. As there is no FEL interaction between the radiation and electrons, `qElectronFieldCoupling` is set to "FALSE".

The ρ parameter is $1/40\pi \approx 7.96 \times 10^{-3}$, so one radiation period is 0.1 in units of $\bar{z}_2$. There are 180 radiation period in the electron pulse. In the transverse plane, one element and a top-hat distribution of macroparticles was used. The initialisation of the macroparticles is discussed next. The macroparticles' phase-space positions deviate from their mean value when shot-noise is present. The weighting function is calculated according to the macroscopic Gaussian current distribution and a charge weight noise added.

The results produced are presented and the analysis of the results are discussed as follows. Figure 3.7 shows the coordinates of the macroparticles' in the transverse plane at $\bar{z} = 0$. The mean initial transverse position is $(\bar{x}, \bar{y}) = (0.00, 0.02)$. The particles orbit around the origin $(\bar{x}, \bar{y}) = (0, 0)$ as they propagate along the undulator. The macroparticles are now positioned in the transverse plane and in the $\bar{z}_2$ direction according to [18].

Figure 3.8 shows the scaled power plotted as a function of $\bar{z}_2$.

A Gaussian distributed electron pulse of $\ell_e = 18$ was propagated to $\bar{z} = 2$ and the evolution of the radiation is shown in figure 3.8. At $\bar{z} = 2$ the electron pulse has propagated to $2 < \bar{z}_2 < 20$. The electron pulse has a standard deviation of 3 and in general the radiation does not evolve in the steady-state; this is in contrast to a rectangular electron pulse in previous examples. The only region that evolves close to the steady-state is around the peak of the electron current,

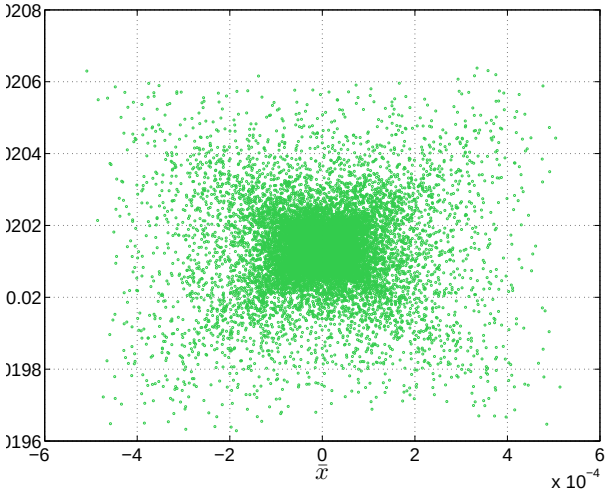

Figure 3.7: At $\bar{z} = 0$, with the effects of shot-noise in the electron beam, the macroparticles are positioned using the shot-noise algorithm in the transverse plane around the mean value of $(0.00, 0.02)$.

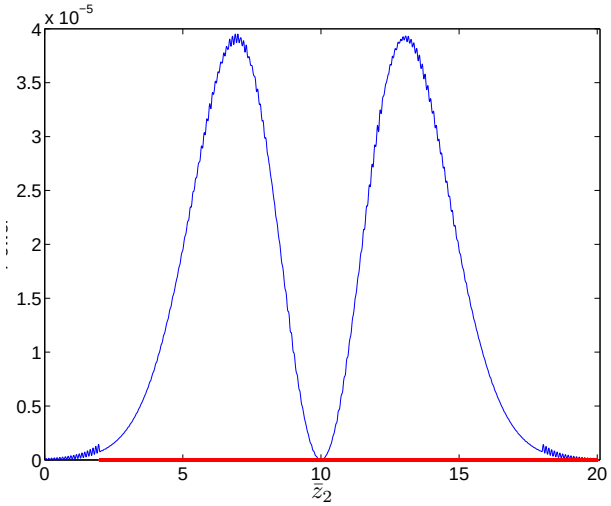

Figure 3.8: The scaled power generated by a Gaussian current electron beam, of length $\ell_e = 18$, with shot-noise plotted against $\bar{z}_2$. The effects of CSE is shown with shot-noise in the electron pulse. The red line indicates position of the electron pulse at $\bar{z} = 2$.

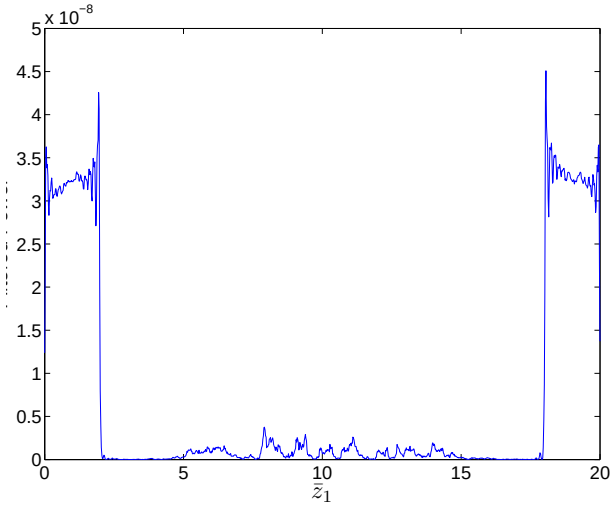

Figure 3.9: The high frequency band pass filtered power, $|A|^2$, is plotted as a function of $\bar{z}_1$ for a Gaussian profile electron pulse of length $\ell_e = 18$. The spontaneous emission is visible (centre) in this filtered plot.

where the current gradient is zero and so the CSE effects become negligible. When the current gradient is large, more CSE is generated as seen around $\bar{z}_2 = 7$ and $\bar{z}_2 = 13$.

The effects of shot-noise are more clearly shown in figure 3.9 by Fourier filtering the scaled field using one of the SDDS tool kit function SDDSFILTER. This filters out the strong, lower frequency components of the CSE which dominate the power of figure 3.8. In [18] it was shown that when $\sigma_{\bar{z}_2} > 2\rho\sqrt{\ln(\bar{N})}$, where $\bar{N}$ is the expectation of the total number of electrons in the pulse using a Poisson distribution, shot-noise should dominate CSE at the resonant wavelength for the Gaussian case. This is clearly seen from the filtered case of figure 3.9.

Again, the figures in 3.8 and 3.9 agree well with the figure 7 and 8 in [18] for a Gaussian electron pulse with shot-noise.

In the last section of this chapter, a simulation using a top-hat profile electron pulse with shot-noise, energy spread and the FEL interaction is presented.

3.3.4 SACSE, Energy spread and Coupling

The simulation of this section demonstrates the properties from the previous models and introduces energy spread effects to the electron pulse. The FEL interaction between the radiation and the electrons is included. The initialisation of the system is first described before the results produced using the 3D simulation are shown.

Electron beam parameters		
Bunch Charge	Q_e	1 nC
Resonant electron energy	γ_r	100
Length of pulse in $\bar{z}_2$	ℓ_e	6
Distribution of electron beam in $\bar{z}_2$		Top-hat
Shot-noise		Yes
Energy spread	σ_p	0.5
Distribution of energy spread		Gaussian
Undulator parameters		
Undulator Type		Helical
Pierce parameter	ρ	$\frac{1}{40\pi}$
Undulator deflection parameter	a_w	2
Propagation distance	$\bar{z}$	5

Table 3.4: Parameters for SACSE, energy spread and coupling.

A rectangular current profile electron beam of length $\ell_e = 6$ with an energy spread is propagated to $\bar{z} = 5$. Most of the parameters are taken from [18] a summary of which are listed in table 3.4.

The length of the electron pulse in $\bar{z}_2$ is $\ell_e = 6$ and there are 60 radiation periods. There is one element and one macroparticle in the transverse plane and the size of the electron beam in the transverse plane is chosen to be greater than the orbital radius,the 1D-limit. The radiation and the electrons interact over five gain lengths, $\bar{z} = 5$.

From table 3.4, the electron charge is 1nC and the Gaussian energy spread, σ_p, of 0.5, this is a 1D parameter. The relative energy spread, $\dfrac{\Delta_\gamma}{\gamma}$, may be described as a spread in the 1D energy parameter p.

$$\sigma_p = \frac{1}{\rho}\frac{\Delta_\gamma}{\gamma} \tag{3.3}$$

The Gaussian energy spread, σ_p, maybe converted into a 3D quantity using the following relation:

$$\bar{p}_{\bar{z}_{2j}} = 1 - 2\rho p_j \tag{3.4}$$

The full range of the energy spread in the Gaussian distribution is then:

$$-3\sigma_{p_j} < p_j < 3\sigma_{p_j} \tag{3.5}$$

$$-1.5 < p_j < 1.5 \tag{3.6}$$

which when converted in terms of $\bar{p}_{\bar{z}_{2j}}$,

$$0.976 < \bar{p}_{\bar{z}_{2j}} < 1.024 \tag{3.7}$$

The standard deviation of the electron beam in $\bar{p}_{\bar{z}_2}$ is approximately 0.008. The range is six times the standard deviation for the Gaussian distribution. In the 1D system all the macroparticles are in resonance at the beginning with $p_{j0} = 0$ (assuming there is no energy spread). Therefore the initial value for $\bar{p}_{\bar{z}_2}$ is 1, from equation 3.4; only one macroparticle was used to represent this scaled phase direction in all previous simulations. With energy spread included there must be at least three macroparticles in $\bar{p}_{\bar{z}_2}$ to ensure a quasi-Gaussian distribution function can be formed. With 60 radiation periods in the electron pulse of $\ell_e = 6$, 21 macroparticles were used in $\bar{p}_{\bar{z}_2}$ per radiation period and 50400 macroparticles used in the 60 periods.

The effects of shot-noise was present in the electron beam, so the macroparticles phase-space coordinates had deviates from their mean value with respect to their χ_j. The same algorithm described in section 3.3.3 was used to calculate the coordinates.

The bunching parameter as defined in equation 3.1, was calculated for an ensemble of 180 distributions and the analytical statistics of the bunching [33] compared with the results of the ensemble. The following are the analytical bunching relations for a real electron distribution [33]:

$$\begin{aligned} b_{\text{rms}} &= \sqrt{\langle |b|^2 \rangle} &&\approx \frac{1}{\sqrt{\bar{N}_\lambda}} \\ \bar{b} &= \langle |b| \rangle &&\approx \sqrt{\frac{\pi}{4\bar{N}_\lambda}} \\ \sigma_{|b|} &= \sqrt{\langle (b - \bar{b})^2 \rangle} &&\approx \sqrt{\frac{1 - \frac{\pi}{4}}{\bar{N}_\lambda}} \end{aligned} \tag{3.8}$$

where $\bar{N}_\lambda = 1.04 \times 10^7$ is the expectation of the number of electrons in a radiation period. The following statistics for the ensemble were calculated and compared to the analytical results of 3.8:

$$\begin{array}{lll} & \text{Numerical} & \text{Analytical} \\ b_{\text{rms}} & \approx 3.05 \times 10^{-4} & \approx 3.10 \times 10^{-4} \\ \bar{b} & \approx 2.71 \times 10^{-4} & \approx 2.75 \times 10^{-4} \\ \sigma_{|b|} & \approx 1.40 \times 10^{-4} & \approx 1.44 \times 10^{-4} \end{array} \tag{3.9}$$

The bunching statistics are seen to be in good agreement with the analysis demon-

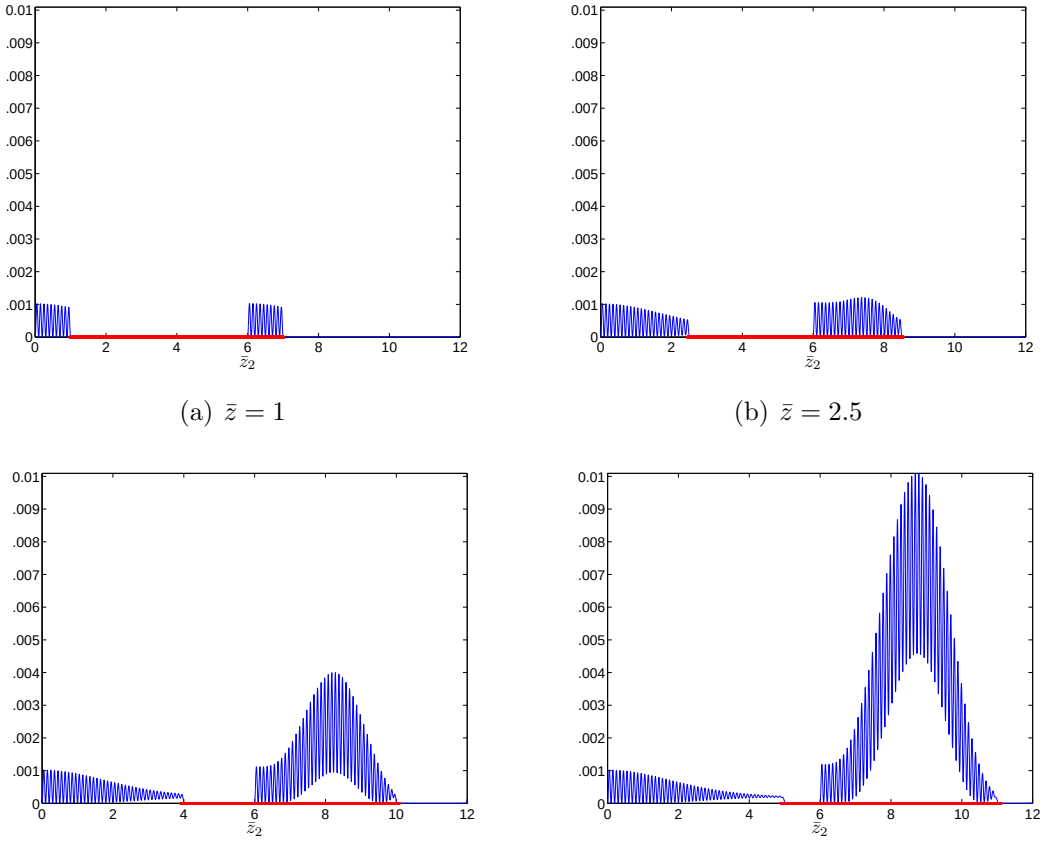

(a) $\bar{z} = 1$ (b) $\bar{z} = 2.5$

(c) $\bar{z} = 4$ (d) $\bar{z} = 5$

Figure 3.10: A top-hat electron pulse of length $\ell_e = 6$ has an energy spread of $\sigma_P = 0.5$ and includes shot-noise. The effects of the FEL interaction are included. The evolution of the power of the radiation is plotted as a function of $\bar{z}_2$ and is shown at various $\bar{z}$. The effects of SACSE are observed.

strating that the macroparticles distribution models shot-noise well.

The integrated $|A|^2$, the scaled power, is plotted in figure 3.10 as a function of $\bar{z}$ and the macroparticles plotted in red. After one gain length, $\bar{z} = 1$, the initial CSE dominates as observed in figure 3.10(a). At $\bar{z} = 2.5$, the radiation to the left of the electron pulse ($\bar{z}_2 = 2.5$) propagates in free space. Notice the amplitude of the CSE radiation is gradually decreasing and the radiation towards the tail of the electron pulse begins to experience exponential gain, these effects are shown in figure 3.10(b). At $\bar{z} = 4$, the exponential gain has amplified the CSE, this is clearly shown in figure 3.10(c), and the amplitude of the radiation in the vacuum region, $0 < \bar{z}_2 < 4$, continues to decrease gradually. At $\bar{z} = 5$, the propagation distance is smaller than the length of the electron pulse, $\bar{z} = 5 < \ell_e(\bar{z}_2) = 6$, so there is a region, $5 < \bar{z}_2 < 6$, within the pulse still evolving as in the steady-state

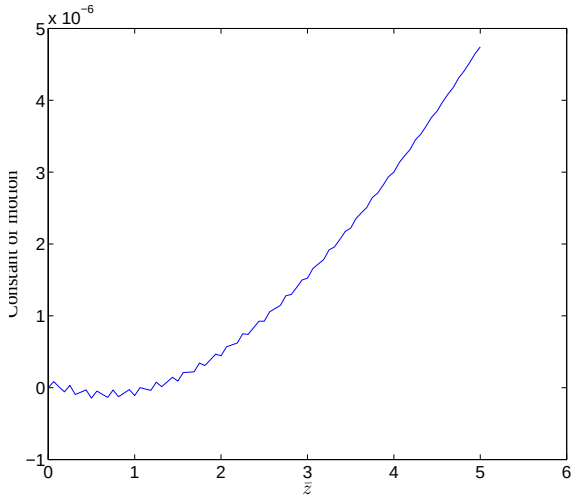

Figure 3.11: A Gaussian electron pulse of length $\ell_e = 6$ with shot-noise and energy spread has propagated to $\bar{z} = 5$. The energy conservation between radiation and electrons is plotted as a function of $\bar{z}$. It has a relative error of 10^{-6}.

regime, see figure 3.10(d). The CSE in the slippage region has been amplified further as the macroparticles interact with the radiation.

The spread in $\bar{p}_{\bar{z}_2}$ in the electron pulse causes a gradual reduction in amplitude of the CSE emitted in the vacuum region as the hard edge of the electron pulse is "blured" due to electron dispersion shown in figures 3.10(a) to 3.10(d). Again, this result are in good agreement with figure 4 of [18].

Finally the constant of motion is shown in figure 3.11 plotted against $\bar{z}$ with a relative error of $< 10^{-5}$ indicating that the energy conservation between the radiation and the electrons is good and that the 3D model solves this system correctly.

In the next chapter, 3D results are presented including the effects of diffraction on the transverse plane, a matched electron beam is used and all the properties modeled in this chapter are included.

Chapter 4

Analysis and results from the New 3D FEL

The results in chapter 3 have shown that one may reproduce 1D results of CSE, CSE with FEL interaction, CSE with shot-noise and CSE, Shot-noise, FEL interaction and energy spread using the 3D simulation code by applying appropriate 1D-limits. The effects of CSE generation and amplification were shown, which are not possible to model in other 3D codes as their model equations have been averaged over a radiation period. The results shown in this chapter include the effects of radiation diffraction in the transverse plane, electron beam emittance and focussing, as these may only be studied in three dimensions. The four sets of results simulated in this chapter are:

- diffraction only;
- matched electron beam with focussing and shot-noise but no FEL interaction;
- matched electron beam with focussing and shot-noise with FEL interaction but no diffraction;
- a full 3D model that simulates the effects of diffraction, shot-noise, FEL interaction, energy spread and matched beam with focussing.

Most of the electron and undulator parameters such as electron emittance, energy spread, and ρ were values used in section 4.2– 4.4 are the same so the similar figures may be compared and analysed.

4.1 Diffraction

The first result presented in this section relates to the effects of diffraction in the transverse plane. In chapter 3, 1D results were reproduced when 1D-limits were applied to the simulation code. One of the limits used only one element in the transverse plane with the radiation assumed as a plane wave.

The parameters used in this section test whether the 3D code simulates the effects of diffraction correctly according to theory. They are not specific to any system and are used simply to test the algorithms modelling the effects of diffraction. There is an option in the input file to use a transverse Gaussian seed field by setting the boolean `qInitialGaussField` to "TRUE". This was used initially to model the effects of diffraction using the parameters listed in table 4.1. The

Electron beam parameters		
Resonant electron energy	γ_r	100
Sigma in $\bar{x}$		0.4
Sigma in $\bar{y}$		0.4
Sigma in $\bar{z}_2$		0.4
Distribution of electron beam in $\bar{x}$		Gaussian
Distribution of electron beam in $\bar{y}$		Gaussian
Distribution of electron beam in $\bar{z}_2$		Gaussian
Number of macroparticles in $\bar{x}$		6
Number of macroparticles in $\bar{y}$		6
Number of macroparticles in $\bar{z}_2$		6
Shot-noise		No
Seed field parameters		
Sigma in $\bar{x}$		0.4
Sigma in $\bar{y}$		0.4
Sigma in $\bar{z}_2$		0.4
Distribution of electron beam in $\bar{x}$		Gaussian
Distribution of electron beam in $\bar{y}$		Gaussian
Distribution of electron beam in $\bar{z}_2$		Gaussian
Initial field	$\lvert A\rvert$	1
Undulator parameters		
Undulator Type		Helical
Pierce parameter	ρ	$\frac{1}{40\pi}$
Undulator deflection parameter	a_w	2
Propagation distance	$\bar{z}$	≈ 10.053

Table 4.1: Parameters used to model the effects of diffraction only.

standard deviation of the initial Gaussian seed field has the same value as the

standard deviation of the electrons, because, generally, the source of the radiation field is the electrons. The information about the electron beam is not important when testing the diffraction. No FEL interaction was modelled so the logical flags `qElectronFieldCoupling` and the boolean `qElectronsEvolve` were set to "FALSE".

The number of elements used in the transverse plane are 63×63, meaning there are 64×64 nodes, chosen as the system is solved more efficiently using the FFT if the number of nodes used is 2^n [31]. The electron beam was placed in the centre of the transverse plane.

The integration step size and the number of steps to be integrated are set to zero in the input file - in the code these values are then initialised so that the propagation length is one scaled Rayleigh range. In this case the integration step size will become 0.02 and the number of steps will be 503.

Section 2.7.2 mentioned that the initial parameters are checked before the code attempts to solve the equations. One of the checks is that the transverse dimensions must be sufficiently large to accommodate diffraction. If the input value is not sufficient a new value will be calculated using the scaled Rayleigh range and the propagation distance.

The effects of the diffraction of the scaled radiation intensity in the transverse plane are shown in figure 4.1(a)–4.1(d). The scaled intensity, $|A|^2$, at $\bar{z} = 0$ is shown in figure 4.1(a), with figure 4.1(b) plotting $|A|^2$ after one scaled Rayleigh range, $\bar{z} = \bar{z}_R \approx 10.053$. One can see that the peak in $|A|^2$ has decreased from figure 4.1(a) to 4.1(b), also the width of the Gaussian pulse has broadened demonstrating diffraction. The contour view in figures 4.1(c) to 4.1(d) is another useful perspective. The propagation distance here is one scaled Rayleigh length: this may be calculated using equation 2.356, and the analytical beam waist of the radiation field may be calculated using equation 2.341. It can also be measured at $1/e^2$ of the peak intensity. In this case, the waist of the field is

$$\sigma_f = \sigma_{\bar{x}} = 0.4,$$

so the waist of the intensity is

$$w_0 = \sqrt{2}\sigma_f = \sqrt{2} \times 0.4 \simeq 0.5657.$$

The red dashed line in figure 4.2 indicates the width of the distribution at $1/e^2$ of the peak intensity, which agrees with the analytical value calculated. The green line in figure 4.2 is the Gaussian intensity at one scaled Rayleigh range and the

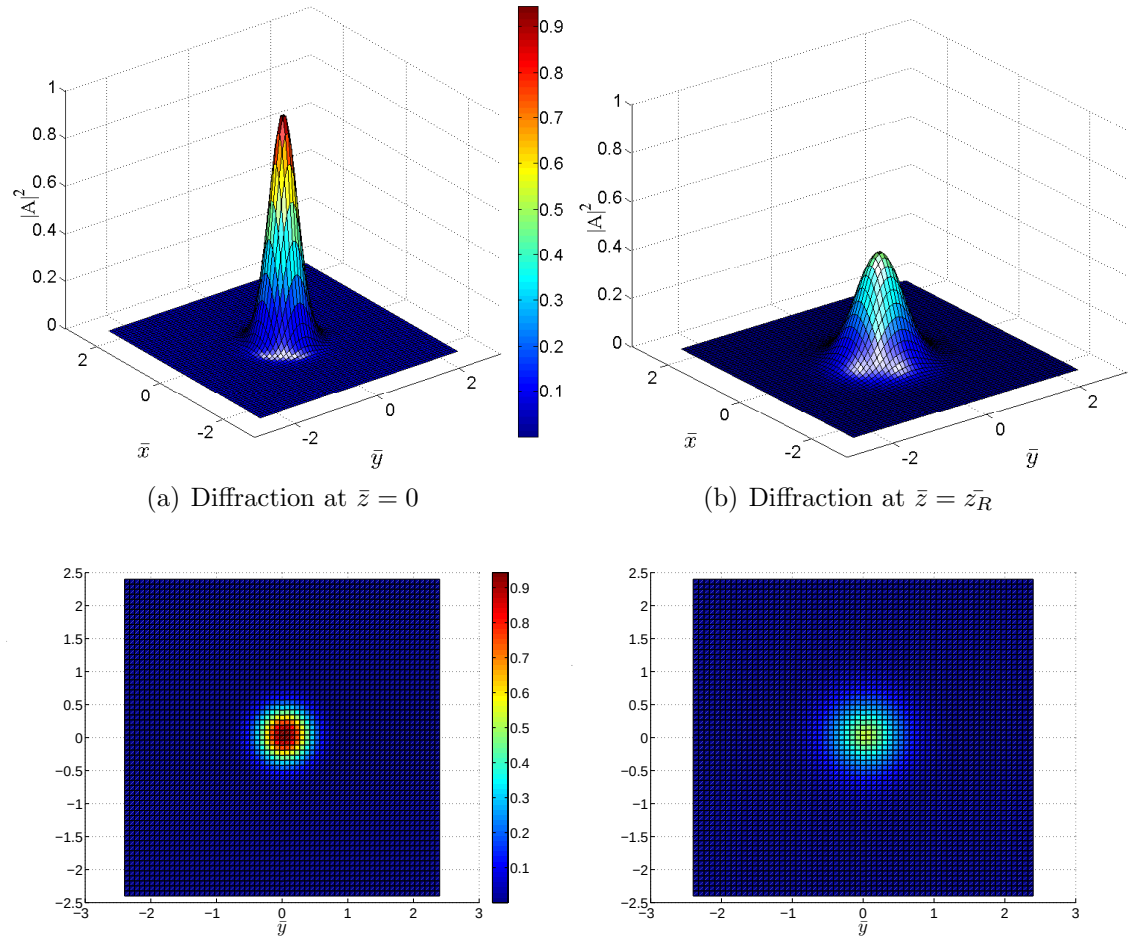

(a) Diffraction at $\bar{z} = 0$

(b) Diffraction at $\bar{z} = z_R$

(c) Diffraction at $\bar{z} = 0$

(d) Diffraction at $\bar{z} = z_R$

Figure 4.1: The effects of radiation diffraction for an initial Gaussian seed field $\sigma_{\bar{x}} = 0.4$ with scaled intensity plotted at $\bar{z} = 0$ in the scaled transverse plane. The peak intensity is reduces and the width broadens after $\bar{z} = z_R$, one Rayleigh range.

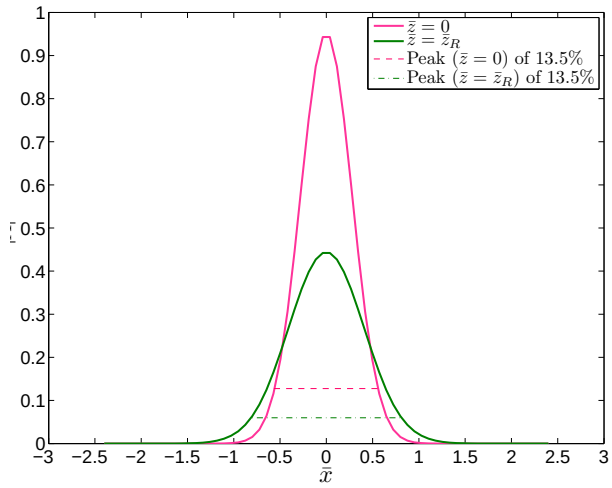

Figure 4.2: A plot showing the beam waist of the radiation at $\bar{z} = 0$ and after one Rayleigh range, $\bar{z} = z_R$. The beam waist is measured at $1/e^2$ of the peak intensity. The beam waist is broader by a factor of $\sqrt{2}$ after one Rayleigh range. The dashed lines indicate the beam waist at the corresponding value of $\bar{z}$.

green dashed line indicates the width of the Gaussian. The σ from the figure at one scaled $\bar{z}_R$ is approximately 0.8, which agrees with the analytical solution given in equation 2.350, thus demonstrating that the code models free-space diffraction correctly.

4.2 Matched Beam with Focussing and shot-noise

In this section, a matched electron beam with shot-noise and natural focussing of the helical undulator is included. This demonstrates that the algorithm for the matched beam functions correctly. The electron beam is said to be matched when the transverse area does not vary as it propagates along the undulator, therefore the transverse radius of beam remains constant. The radius is calculated for a given emittance value. The emittance of the electron beam must satisfy two conditions to ensure a "cold beam" is used.

In previous models, the electron beam was mono-energetic and resonant so there was no energy spread and only one macroparticle could be used in the transverse plane. Here an energy spread is introduced in the electron beam. Given an emittance value, the radius in the transverse plane and the scaled momentum in the transverse plane may be calculated from the theory of matched beam as discussed in section 2.6.10. The results demonstrates the electron beam radius

stays approximately constant when it is matched to the undulator with the undulator focussing term is included in the electrons' momentum equation, as in equation 2.338.

4.2.1 Emittance

When using a beam with a non-zero emittance, the beam should be "matched" to the focussing channel as discussed in section 2.6.10. In addition, the following criteria must be obeyed to ensure that a cold beam is used during the FEL interaction:

1. Emittance of the electron beam must be

$$\epsilon_n < \frac{\gamma_r \lambda_r}{4\pi} \tag{4.1}$$

2. The normalised energy spread, Δ_ϵ, must be much smaller than ρ:

$$\Delta_\epsilon \ll \rho \tag{4.2}$$

where Δ_ϵ is defined as:

$$\Delta_\epsilon = \sqrt{\sigma_\gamma^2 + \sigma_\epsilon^2} \tag{4.3}$$

which consists of the resonant energy spread,

$$\sigma_\gamma = \frac{\Delta\gamma}{\gamma}, \tag{4.4}$$

and the equivalent energy spread due to the emittance,

$$\sigma_\epsilon = \frac{k_r \epsilon a_w f}{4\gamma_r} = \frac{\pi \epsilon_n a_w f}{\lambda_w (1 + a_w^2)}. \tag{4.5}$$

These conditions can effect the changes in electron/radiation coupling via the changing deflection parameter, a_w, [34]. Therefore it is important to satisfy the above conditions when intialising the properties of an electron beam ϵ_n and σ_p, as defined in equation 3.3.

In the next section, the parameters are chosen to satisfy both of these conditions. Macroparticle propagation within the transverse plane, the radius calculated from the macroparticles' coordinates and the trajectory of macroparticles in $\bar{x} - \bar{z}$ frame are plotted.

Electron beam parameters		
Peak intensity	I_{pk}	≈ 9394.37A
Bunch Charge	Q_e	≈ 68 pC
Resonant electron energy	γ_r	≈ 489.24
Normalised Emittance	ϵ_n	1nπm.rad
Distribution of electron beam in $\bar{x}$		Gaussian
Distribution of electron beam in $\bar{y}$		Gaussian
Distribution of electron beam in $\bar{p}_x$		Gaussian
Distribution of electron beam in $\bar{p}_y$		Gaussian
Length of pulse in $\bar{z}_2$	ℓ_e	4
Distribution of electron beam in $\bar{z}_2$		Top-hat
Shot-noise		Yes

Undulator parameters		
Undulator Type		Helical
Pierce parameter	ρ	$\approx 1.4966 \times 10^{-2}$
Undulator wavelength	λ_w	1.5
Undulator deflection parameter	a_w	2
Focussing factor for helical	f	$\sqrt{2}$
Propagation distance	$\bar{z}$	20.2169

Table 4.2: Parameters used to model a matched electron beam with natural focussing.

4.2.2 Results

The electron beam used in this model has shot-noise included, but no FEL interaction. The main objective is to show that the transverse radius of an electron beam remains constant under the influence of natural focussing for a given emittance.

The parameters of the electron beam chosen in the model were also used in the next two sections: section 4.3 (with FEL interaction included) and 4.4 (with both diffraction and FEL interaction). Therefore a comparison of the results can be made; for example one can see how the integrated intensity differs between the models. The emittance parameter is checked with the conditions described above and additional checks were not required in sections 4.3 and 4.4.

The parameters used in the model are listed in table 4.2 and a discussion of these parameters and the initialisation of the FEL system are discussed next.

Using the parameters in table 4.2, one can show that the condition in equation 4.1 is satisfied. The radiation wavelength may be calculated using the reso-

nance condition, equation 2.44:

$$\lambda_r = \frac{\lambda_w(1 + a_w^2)}{2\gamma^2} \approx 1.018\text{Å}. \tag{4.6}$$

The condition related to the emittance is:

$$\epsilon_n < \frac{\gamma_r \lambda_r}{4\pi} \tag{4.7}$$

$$1 \times 10^{-6} < \frac{489.24 \times 1.018 \times 10^{-7}}{4\pi} \tag{4.8}$$

$$\Rightarrow 1 \times 10^{-6} < 3.96 \times 10^{-6} \tag{4.9}$$

The second condition in equation 4.2 is that the normalised energy spread must be smaller than ρ. The only contribution to the energy spread is due to emittance since there is no resonant energy spread, σ_P in equation 3.3, so equation 4.2 is changed to:

$$\sigma_\epsilon \ll \rho \tag{4.10}$$

$$\frac{\pi \epsilon_n a_w f}{\lambda_w(1 + a_w^2)} \ll \rho \tag{4.11}$$

$$\Rightarrow 1.367 \times 10^{-4} \ll 1.4966 \times 10^{-2} \tag{4.12}$$

It was shown that the beam emittance satisfies both of the conditions so the next calculated parameter is ρ. ρ can be calculated using equation 2.48 and the equation used here is:

$$\rho = \left(\frac{e\ I_{pk}\ a_w^2\ k_\beta}{32\pi\ \varepsilon_0\ m\ c^3\ \gamma_r^2\ k_w^2\ \epsilon_n} \right)^{1/3} \tag{4.13}$$

This equation is equivalent to equation 2.48 where the peak electron density, n_{pk}, has been redefined in terms of peak intensity and beam emittance. Given the parameters shown in table 4.2, ρ was calculated.

There are 5 macroparticles in each of the $\bar{x}$, $\bar{y}$, $\bar{p}_x$ and $\bar{p}_y$ direction and there must be one element per macroparticle in the transverse plane. The total size is 7×7 to allow transverse movement of the macroparticles. The r.m.s. radius of the electron beam is calculated using equation 2.334 in the transverse plane and equation 2.328 was used to calculated $\sigma_{\bar{p}_x}$ and $\sigma_{\bar{p}_y}$. The radii of the electron beam are:

$$\sigma_{\bar{x}} \approx 0.2283,\ \sigma_{\bar{y}} \approx 0.2283,\ \sigma_{\bar{p}_x} \approx 0.0211,\ \sigma_{\bar{p}_y} \approx 0.0211 \tag{4.14}$$

The range of the electron beam in these directions must be at least six times the σ to form an adequate Gaussian distribution. There are 213 macroparticles in the $\bar{z}_2$ and none in $\bar{p}_{\bar{z}_2}$, so the total number of macroparticles set to use is $133,125$ but the actual number used is $115,540$. The $17,585$ macroparticles have a small charge weight of real electrons compared to the $115,540$ macroparticles, so their effects are negligible and were removed. The percentage loss of real electrons was less than 0.1% when $17,585$ macroparticles were removed.

The natural focussing in a helical undulator is used where the f parameter shown in table 4.2 is the focussing factor and it is equal to $\sqrt{2}$. This parameter determines the scaled betatron wavenumber, $\bar{k}_\beta$, and ρ is also dependent on it. The scaled betatron wavelength may be calculated from $\bar{k}_\beta$, which is defined in equation 2.317:

$$\bar{\lambda}_\beta = \frac{2\pi}{\bar{k}_\beta} \tag{4.15}$$

$$= \frac{2\pi\ 2\sqrt{2}\,\rho\,\gamma_r}{a_w} \tag{4.16}$$

$$\approx 86.75 \tag{4.17}$$

One scaled betatron period is approximately 86.75 and the propagation distance in the model is approximately 20.22, about a quarter of the scaled betatron period.

Figures 4.3 are the transverse plane and discussion is given on the movement of the macroparticles. The grid lines in figure 4.3 are drawn to the size of the elements of the system in the transverse plane.

At $\bar{z} = 0$ the macroparticles are initialised as shown in figure 4.3(a).There are 5 $\bar{x}$ and 5 $\bar{y}$ mean positions in the transverse plane and the macroparticles are positioned around their mean values. The spread of the macroparticles in the centre is small compared to the ones at the corner; this is because the macroparticles at the side have less charge weight, N_j, than the ones in the centre. With the effects of shot-noise, the macroparticles' positions are varied inversely with respect to the charge weight, so the spread is larger at the edge of the beam.

From figure 4.3(a) to 4.3(b), $\bar{z} = 0$ to $\bar{z} = 10.9547$, the macroparticles have propagated in their own oscillating path along the undulator. In figure 4.3(b), it seems like the macroparticles have spread out from their initial position. Notice that some macroparticles have moved into the extra elements at the sides, this is compared to figure 4.3(a) where they exist only in the centre 5×5 elements in the centre of the plane.

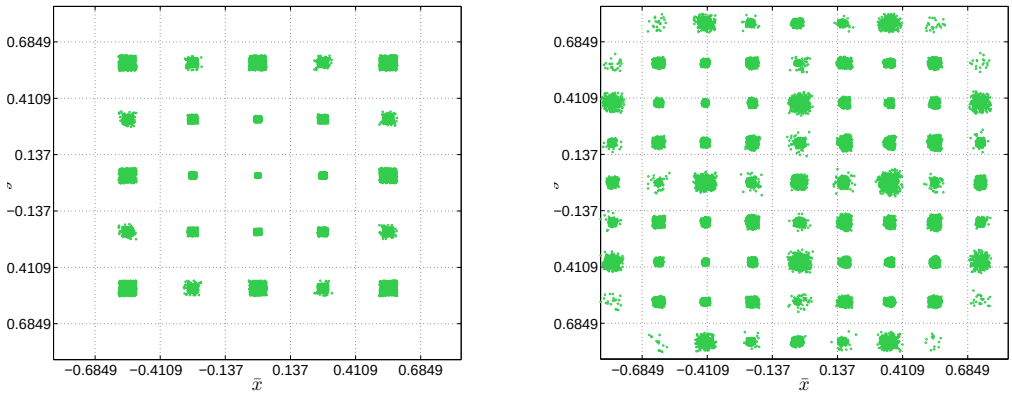

(a) $\bar{z} = 0$

(b) $\bar{z} = 10.9547$

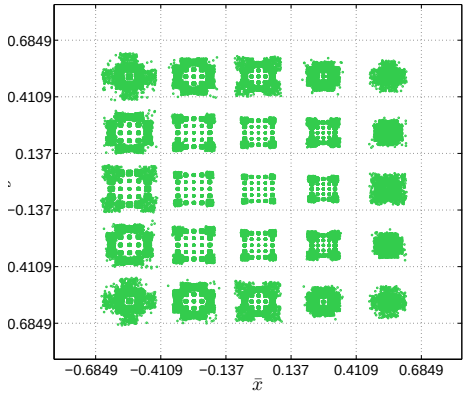

(c) $\bar{z} = 20.2169$

Figure 4.3: An electron beam has an emittance of 1n π m.rad, focussed by natural focussing of the undulator. There are 25 transverse position in the transverse plane and at each position there is a further 25 macroparticles that have different momentum. The movement of the macroparticles is shown at different $\bar{z}$. The electron beam was focussed in the transverse plane.

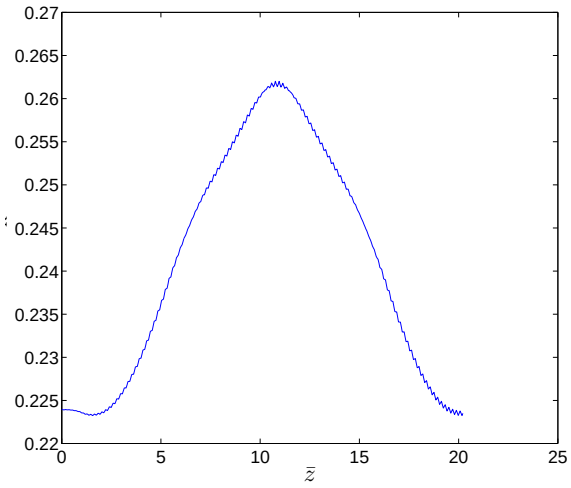

Figure 4.4: The radius of a matched electron beam, of emittance 1n π m.rad, is calculated from the transverse co-ordinates of the macroparticles. The figure shows the electron beam is focussed within its envelope in the transverse plane. This demonstrates the initial r.m.s radius of the electron beam and the natural focussing has been calculated correctly.

The macroparticles have propagated to approximately a quarter of the betatron period at $\bar{z} = 20.2169$. Their positions are contained within the centre 5×5 elements, this is shown in figure 4.3(c). Within an element, one can see there are a further 5×5 macroparticles' positions, since there are also 5×5 macroparticles in the transverse momentum space. Note that the macroparticles at the edge are more spread out compared to ones in the centre element. Throughout the propagation, the macroparticles have moved within the 7×7 element grid demonstrating the matched electron beam was focussed within its envelope. The next figure shows the r.m.s. radius of the electron beam. The radius of the electron beam was calculated from the macroparticles' transverse position. The radius is plotted against $\bar{z}$, the propagation distance, see figure 4.4 and it varied between 0.225 to 0.265; the input radius was 0.2283. The cause of this variation is the electron beam was not filled with macroparticles to cover all the transverse and momentum positions. However this is still a good indication that the calculated matched beam radius and the algorithm of the natural focussing have been solved correctly in the simulation code.

Figure 4.5 shows five randomly chosen macroparticles' trajectories in the $\bar{x}$-$\bar{z}$ plane. Macroparticle 1 and Macroparticle 4 $\bar{x}$ coordinates at $\bar{z} = 0$ are very close in figure 4.5, but their final $\bar{x}$ coordinates are different. All macroparticles have their own trajectories since they have different initial velocities and/or initial

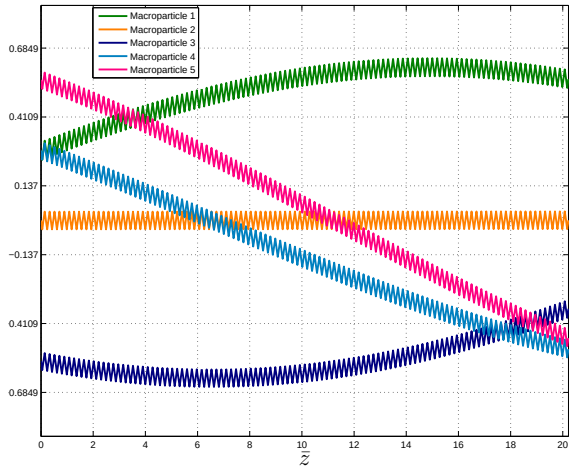

Figure 4.5: Five randomly chosen macroparticles' trajectories are plotted in the $\bar{x} - \bar{z}$ frame. This shows that no macroparticles propagate outside the beam envelope according to the matched beam theory.

coordinates. Again, same analogy applied to Macroparticle 4 and Macroparticle 5 that their final $\bar{x}$ coordinates are very close but their initial positions are different.

A 3D plot of the macroparticles' trajectories is shown in figure 4.6. The path of Macroparticle 2 in figure 4.5 looks approximately straight but in figure 4.6 one can see it was not a straight path. The five macroparticles' paths are different when viewing in figure 4.6 and each of them has a spiral motion in the 3D space.

The same matched electron beam is used in the next section but an FEL interaction and an energy spread in the $\bar{p}_{\bar{z}_2}$ direction are also included. The results of scaled intensity, scaled power and phase-space plots are shown in the next model.

4.3 Matched beam, shot-noise, focussing, energy spread and FEL interaction

The previous example has shown that given an electron beam emittance and the restoring force of natural focussing, the electrons propagate within their envelope. The next step is to include the effects of the FEL interaction and energy spread in the $\bar{p}_{\bar{z}_2}$ direction on the same FEL system, but still in absence of diffraction, allowing the evolution of the radiation and the electrons' behaviour to be studied.

This will use a rectangular current profile in $\bar{z}$ direction, with the same ℓ_e, the same emittance value for the electron beam which has a Gaussian distribution in

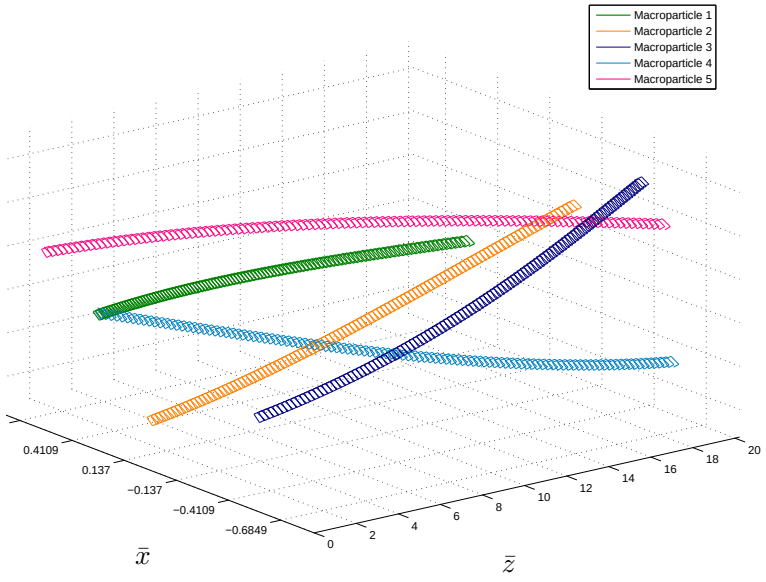

Figure 4.6: Five randomly chosen macroparticles' trajectories are plotted in 3D space.

the transverse plane and momentum transverse plane. Most of the parameters used in the model are the same as the previous model, but there is a resonant energy spread. The parameters used to model a matched electron beam with the effects of shot-noise and natural focussing are shown in table 4.3.

The extra information in the model is the resonant energy spread, σ_P, and the condition in equation 4.2 on the normalised energy spread must be computed again including this resonant energy spread as well as the equivalent energy spread due to the emittance. The standard deviation of the electron beam in $\bar{p}_{\bar{z}_2}$ is 0.002 and σ_P was calculated using the relations in equations 3.3, 3.4 and 4.4. From table 4.3, the standard deviation of $\bar{p}_{\bar{z}_2}$ is:

$$\sigma_{\bar{p}_{\bar{z}_2}} = 0.002 \tag{4.18}$$

The range of the electron beam in $\bar{p}_{\bar{z}_2}$ direction is:

$$\Rightarrow 0.994 < \bar{p}_{\bar{z}_2} < 1.006 \tag{4.19}$$

Using the relation between the 1D parameter p_j and $\bar{p}_{\bar{z}_2}$ in equation 3.4, the range in terms of p_j is:

$$\Rightarrow -0.2004 < p_j < 0.2004 \tag{4.20}$$

The standard deviation of p_j is ≈ 0.0668 and the resonant energy spread was

Electron beam parameters		
Peak intensity	I_{pk}	≈ 9394.37A
Bunch Charge	Q_e	≈ 68 pC
Resonant electron energy	γ_r	≈ 489.24
Normalised Emittance	ϵ_n	1nπm.rad
Distribution of electron beam in $\bar{x}$		Gaussian
Distribution of electron beam in $\bar{y}$		Gaussian
Distribution of electron beam in $\bar{p}_x$		Gaussian
Distribution of electron beam in $\bar{p}_y$		Gaussian
Length of pulse in $\bar{z}_2$	ℓ_e	4
Distribution of electron beam in $\bar{z}_2$		Top-hat
Sigma spread in $\bar{p}_{\bar{z}_2}$	$\sigma_{\bar{p}_{\bar{z}_2}}$	0.002
Distribution of electron beam in $\bar{p}_{\bar{z}_2}$		Gaussian
Shot-noise		Yes

Undulator parameters		
Undulator Type		Helical
Pierce parameter	ρ	$\approx 1.4966 \times 10^{-2}$
Undulator wavelength	λ_w	1.5cm
Undulator deflection parameter	a_w	2
Focussing factor for helical	f	$\sqrt{2}$
Propagation distance	$\bar{z}$	12.0361

Table 4.3: Parameters used to model non-zero emittance.

calculated using equation 3.3: $\Rightarrow \sigma_\gamma = 0.001$.

In previous models, the equivalent energy spread due to the emittance was calculated: $\sigma_\epsilon \approx 1.367 \times 10^{-4}$ and the normalised energy spread was re-calculated including the resonant energy spread:

$$\Delta_\epsilon = \sqrt{\sigma_\gamma^2 + \sigma_\epsilon^2} \tag{4.21}$$

$$= \sqrt{0.001^2 + (1.367 \times 10^{-4})^2} \tag{4.22}$$

$$\approx 1.009 \times 10^{-3} \tag{4.23}$$

$$\ll \rho \tag{4.24}$$

The solution above shows that the inequality in equation 4.2 is satisfied. The emittance inequality in equation 4.1 was already shown previously, so the beam quality should be sufficient to allow FEL lasing to occur.

There are 3 macroparticles in each of the $\bar{p}_x$, $\bar{p}_y$ and $\bar{p}_{\bar{z}_2}$ directions. In the other three spatial directions the same number of macroparticles were used as in the previous model: 5 in $\bar{x}$, 5 in $\bar{y}$, and 213 in $\bar{z}_2$. At any one spatial position,

there are 27 macroparticles and no two macroparticles has the same set of scaled initial momenta $(\bar{p}_{x0}, \bar{p}_{y0}, \bar{p}_{\bar{z}_20})$. The total number of macroparticles set to use was $143,775$, but only $133,762$ macroparticles were actually used. The number of real electrons that the $10,013$ macroparticles represents were small compared to the $133,762$ macroparticles so they are removed. The percentage of real electrons lost was less than 0.1%.

The electron emittance, see table 4.3, is $1 \times 10^{-6}\pi$ nm, which is the same as in the previous section, therefore the r.m.s radii of the electron beam are: $\sigma_{\bar{x}} \approx 0.2283$ and $\sigma_{\bar{y}} \approx 0.2283$. Also $\sigma_{\bar{p}_x} \approx 0.0211$ and $\sigma_{\bar{p}_y} \approx 0.0211$. The transverse grid used to setup the system is 9×9 elements. The propagation distance in the model is $\bar{z} = 12.0361$, therefore $1,117$ elements were used in $\bar{z}_2$ direction.

The evolution of scaled intensity in the transverse plane is shown in the following figures.

The electron pulse length in $\bar{z}_2$ is $\ell_e = 4$ and figure 4.7 shows the evolution of the scaled intensity at a fixed position along the electron pulse at $\bar{z}_1 = 3$. No initial seed field was used at $\bar{z} = 0$, as shown in figure 4.7(a), so the system started from shot-noise. At $\bar{z} = 7.9927$, $|A|^2$ began to increase, see figure 4.7(b). At one side of the interpolation scaled intensity is slightly higher; this is because the macroparticles were orbiting on the transverse plane and in that instance they interact more with the field nodes on the left. As the electron pulse propagates further to $\bar{z} = 9.2622$ shown in figure 4.7(c), the scaled intensity pulse has become more distinctively Gaussian and the amplitude has increased. This demonstrates the non-linear evolution of the radiation, and finally $|A|^2$ at $\bar{z} = 12.0361$ is shown in figure 4.7(d). The amplitude of $|A|^2$ at $\bar{z} = 12.0361$ is smaller than at $\bar{z} = 9.2622$; this will be explained along with figure 4.8, which is the scaled power plot in $\bar{z}_2$ frame.

The integrated scaled intensity, which is the scaled intensity integrated over the transverse plane, at $\bar{z} = 12.0361$ is shown in figure 4.8. The electrons are indicated in red. At $0 < \bar{z}_2 < 4$, the radiation in this region is CSE then from $\bar{z}_2 > 4$ the effects of SACSE may be seen by the growth rate of scaled power increasing exponentially until it reached saturation at $\bar{z} = 11.4719$. At $11.5 < \bar{z}_2 < 16.6$, the macroparticles were interacting with the radiation and this is the cause of the oscillation of the radiation in this region. At a fixed position of $\bar{z}_1 = 3$ in the electron frame, this corresponds to $\bar{z}_2 = 13.0361$ in the radiation frame at $\bar{z} = 12.0361$. The amplitude of the radiation at $\bar{z}_2 = 13.0361$ is small compare to the saturation peak. At $\bar{z} = 9.2622$, the fixed position $\bar{z}_1 = 3$ in the electron

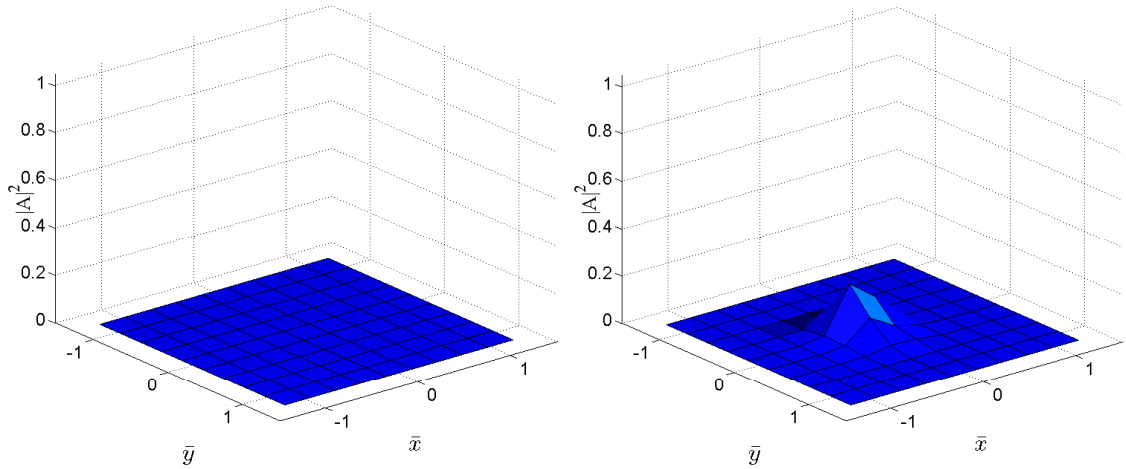

(a) $\bar{z} = 0$ (b) $\bar{z} = 7.9927$

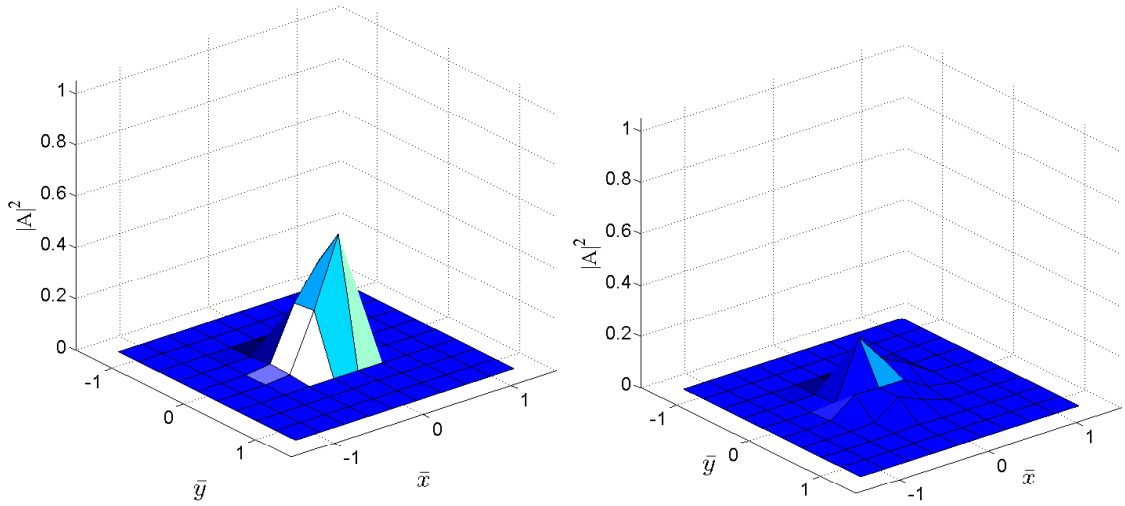

(c) $\bar{z} = 9.2622$ (d) $\bar{z} = 12.0361$

Figure 4.7: This simulation includes full 3D effects in the absence of diffraction. The evolution of the scaled intensity in the transverse plane for a fixed $\bar{z}_1 = 3$ is shown at four different figures at various $\bar{z}$. The scaled intensity is growing from $\bar{z} = 0$. The peak is smaller at $\bar{z} = 12.0361$ compared to $\bar{z} = 9.2622$ and indicates saturation has been reached between $\bar{z} = 9.2622$ and $\bar{z} = 12.0361$.

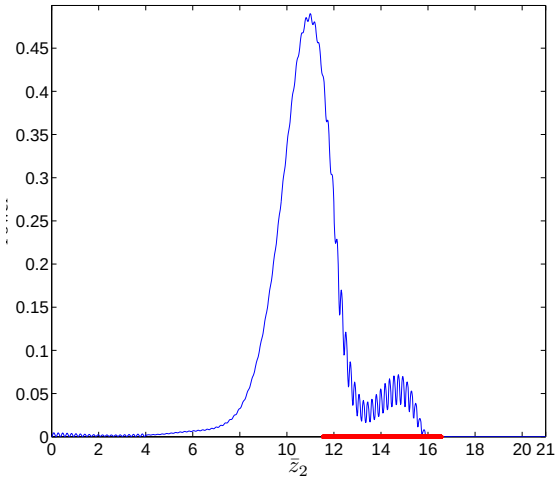

Figure 4.8: The power plot for a full 3D effects excluding diffraction, is plotted as a function of $\bar{z}_2$. The propagation distance is $\bar{z} = 12.0361$ and the red line indicates the electron pulse position. Saturation has been reached at around $\bar{z}_2 = 11$.

pulse corresponds to $\bar{z}_2 = 10.2622$, and the radiation would still be increasing exponentially. The amplitude of the scaled integrated intensity at $\bar{z} = 9.2622$ is larger than at $\bar{z} = 12.0361$ and this effect was shown in figures 4.7(c) to 4.7(d).

Figure 4.9 shows the phase-space of the macroparticles from $\bar{z} = 0$ to $\bar{z} = 12.0361$ and electron bunching is observed. Equation 4.20 is the range of the electron beam in $\bar{p}_{\bar{z}_2}$ direction and the macroparticles lie within this range at $\bar{z} = 0$, see figure 4.9(a). It was stated earlier in the section that 3 macroparticles were used in $\bar{p}_{\bar{z}_2}$ direction, the three lines in figure 4.9(a) represent the 3 different initial values of p_j. At $\bar{z} = 7.9929$, the macroparticles at the head of the electron pulse have bunched over a radiation period as shown in figure 4.9(b). The bunching is clearly shown at later stages in figure 4.9(c) and 4.9(d).

The effects of dispersion, shown in figures 4.9(b), 4.9(c) and 4.9(d), is due to the electron energy spread and are seen as the macroparticles with larger p_j propagate to larger $\bar{z}_1$ while those with smaller p_j propagate to smaller $\bar{z}_1$. Those electrons with decreasing p_j are losing energy to the radiation field. Most of the macroparticles shown in figure 4.9(d) were bunched over a radiation period. The difference in position becomes more pronounced as the macroparticles propagate further in $\bar{z}$.

Figure 4.10 shows the radius of the electron beam that was calculated from the macroparticles' transverse coordinates. The radius varies between 0.225 and 0.26, which is the same as figure 4.4 in the absence of FEL interaction and energy

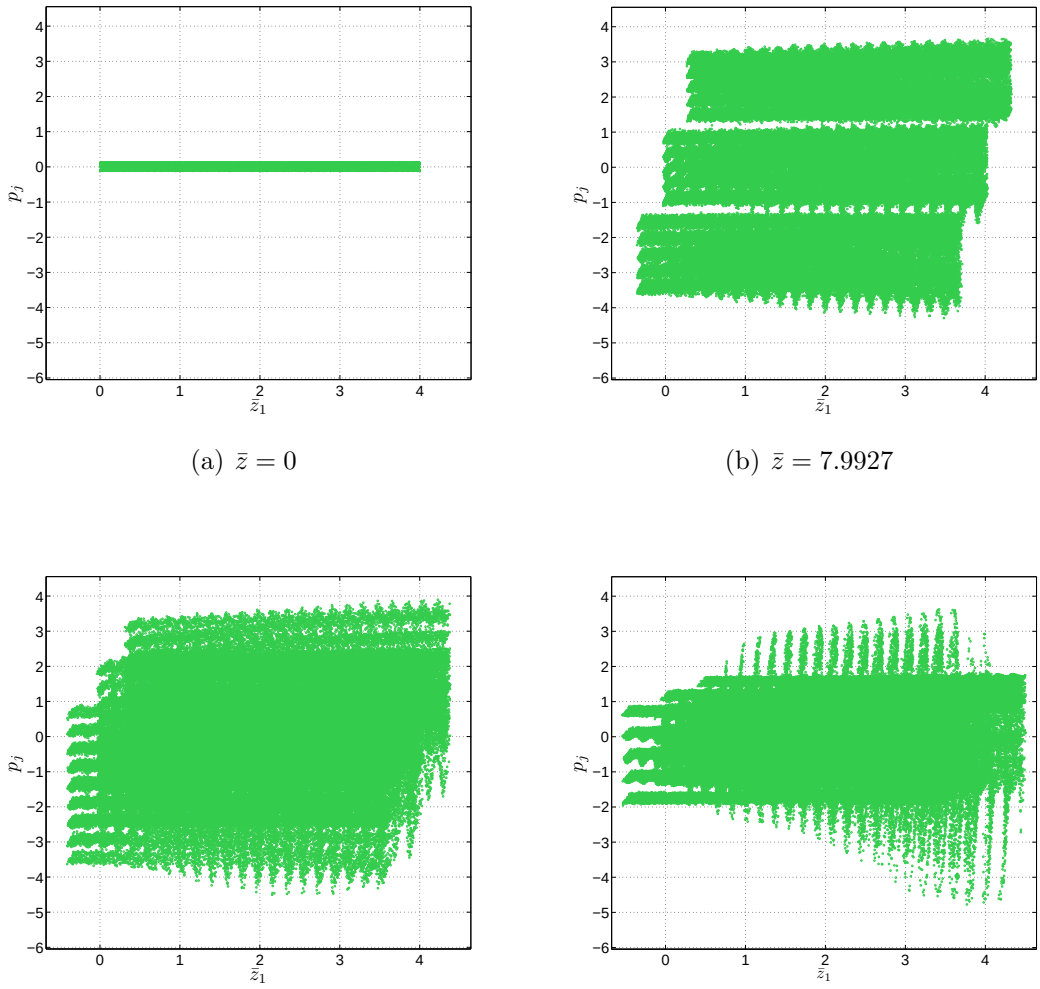

(a) $\bar{z} = 0$ (b) $\bar{z} = 7.9927$

(c) $\bar{z} = 9.2622$ (d) $\bar{z} = 12.0361$

Figure 4.9: This simulation plots macroparticle phase space with full 3D effects but excludes diffraction. The length of the electron pulse $\ell_e = 4$. The macroparticles are initially positioned as shown with three different values of p_j. Electrons bunching is seen to increase with $\bar{z}$.

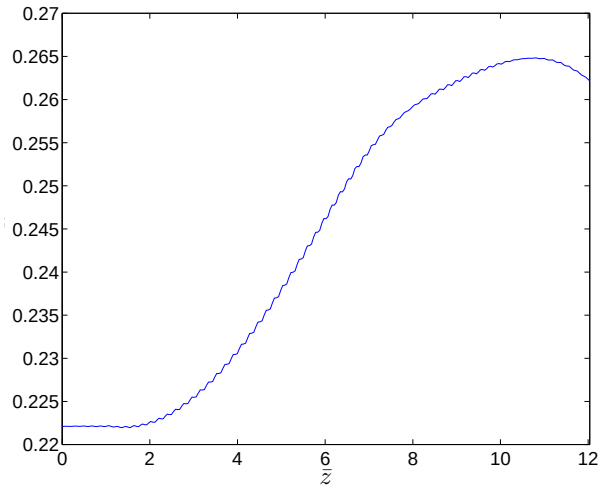

Figure 4.10: A matched electron beam with an emittance of 1nπm.rad. The radius of the electron beam is calculated from the macroparticles' transverse coordinates and is plotted as a function of $\bar{z}$. Full 3D effects are included but excluding diffraction.

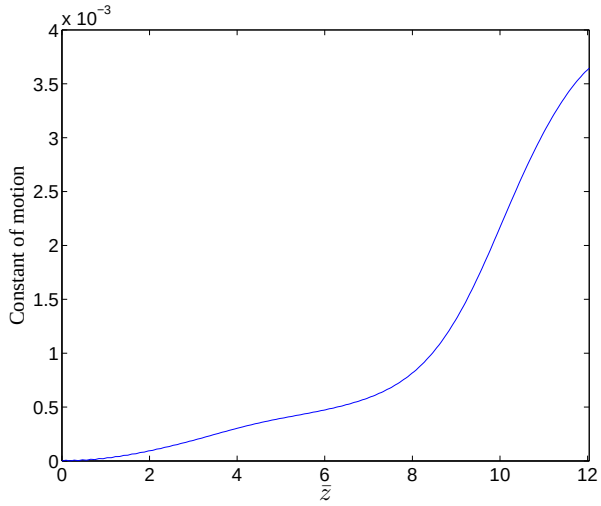

Figure 4.11: The energy conservation between radiation and electrons is plotted as a function of $\bar{z}$. A top-hat electron pulse of length $\ell_e = 4$ in a full 3D simulation excluding diffraction.

spread. This shows that the electron beam was matched when the macroparticles were interacting with the radiation. The plot in figure 4.11 shows that the conservation of energy has an uncertainty of the order 10^{-3}, therefore the FEL equations have been solved correctly using a matched electron beam that interacted with the radiation.

The matched electron beam in this section included effects of shot-noise and energy spread. It has been focussed using the natural undulator focussing and while interacting with no initial seed field radiation. In the final simulation of this chapter, this electron beam is used again and the effects of radiation diffraction are included.

4.4 Diffraction, FEL interaction, Shot-noise, Energy spread, Matched beam and focussing

The effects of diffraction and the use of a non-zero emittance electron beam have been tested individually and the results are in good agreement with the theory and analytical solutions.

An initial seed field, an electron beam that has a rectangular current profile in $\bar{z}_2$ and Gaussian distribution in the transverse plane which is matched to the undulator with the undulator focussing and an energy spread has been used to model the FEL interaction between the radiation and the macroparticles. The effects of radiation diffraction occurring in the vacuum region and gain-guiding occurring in the slippage region are shown in the final section.

A simulation described above is now presented with the parameters listed in table 4.4. Since an initial seed field was used, the parameters used were also added to the table.

The emittance of the electron beam, $\epsilon_n = 1\text{n}\ \pi\text{m.rad}$, was chosen to be the same in sections 4.2, 4.3 and also in this section for easy comparison. The standard deviation of the electron beam in $\bar{x}$, $\bar{y}$, $\bar{p}_x$ and $\bar{p}_y$ is calculated in the simulation code using the relationship from equations 2.328 and 2.334 and they are:

$$\sigma_{\bar{x}} \approx 0.2283\ \sigma_{\bar{y}} \approx 0.2283\ \sigma_{\bar{p}_x} \approx 0.0211\ \sigma_{\bar{p}_y} \approx 0.0211 \tag{4.25}$$

An important parameter to calculate is the Rayleigh range. This value is used to determine the size required in the transverse plane to allow radiation to

Electron beam parameters		
Peak Intensity	I_{pk}	≈ 9394A
Bunch Charge	Q	67.8744 pC
Resonant electron energy	γ_r	≈ 489.2377
Length of pulse in $\bar{z}_2$	ℓ_e	4
Distribution of electron beam in $\bar{z}_2$		Top-hat
Sigma spread in $p_{\bar{z}_2}$	$\sigma_{p_{\bar{z}_2}}$	0.002
Emittance	ϵ_n	1n πm.rad
Shot-noise		Yes
Seed field parameters		
Sigma spread in $\bar{x}$	Seed $\sigma_{\bar{x}}$	$\sigma_{\bar{x}}$
Sigma spread in $\bar{y}$	Seed $\sigma_{\bar{y}}$	$\sigma_{\bar{y}}$
Distribution of electron beam in $\bar{x}$		Gaussian
Distribution of electron beam in $\bar{y}$		Gaussian
Distribution of electron beam in $\bar{z}_2$		Top-hat
Initial field	$\lvert A\rvert$	≈ 0.0316
Undulator parameters		
Undulator Type		Helical
Pierce parameter	ρ	$\approx 1.4966 \times 10^{-2}$
Wiggler deflection parameter	a_w	1.5
Undulator wavelength	λ_w	1.5cm
Focussing factor	f	$\sqrt{2}$
Propagation distance	$\bar{z}$	≈ 8

Table 4.4: Parameters used to model all 3D effects.

diffract. The Rayleigh range is derived using equation 2.356 and the solution of $\sigma_{\bar{x}}$ has been computed and shown in equation 4.25:

$$\bar{z}_R = \frac{\sigma_{\bar{x}}^2}{2\rho} \tag{4.26}$$

$$\approx 1.7411 \tag{4.27}$$

An initial seed field with radius that of the electron beam was introduced, with an initial value of $|A| \approx 0.0316$. This seed has a Gaussian distribution in the transverse plane and a top-hat distribution in $\bar{z}_2$. The initial value was chosen so that the power $|A|^2$ integrated over the transverse plane was 0.001. Given this seed field, the beam waist of the radiation pulse may be calculated using equation

Number of elements	
$\bar{x}$	63
$\bar{y}$	63
$\bar{z}_2$	665
Number of electrons	
$\bar{x}$	7
$\bar{y}$	7
$\bar{z}_2$	213
$\bar{p}_x$	3
$\bar{p}_y$	3
$\bar{p}_{\bar{z}_2}$	3

Table 4.5: Number of elements and macroparticles used in the complete model, including full 3D effects.

2.341 [1] at $\bar{z} = 8$:

$$w(\bar{z} = 11) = w_0\sqrt{1 + \frac{\bar{z}^2}{\bar{z}_R^2}} \tag{4.28}$$

$$\approx 1.5181 \tag{4.29}$$

The number of elements needed and the number of macroparticles used in the system are listed in table 4.5: The 7×7 macroparticles are placed at the centre of the transverse plane, which takes up a 7×7 element grid. The electron momentum distributions are Gaussian and the number of macroparticles used to approximate the distributions are listed in table 4.5. At any one spatial position in $(\bar{x}, \bar{y}, \bar{z}_2)$, there are 27 macroparticles each of which have a different set of momenta. Shot-noise was also included when the macroparticles were initialised. The actual number of macroparticles used in the model is $263,485$ and $18,314$ macroparticles were removed because their charge weight is negligible compare to the $263,485$ macroparticles.

The full wave equation was solved and the effects of FEL interaction, focussing of the electron beam and diffraction of the radiation all happen concurrently. As there is no wavelength averaging, the effects of CSE may be observed, which is not possible from other three dimensional simulations. The evolution of the scaled intensity plots from $\bar{z} = 0$ to $\bar{z} = 7.9974$ at a fixed position within the electron pulse, $\bar{z}_1 = 4$, are shown in figure 4.12.

The scaled intensity shown in figure 4.12 is at the head of the electron pulse

[1] This equation is the same in the scaled units.

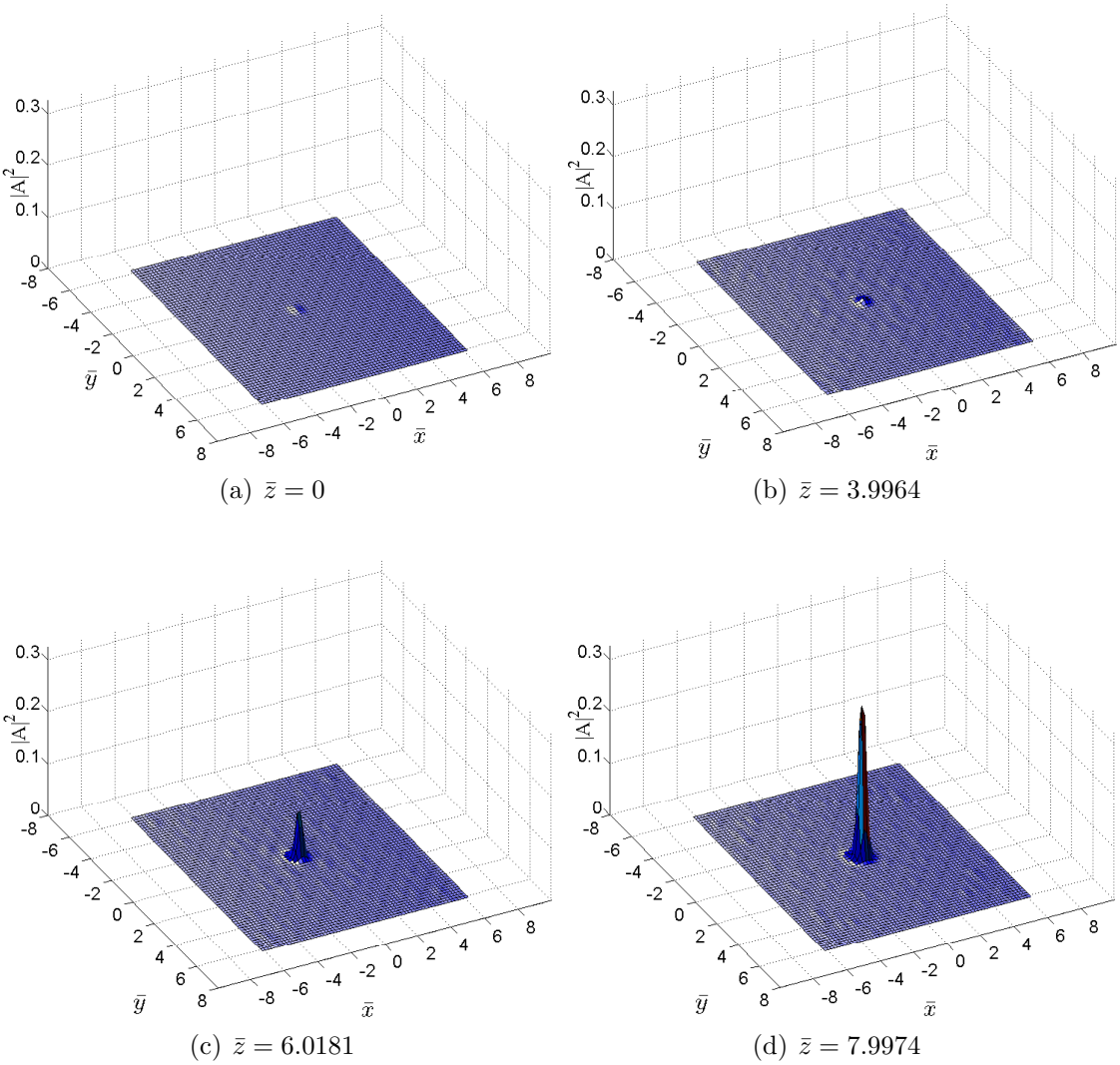

(a) $\bar{z} = 0$ (b) $\bar{z} = 3.9964$

(c) $\bar{z} = 6.0181$ (d) $\bar{z} = 7.9974$

Figure 4.12: Full 3D effects are modelled for a propagation distance of $\bar{z} = 7.9974$. The evolution of the scaled intensity is plotted in the transverse plane at a fixed $\bar{z}_1 = 4$ position (fixed position in the electron pulse). The radiation pulse intensity grows from $\bar{z} = 0$ to $\bar{z} = 7.9974$.

$\bar{z}_1 = 4$ (fixed position in the electron pulse). There is a Gaussian seed field at $\bar{z} = 0$, so the system did not start up from shot-noise. At $\bar{z} = 0$, figure 4.12(a), $|A|^2 = 0.001$ is the initial scaled intensity. A Gaussian seed would be seen when the $|A|^2$ axis is re-scaled. As the electron pulse propagates to $\bar{z} = 3.9964$, the Gaussian seed field grows and is visible in figure 4.12(b) on the transverse plane. The radiation has grown strongly at the head of the electron pulse at $\bar{z} = 6.0181$ as shown in figure 4.12(c) and a clear shape of the Gaussian field is shown. The evolution of the scaled intensity is shown at a fixed $\bar{z}_1$ position therefore the radiation field has a continuous interaction with the macroparticles. Figure 4.12(d) shows the scaled intensity has been amplified more at $\bar{z} = 7.9974$ and saturation was not reached.

The figures from 4.13(a) to 4.13(d) show the evolution of $|A|^2$ for a fixed $\bar{z}_2 = 7$ (fixed position in the radiation frame) as the electron pulse propagates past this point. When $\bar{z} = 0$, the radiation at $\bar{z}_2 = 7$ in figure 4.13(a) is zero since the seed field exists where the electron pulse lies, $0 < \bar{z}_2 < 4$. When the electron pulse propagates to $\bar{z} = 3.009$, the electron pulse lies between $3 < \bar{z}_2 < 7$. Near the tail of the electron pulse is $\bar{z}_2 = 7$ and the macroparticles began to emit radiation more strongly at this point, see figure 4.13(b), and the effects of gain-guiding occurs in this region. These effects will be discussed later in the section. When the electron pulse has travelled past $\bar{z}_2 = 7$, the head of the electron pulse has just propagated past this point. The radiation at $\bar{z}_2 < 7.0054$ in figure 4.13(c) is no longer interacting with the macroparticles and the radiation begins to diffract more strongly as this region is now in vacuum. At $\bar{z} = 7.9974$, the electron pulse has propagated past $\bar{z} = 7$ and the radiation in figure 4.13(d) has diffracted further and the peak of the radiation pulse reduced as expected. Compare this result with the model in the previous section, in the absence of diffraction, where the radiation pulse, see figure 4.8, in $\bar{z}_2 < 10$, which is the vacuum region, did not change.

The radius of the radiation pulse can be measured and diffraction effects were observed; these issues will be discussed further on in this section. The scaled integrated intensity plot of the model is shown in figure 4.14 where the macroparticles' $\bar{z}_2$ positions are shown in red.

A scaled power plot of $|A|^2$, integrated over the transverse plane, at $\bar{z} = 7.9974$ is shown in figure 4.14. The effects of CSE exist in $0 < \bar{z}_2 < 4$ and the gain was growing exponentially from $\bar{z}_2 = 4$. Within the electron pulse, the macroparticles were still interacting with the radiation. The amplitude of the power in $10 < \bar{z} < 12$ is small compared to other regions in front, this is because there was no

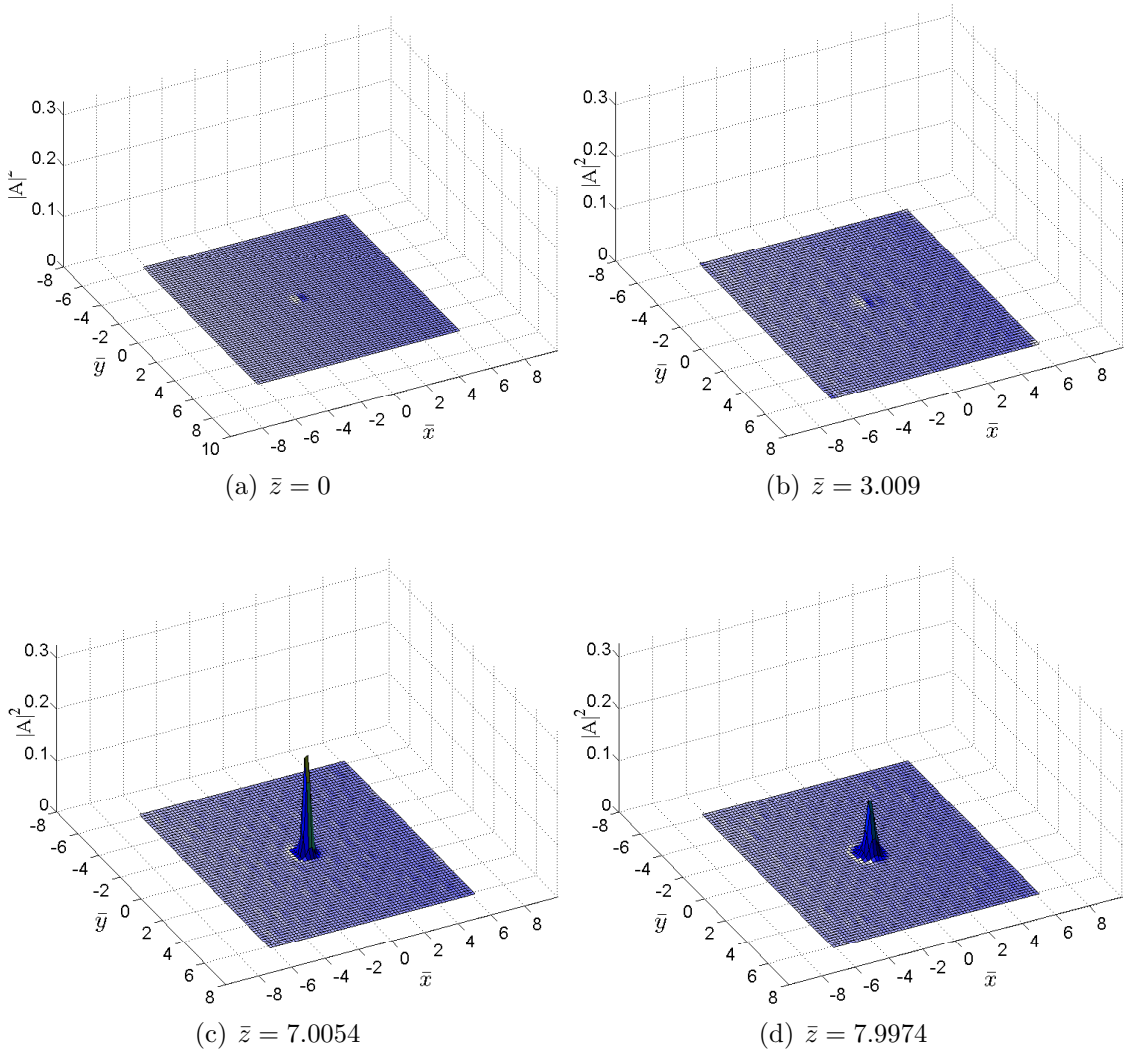

(a) $\bar{z} = 0$ (b) $\bar{z} = 3.009$

(c) $\bar{z} = 7.0054$ (d) $\bar{z} = 7.9974$

Figure 4.13: Full 3D effects for a propagation distance of $\bar{z} = 7.9974$. The evolution of the scaled intensity is plotted in the transverse plane at a fixed $\bar{z}_2 = 6.9925$ position (fixed position in the radiation frame). The radiation pulse is growing from $\bar{z} = 0$ until $\bar{z} = 7.0054$ and decreases afterwards where it propagates and diffracts into vacuum region from $\bar{z}_2 = 7$ as the electron pulse has propagated pasted this point.

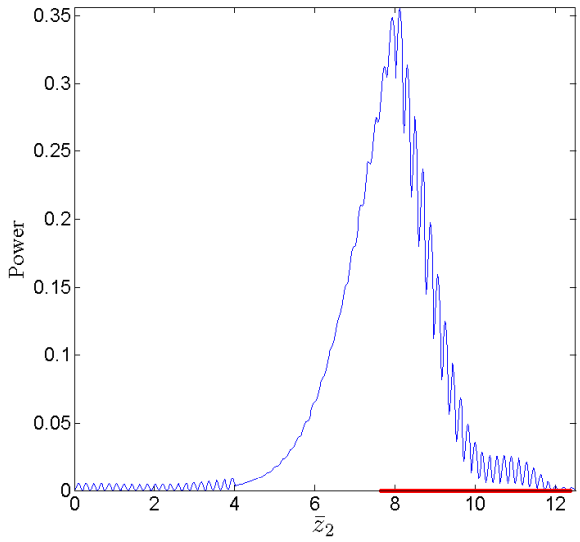

Figure 4.14: The scaled power in a full 3D effects that has an electron pulse length of $\ell_e = 4$ (in red) has propagated to $\bar{z} = 7.9974$ is shown. CSE effects at $0 < \bar{z}_2 < 4$. Exponential gain is seen with saturation not yet reached at $\bar{z} = 7.9974$.

incoming radiation from the back of the electron pulse to interact with. It should be noted that saturation was not reached at $\bar{z} = 8$; lack of machine memory limited the available integration region.

The effects of diffraction may be analysed by measuring the radius of the radiation pulse in the transverse plane. The radius of a Gaussian distribution radiation pulse is the σ-spread (or the standard deviation) of the Gaussian, and it is calculated using the definition of the standard deviation.

$$\sigma_{\bar{x}} = \sqrt{\bar{X^2} - (\bar{X})^2} \tag{4.30}$$

$$\text{where } \bar{X} = \frac{\sum \bar{x} \cdot |A(\bar{x})|^2}{\sum |A(\bar{x})|^2} \text{ and } \bar{X^2} = \frac{\sum \bar{x}^2 \cdot |A(\bar{x})|^2}{\sum |A(\bar{x})|^2} \tag{4.31}$$

Figure 4.15 shows the radius of the radiation pulse is calculated and plotted against $\bar{z}_2$. The radius of the radiation pulse at $\bar{z} = 0$, shown in figure 4.15(a), is equal to the radius of the electron beam and used as the initial condition, as expected. In figure 4.15(b) the radiation just before the head of the electron pulse, $\bar{z}_2 < 8$, has just entered into the vacuum region and is beginning to diffract. The radius in this region has increased, a sign of diffraction effects. Again, one can use the definition in equation 2.341 to calculate the analytical beam waist at $\bar{z} = 8$. The plot in figure 4.16 shows the analytical and numerical plots of the radiation pulse beam waist. The radiation pulse for $\bar{z}_2 < 4$ has diffracted significantly, and its shape is no longer a Gaussian, therefore the radius from the numerical results

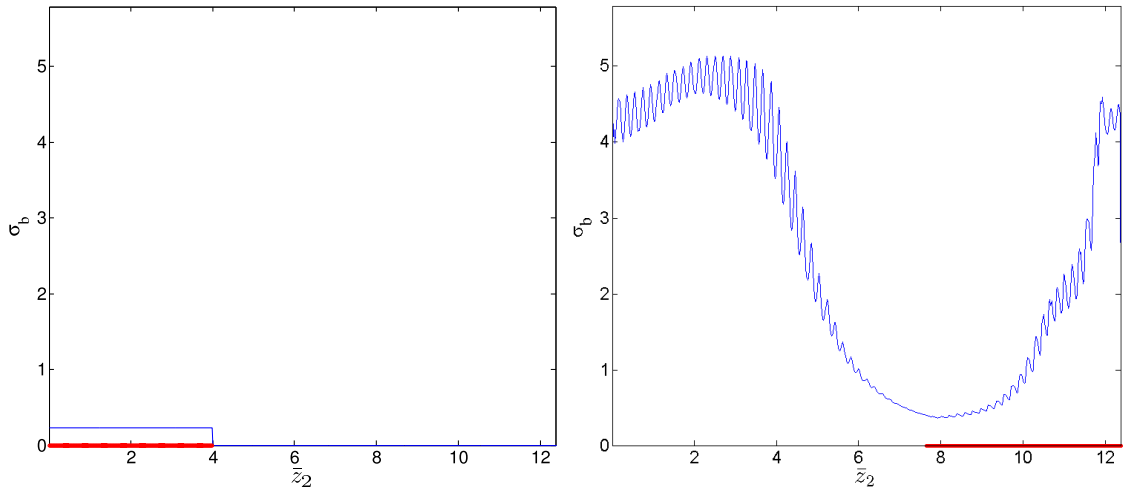

(a) $\bar{z} = 0$ (b) $\bar{z} = 7.9974$

Figure 4.15: For a full 3D effects simulation the radiation beam waist is calculated and plotted as a function of $\bar{z}_2$. At $\bar{z} = 0$ the radius of the radiation pulse is the r.m.s. transverse radius of the electron beam as expected. At $\bar{z} = 7.9974$ radiation before the head of the electron beam ($\bar{z}_2 \lesssim 7.5$) has propagated into free-space and diffraction occurs.

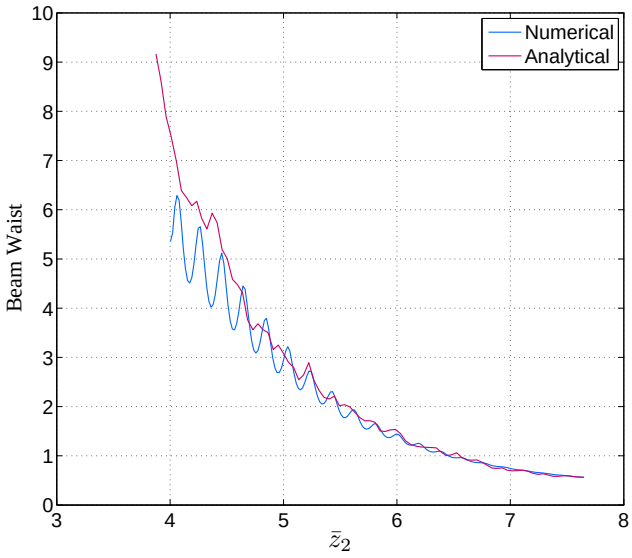

Figure 4.16: The beam waist of the radiation pulse is calculated from analysis and from the numerical results are plotted as a function of $\bar{z}_2$ at $\bar{z} = 7.9974$. Good agreement is seen.

is not accurate. Also the peak intensity value is close to its initial value, as seen from figure 4.14.

The numerical solution (blue) of figure 4.16 was calculated from the simulation results and is a good fit to the analytical solution (red) for $4 \lesssim \bar{z}_2 \lesssim \ell_e$. The quality of the agreement can be quantified if the numerical and analytical values shown in figure 4.16 are interpolated on to the same abscissae. Once the interpolation is carried out, the quality, ζ, can be evaluated as

$$\zeta = \frac{1}{N_{\text{pts}}} \sum_i |w_{ai} - w_{ni}| \tag{4.32}$$

where N_{pts} is the number of data points, w_a and w_n are the values of the beam waist calculated analytically and numerically respectively. A value of $\zeta = 0$ would be a perfect agreement between the two methods of calculation. In the case of data shown in figure 4.16, $\zeta = 0.53$; the largest proportion of this value is due to the increasing oscillatory behaviour at low values of $\bar{z}_2$. If one limits the range over which the evaluation is carried out to $\bar{z}_2 > 6$, the quality of agreement improves substantially, to $\zeta = 0.19$ [35].

The electron pulse lies between $6.347 < \ell_e < 11$ when $\bar{z} = 6.6293$ and the radii within the electron pulse were approximately the same except for a region near the tail of the electron pulse, $\ell_e > 9$. While the radiation is still interacting with the electrons, they continue to emit radiation in this region reducing the perception of diffraction. This is known as the "gain-guiding" effect [36].

The radius of the radiation pulse at the tail of the electron pulse is larger than in other regions of the electron pulse. This is because there is no incoming radiation from "behind" to interact with the electrons there, so the electrons are spontaneously emitting radiation and there is no gain guiding. In figure 4.17(a) the electrons at $9 < \bar{z}_2 < 11$ did not have any radiation to interact with. After one gain length, $\Delta\bar{z} = 1$, the radiation in this region was interacting with the electrons and the radius is approximately the same as in the region in front. This is another phenomenon showing that gain-guiding has occurred in this system.

The final figure of the section shows the conservation of energy between the radiation and the electrons. In figure 4.18, the constant of motion that was calculated using equation 2.302 is plotted against the propagation distance and the conservation of energy is good. The relative numerical error is of the order 10^{-4} which indicates that the 3D model has solved this system correctly.

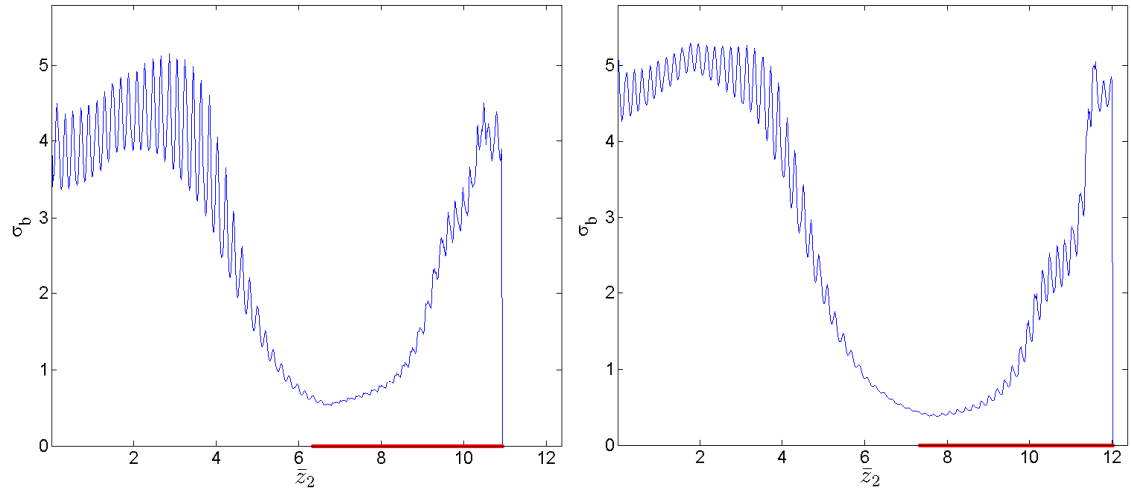

(a) $\bar{z} = 6.6293$ (b) $\bar{z} = 7.6636$

Figure 4.17: The radiation beam waist is calculated from the numerical results at $\bar{z} = 6.6293$ and $\bar{z} = 7.6636$. The beam waist in $9 < \bar{z}_2 < 11$ at $\bar{z} = 6.6293$ is larger than at $\bar{z} = 7.6636$. This is because after approximately one gain length, the beam waist decreases as the macroparticles interact with the radiation receiving gain and reducing apparent diffraction. This is called gain-guiding.

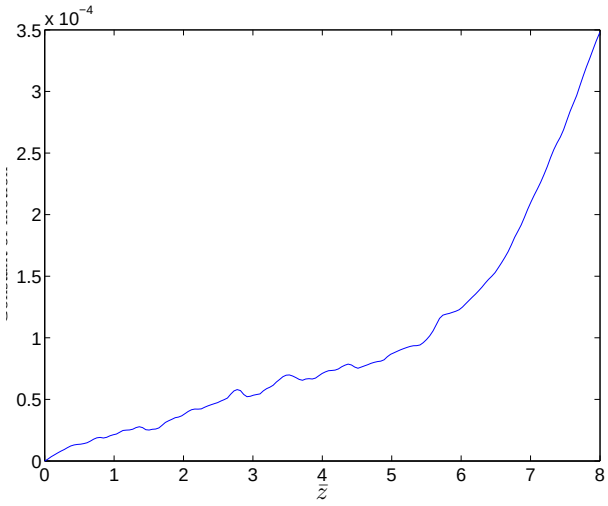

Figure 4.18: The energy conservation between radiation and electrons is plotted as a function of $\bar{z}$ for the previous results. The relative error of $\sim 10^{-4}$ demonstrates the numerical model is solving the equations effectively.

Chapter 5

Future work and Conclusion

5.1 Conclusions

In this thesis a new theory and computational model for a fourth generation light source using the FEL technology was developed. A simulation code was written in Fortran 95 using parallel architecture to model the FEL interaction between the radiation field and electrons in three dimensions. This is the first such 3D model to be developed which has not averaged either the electron motion or the radiation field over an undulator period.

A major part of the work was the derivation of new scaled 3D FEL equations from Maxwell's wave equations and the Lorentz equation. These equations were scaled with respect to the gain-length, l_g, and/or the cooperation length, l_c, so that they became dimensionless. A conservation of energy expression was derived and used to check whether the FEL system of equations had been numerically integrated correctly.

A 1D model was developed that uses pulses of electrons. Here slippage effects became important and superradiance effects were observed. A 1D limit was applied to the 3D code in order to reproduce the previous 1D results of [18] and [32].

The numerical method used to solve the 3D FEL equations is the Split-Step Fourier Method (SSFM) incorporating the Finite Element Method (FEM) and 4th order Runge–Kutta (rk4). The SSFM was carried out in two steps: first, diffraction acts alone on the field in the absence of any source, then the source term drives the field in the absence of diffraction. The solution from the first step of the SSFM acts as an initial value for the second step. In the second step, the transverse derivatives in the wave equation were set to zero and the FEM applied to the equation. The electron equations in the 3D model are similar to

the equation of the 1D model with an additional term for focussing. For the radiation the main differences between the 3D and 1D models are the effects of diffraction and the electron matched beam. The complex envelope approximation was the only assumption made in the 3D model. Other current 3D models average the radiation over one period so they cannot simulate CSE that arise from current gradients within the electron pulse.

The 3D results included the effects of radiation diffraction, shot-noise and energy spread in the electron beam, matched electron beam with focussing and the FEL interaction between the radiation and electrons. Simulations of these individual effects were carried out successfully. Energy was conserved when all effects of FEL interaction are included.

The effects of diffraction were tested alone without any influence from the electrons for 3D results. An initial Gaussian seed field was used and the resultant beam waist after one Rayleigh agreed with analysis. A non-zero emittance electron beam was modelled along with focussing. The result shows that the electrons propagated within their envelope whether interacting with the radiation or not. The electrons in phase-space were bunched over a radiation period and the energy constant of motion was maintained to within a factor 10^{-3}.

The full 3D model was simulated including the effects of diffraction, FEL interaction, energy spread, emittance and shot-noise in the electron beam. An initial Gaussian seed field, which is the same transverse size as the electron beam, was used. At the head of the electron beam the intensity of the radiation increased due to the FEL interaction as the electron beam propagated along $\bar{z}$. At a fixed $\bar{z}_2$ position the 3D plots showed the intensity in the transverse plane undergoing exponential gain and the radiation diffracting according to theory when it enters the vacuum. The scaled intensity integrated over the transverse plane showed that the radiation power was exponentially amplified as the electron pulse propagate along $\bar{z}$. The radius of the emitted radiation pulse was calculated and there was a good agreement between the analytical and the numerical solutions for the diffracted radiation radius. The effects of radiation diffraction, gain-guiding, electrons bunching and FEL interaction were observed. To the author's knowledge the simulation code developed in this thesis is the only model that can simulate all the effects described.

The theory and modelling of a three dimensional FEL was carried out successfully. The numerical methods used in the simulation code were a good approach and minimal assumptions were made. This will lead to greater understanding of FEL operation.

5.2 Future Work

The work carried out during the course of this thesis may be extended further by adding additional features to the simulation code, using a different numerical method to solve the 3D FEL equations. Details of the methodology used in this thesis will also now be published.

The routines used to set up and store arrays for the FFT are different from those used for the linear solver, and the BLACS routine, provided by NAG administrators, must be used to gather the results. It is possible to advance this work by using other open source libraries, which would allow the simulation to stand alone without using the third-party NAG libraries. FFTW (Fastest Fourier Transform in the West) [37], is a C subroutine library for computing the FFT, may be used. For the linear solver, an open source library called LAPack [38], (Linear Algebra Package), provides routines for solving systems of equations. One of the major issues which arose with NAG was the communication between the root processor and all the other processors: this could be reduced by using another method.

The element size in the transverse plane was constant throughout the work carried out in this thesis; variable sized elements could be used in the future to define a finer grid near the centre than in the surrounding region. If this change was to be applied in the simulation code, one must rewrite the routine for identifying which element an individual electron is located within. The current version of the electron location routine only works for elements of equal size.

A new method based on [39] will be used in the second part of the Split-Step Fourier method to solve the Maxwell wave equation. The solution of the scaled radiation envelope will remain in Fourier space after the first half of the SSFM. The second part of the wave equation will be derived in the same way as in this thesis and then it will be transformed into Fourier space. This new method should eliminate the need for the FEM and allow an easier and ultimately faster parallel implementation of the code. The solution from the first part of the SSFM is already scattered over the processors and there will be no need to gather the solutions into a single processor before computing the second part of the SSFM. This will save a lot of computational time since no inverse Fourier transform needs to be carried out until the end of the calculations. A detailed explanation and calculations using this method will be published in the future [40].

A conference proceedings paper on the theory and modelling of the new 3D FEL model was published at the FEL 2008 conference D and a poster presentation was presented at this conference. There will be addition publications in other journals, such as Physical Review, on the work carried out in this thesis including

the 3D results; these publications are in preparation.

Bibliography

1. Berliner Elektronenspeicherring-Gesellschaft für Synchrotronstrahlung (BESSY). History development
online at http://www.bessy.de/cms.php?idcatart=618&changelang=5.

2. National Synchrotron Light Source. A brief history of NSLS
online at http://www.nsls.bnl.gov/about/history/.

3. A L Robinson. X-Ray Data Booklet - Section 2.2 History of synchrotron radiation. Lawrence Berkeley National Laboratory, Feburary 2005.
online at http://xdb.lbl.gov/Section2/Sec_2-2.html.

4. H Owen. Beam lifetime at the SRS. *Particle Accelerator Conference, 1997. Proceedings of the 1997*, 1:333–335, 1997.

5. Biedron, O'Shea, Todd. SYNCHROTRON RADIATION IN 2003. NPSS Newsletter. online at http://www.ieee.org/organizations/pubs/newsletters/npss/0304/sync.html.

6. ESRF. The making of the ESRF, 2006. online at http://www.esrf.eu/AboutUs/CompanyInfo/KeyDates/History.

7. NEC Microwave Tube Ltd. History.
online at http://www.nec-mwt.com/english/company/history.html.

8. Committee on Free Electron Lasers and National Research Council Other Advanced Coherent Light Sources. *FREE ELECTRON LASERS AND OTHER ADVANCED SOURCES OF LIGHT*. National Academy Press, Washington, D.C., 1994.
online at http://www.nap.edu/catalog.php?record_id=9182#toc.

9. R Bonifacio et al. Physics of the High-Gain FEL and Superradiance. *Rivista Del Nuovo Cimento*, 13(9), 1989.

10. DESY. The European X-Ray Laser Project XFEL, 2008.
online at http://xfel.desy.de/.

11. SPring-8. Accelerator Division - SPring-8 Web Site, 2008. online at http://www.spring8.or.jp/en/about_us/organization/accelerator.

12. B W J McNeil. Fee-Electron Lasers: A down-sized design. *Nature Photonics*, 2(9):522–524, 2008.

13. P Barratt. Launch of New UK Light Source Project, 2008. online at http://www.scitech.ac.uk/PMC/PRel/STFC/LightSource.aspx.

14. Vijay Pande and Stanford University. Folding @ home, 2000–2008.

15. W M Fawley. An enhanced GINGER simulation code with harmonic emission and HDF5 IO capabilities. *Proceedings of FEL 2006, BESSY, Berlin, Germany*, pages 218–221, 2006. available at http://www.bessy.de/fel2006/proceedings/PAPERS/MOPPH073.PDF.

16. S Reiche. GENESIS 1.3 : a fully 3D time-dependent FEL simulation code. *Nuclear Instruments and Methods in Physics Research A*, 429:243–248, 1999.

17. E L Saldin et al. FAST : a three-dimensional time-dependent FEL simulation code. *Nuclear Instruments and Methods in Physics Research A*, 429:233–237, 1999.

18. B W J McNeil, M W Poole, G R M Robb. Unified model of electron beam shot noise and coherent spontaneous emission in the helical wiggler free electron laser. *Physical Review Special Topics - Accelerators and Beams*, 6:070701–1–10, 2003.

19. W. H. Press et al. *Numerical Receipes in Fortran 77*. Cambridge University Press, Cambridge, 1992.

20. P W Milonni, J H Eberly. *LASERS*. Wiley-Interscience, 1988.

21. The Numerical Algorithms Group. NAG. online at http://www.nag.co.uk/.

22. Advance Photo Source. OAG Documentation. online at http://www.aps.anl.gov/asd/oag/documentation.shtml.

23. B W McNeil, 2008. *Private Communication*.

24. R Bonifacio, B W J McNeil. Slippage and superradiance in the high gain fel. *Nuclear Instruments and Methods in Physics Research Section A*, 272:280–288, 1988.

25. R Bonifacio, C Maroli, N Piovella. Slippage and supperadiance in the high gain fel: Linear theory. *Optics Communications*, 68:369–374, 1988.

26. W M Sharp et al. Simulation of superradiant free electron lasers. *Nuclear Instruments and Methods in Physics Research section A*, 285:217–233, 1989.

27. R H Dicke. Coherence in spontaneous radiation processes. *Physical Review*, 93:99–110, 1954.

28. 4GLS Design Team. *4GLS Conceptual Design Report*. CCLRC, UK, 2006. online at http://www.4gls.ac.uk/documents.htm.

29. Claes Johnson. *Numerical solution of partial differential equations by the finite element method*. Press Syndicate of the University of Cambridge, Sweden, 1995.

30. Huebner, Thornton, Byrom. *The finite element method for engineers*. J Wiley & Sons, New York, 1983.

31. R Bonifacio et al. *High Gain, High Power Free Electron Laser: Physics and Application to TeV Particle Acceleration*. North-Holland Physics, Amsterdam, 1989.

32. B W J McNeil, G R M Robb, D A Jaroszynski. Self-amplication of coherent spontaneous emission in the free electron laser. *Optics Communications*, 165:65–70, 1999.

33. William M Fawley. Algorithm for loading shot noise microbunching in multidimensional, free-electron laser simulation codes. *Physical Review Special Topics - Accelerators and Beams*, 5:070707–1:6, 2002.

34. R Bonifacio, L De Salvo Souza, B W J McNeil. Emittance limitations in the free electron laser. *Optics Communications*, 93:179–185, 1992.

35. I D Paton, 2008. *Private Communication*.

36. Y Seo. Active optical guiding and gain guiding in a free electron laser. *Physics of Plasma*, 3:4748–4750, 1996.

37. Matteo Frigo, Steven G Johnson. Fastest Fourier Transform in the West (FFTW). online at `http://www.fftw.org/`.

38. LAPACK. Linear Algebra PACKage.
online at `http://www.netlib.org/lapack/`.

39. N Piovella. High gain free electron laser amplifiers starting from coherent and incoherent spontaneous emission. *Physics of Plasmas*, 6:3358–3368, 1999.

40. L Campbell, 2008. *Private Communication*.

41. W Backer, J K McIver. Madey's theorems for free-electron devices, spontaneous emission, and applications. *Zeitschrift für Physik D*, 7, 1988.

42. Haruo Kuroda. Status of FEL-SUT Project. *Japanese Journal of Applied Physics*, 41, 2002.

43. R Bonifacio, B W J McNeil. Slippage and superradiance in the high gain FEL. *Nuclear Instruments and Methods in Physics Research Section A*, 272:280–288, 1988.

44. Craig Hamilton. Undergraduate final year project. University of Strathclyde, UK, 2006.

45. The Numerical Algorithms Group. Numerical Algorithms Group:C06. online at `http://www.nag.co.uk/numeric/FD/manual/html/C06_fd03.html`.

Appendix A

δ function

To change from z to t

$$\delta(z - z_j(t)) = \frac{\delta(t - t_j)}{|\frac{dz_j(t)}{dt}|} \qquad \text{where } \frac{dz_j(t)}{dt} = v_j \tag{A.1}$$

Also $\delta(\alpha x) = \frac{1}{\alpha}\delta(x)$ and as

$$\bar{z}_{2j} = 2k_w\rho\frac{\bar{\beta}_z}{1 - \bar{\beta}_z}(ct_j - z) \tag{A.2}$$

$$t_j = \frac{1}{c}\left(\frac{1 - \bar{\beta}_z}{\bar{\beta}_z}\frac{\bar{z}_{2j}}{2k_w\rho} + \frac{\bar{z}}{2k_w\rho}\right) \tag{A.3}$$

$$t - t_j = \frac{1}{c}\frac{1 - \bar{\beta}_z}{\bar{\beta}_z}\frac{1}{2k_w\rho}(\bar{z}_2 - \bar{z}_{2j}) \tag{A.4}$$

So the δ function becomes

$$\delta(t - t_j) = 2k_w\rho c\frac{\bar{\beta}_z}{1 - \bar{\beta}_z}\delta(\bar{z}_{2j} - \bar{z}_{2j}) \tag{A.5}$$

$$\Rightarrow \delta(z - z_j(t)) = \frac{1}{\beta_{zj}}2k_w\rho\frac{\bar{\beta}_z}{1 - \bar{\beta}_z}\delta(\bar{z}_{2j} - \bar{z}_{2j}) \tag{A.6}$$

Appendix B

Relate $x^{'}$ to $\bar{p}_x$

Beginning with equation (2.308),

$$\bar{p}_{xj} = \frac{\gamma_j}{c}\frac{dxj}{dt} \tag{B.1}$$

$$= \frac{\gamma_j}{c}\beta_{zj}c\frac{dxj}{dz} \tag{B.2}$$

$$= \gamma_j\beta_{zj}\frac{dxj}{dz} \tag{B.3}$$

$$\frac{dxj}{dz} = \frac{1}{\gamma_j\beta_{zj}}\bar{p}_{xj} \tag{B.4}$$

$$= \frac{1}{\beta_{zj}}\left[\frac{1-\beta_{zj}^2}{1+|\bar{p}_{\perp j}|^2}\right]^{1/2}\bar{p}_{xj} \tag{B.5}$$

$$= (1+\varepsilon_j)\left[\frac{1-\frac{1}{(1+\varepsilon_j)^2}}{1+a_w^2}\right]^{1/2}\bar{p}_{xj} \quad \text{where } \varepsilon_j \equiv \frac{1-\beta_{zj}}{\beta_{zj}} \tag{B.6}$$

$$= (1+\varepsilon_j)\left[\frac{1-\frac{1}{(1+\varepsilon_j)^2}}{2\varepsilon\gamma_r^2}\right]^{1/2}\bar{p}_{x_j} \tag{B.7}$$

$$= (1+\varepsilon_j)\left[\frac{(1+\varepsilon_j)^2-1}{2\varepsilon\gamma_r^2(1+\varepsilon_j)^2}\right]^{1/2}\bar{p}_{xj} \tag{B.8}$$

$$= \left[\frac{\varepsilon_j(2+\varepsilon_j)}{2\varepsilon\gamma_r^2}\right]^{1/2}\bar{p}_{x_j} \tag{B.9}$$

$$= \left(\frac{2+\varepsilon_j}{2\gamma_r^2}\right)^{1/2}\bar{p}_{xj} \tag{B.10}$$

$$\approx \frac{1}{\gamma_r}\bar{p}_{xj} \tag{B.11}$$

Appendix C

Macroparticles charge weight parameter, $\bar{\chi}$

χ_k needs to be calculated for each k^{th} macroparticle and the definition of χ_k is known already,

$$\chi_k = \frac{N_k}{\bar{n}_p V_k} \tag{C.1}$$

where N_k is a Poisson variate which is computed in a separate module, `genMacro.f90`. V_k is the volume occupied by each macroparticle, defined in equation 2.163 and see figure 2.12. $\bar{n}_p$ is the peak electron density.

$\bar{n}_p$ can be calculated using the parameters computed in the `genMacro.f90` subroutine.

$$\bar{n}_p = max\left[\frac{m\_number_k}{V_k}\right] \tag{C.2}$$

The variable "m_number", which is required when calculating $\bar{n}_p$ is the mean number of electrons in $\bar{x}$, $\bar{y}$ and $\bar{z}_2$ direction, the other three dimensions of $\bar{p}$'s are not included.

Replace this definition $\bar{n}_p$ into χ_k to get

$$\chi_k = \frac{N_k/V_k}{max\left[\frac{m\_number_k}{V_k}\right]} \tag{C.3}$$

If V_k, the electron spatial grid element volume, is approximately constant and V_e is the element volume of the stiffness matrix. Then $\frac{V_e}{V_k}$ describes the number of macroparticles in one element. However, the length of $\bar{x}$ (or $\bar{y}$ or $\bar{z}_2$) in the grid can vary, so the volume of the electron grid element V_k can deviate from one element to the next. N_k is the actual number of electrons of the k^{th} macroparticle using the Poisson distribution.

Previously, the calculation for the second part of the field equation was explained and the weighting factor χ_k mentioned. The subroutine `genMacro.f90` was used to calculate this factor and can be used for one to three dimensions in space with three additional momentum dimensions. The compulsory inputs are:

- The number of real electrons, N_e.

- Shot-noise is switched on or off, q_noise = "TRUE" or "FALSE".
- Supply at least one spatial dimension grid points.
- Supply the corresponding distribution function(s).

The input grid points are provided by the user. The options are uniformly spaced ('`linspace`') or gaussian spaced ('`GaussianGrid`'). In `linspace` subroutine, the user specifies the number of macropaticles in each space and momentum direction. The grid points are calculated accordingly so the spacing between the points are equal. In the gaussian spaced function the grid points are calculated where the area under the gaussian are equal. If there are 5 macroparticles in the $\bar{x}$ direction there will be 6 grid points. The first grid points is the starting value of $\bar{x}$, $\bar{x}_0$. The next point, $\bar{x}_1$, is calculated where the area under the gaussian is 0.2. The third point, $\bar{x}_2$, have area=0.4 under the distribution and so on. The spacing between the grid points varies depending on the number of macroparticles used in each direction.

A corresponding distribution function is also supplied to the `genMacro` subroutine. This function used here is the Gaussian distribution, $f(x)$. Integrating $f(x)$,

$$\int_{-\infty}^{\infty} f(x)dx = F \tag{C.4}$$

To normalised $f(x)$ one need to divide by F,

$$f_n(x) = \frac{f(x)}{\int_{-\infty}^{\infty} f(x)dx} \tag{C.5}$$

$$= \frac{f(x)}{\sum_i f_i \delta x_i} \tag{C.6}$$

In `Dfunction` subroutine, this is how one would normalised the Gaussian distribution function.

Appendix D

FEL Conference Paper 2008

Appendix E

CD containing code